Development of Highly Transparent Y_2O_3–Based Ceramics via Advanced Powder Processing Technique

LU Bin

Doctoral program in Materials Science and Engineering

Submitted to the Graduate School of
Pure and Applied Sciences
in Partial Fulfillment of the Requirements
for the Degree of Doctor of Philosophy in
Engineering

at the
University of Tsukuba

Thesis Abstract

Polycrystalline transparent ceramics as one of the most important functional materials have extensive applications in various areas. By properly doping with activator ions, transparent ceramic scintillators may be attained by employing advanced powder processing and ceramic sintering techniques. Transparent $Y_{1.34}Gd_{0.6}Eu_{0.06}O_3$ ceramic with the transparency of 72.8% at the wavelength of 610 nm was the first commercialized polycrystalline scintillator used in medical x-ray detectors by General Electric Company. Despite previous works on Y_2O_3-based ceramic scintillators in the past three decades, high transparency in the visible-light region is still difficult to achieve. Vacuum sintering is a cost-effective technique for fabricating transparent ceramics but requires sinterable powders, properties of which are significantly affected by their precursors.

The main objective of this thesis is to highlight the applicability of powder processing technique for fabricating highly transparent Y_2O_3-based ceramics via vacuum sintering and to reveal the underlying mechanisms of particle formation, sintering behavior and optical performance. The readily sinterable oxide powders with significantly reduced hard agglomoration made in this work are successfully densified into highly transparent ceramics with fairly small grain size, which can be applied in various optical and thermodynamic fields. The following is the accomplishment of this thesis ī

Ammonium hydrogen carbonate precipitation route for yielding red $(Gd,Ln)_2O_3$:Eu (Ln=Y, Lu) phosphors and transparent Y_2O_3:Eu ceramics (Chapter Ⅱ)

Synthesis of $(Gd_{0.95-x}Ln_xEu_{0.05})_2O_3$ (Ln=Y and Lu, x=0-0.95) phosphor particles via ammonium hydrogen carbonate (AHC) precipitation has been systematically studied. Different nucleation kinetics exists in the Gd-Y-Eu and Gd-Lu-Eu ternary systems (Y^{3+} < Gd^{3+} < Eu^{3+} < Lu^{3+}), which leads to various morphologies and particle sizes of the precipitated precursors. The resultant oxide powders are ultrafine, narrow in size distribution, well dispersed and rounded in particle shape. Lattice parameters of the two kinds of oxide solid solutions linearly decrease at a higher Y^{3+} or Lu^{3+} content. Their theoretical densities linearly decrease with increasing Y^{3+} incorporation, but increase along with more Lu^{3+} addition. The two kinds of phosphors exhibit typical red emissions at ~613 nm and their charge transfer bands blue shift at a higher Y^{3+} or Lu^{3+} concentration. PL/PLE intensities and external quantum efficiency are found to decrease with increasing x value. Elevated calcination temperature enhances the PL intensity and the external quantum efficiency but lowers the lifetime of the phosphors.

Transparent $(Y_{0.95}Eu_{0.05})_2O_3$ ceramics with the transmittances of 22.8-60.9% at the wavelength of 613 nm Eu^{3+} emission were fabricated by further optimized parameter for particle synthesis. However, low AHC content induced a cationic component deviation for Y/Eu binary system albeit led to a higher ceramic transparency.

Synthesis of layered rare-earth hydroxide nanosheets leading to highly transparent Y_2O_3:Eu ceramics (Chapter Ⅲ)

Layered rare-earth hydroxide (LRH, $Ln_2(OH)_5NO_3{\cdot}nH_2O$, Ln=$Y_{0.95}Eu_{0.05}$) nanosheets (up to 7 nm thick) for the Y/Eu binary system, with the interlayer NO_3^- exchangeable with SO_4^{2-}, have been synthesized via chemical precipitation at the freezing temperature of ~4 °C. Calcining the sulfate derivative at 1100 °C for 4 h produces well dispersed and readily sinterable Ln_2O_3 red phosphor powders (~14.8 m^2/g) that can be

densified into highly transparent ceramics via vacuum sintering at the relatively low temperature of 1700 °C for 4 h (average grain size ~14 εm; in-line transmittance ~80% at the 613 nm Eu^{3+} emission). The extent of SO_4^{2-} exchange and the interlayer distance of LRH are both affected by the SO_4^{2-}/Ln^{3+} molar ratio (*R*), and an almost complete exchange is achievable at *R*=0.25 as expected from the chemical formula (one SO_4^{2-} replaces two NO_3^- for charge balance). The Ln^{3+} concentration for LRH synthesis substantially affects properties of the resultant oxides, and hard agglomeration has been significantly reduced at the optimized Ln^{3+} concentration of 0.05-0.075 mol/L.

Sulfate exchange significantly alters the thermal decomposition pathway of LRH, and was demonstrated to be essential to produce well dispersed and highly sinterable oxide powders. Slower heating in the ramp stage of vacuum sintering benefits optical quality of the final ceramic and the optimal sintering temperature is 1700 °C. Both the oxide powders and transparent ceramics exhibit the typical red emission of Eu^{3+} at ~613 nm under charge transfer (CT) excitation. Red-shifted CT band center, stronger excitation/emission, and shorter fluorescence lifetime were, however, observed for the transparent ceramic bodies.

Effects of Gd substitution on sintering and optical properties of highly transparent $(Y,Gd)_2O_3$:Eu ceramics (Chapter IV)

Highly transparent $(Y_{0.95-x}Gd_xEu_{0.05})_2O_3$ (*x*=0.15-0.55) ceramics were fabricated by vacuum sintering with the in-line transmittances of 73.6-79.5% at the Eu^{3+} emission wavelength of 613 nm (~91.9-99.3% of the theoretical transmittance of $Y_{1.34}Gd_{0.6}Eu_{0.06}O_3$ single crystal), while the *x*=0.65 ceramic undergoes a phase transformation at 1650 °C and has a transparency of 53.4% at the lower sintering temperature of 1625 °C. The effects of Gd^{3+} substitution for Y^{3+} on the particle properties, sintering kinetics and optical performances of the materials were systematically studied.

Wet chemical precipitation and sulfate-ion exchange yielded layered LRH nanosheets of the ternary Y-Gd-Eu system and their interlayer distances were significantly affected by the combined factors of layer charge density, hydrogen bonding and geometry of the interlayer anions. Calcining the layered LRH precursors yielded rounded oxide particles with greatly reduced hard agglomeration and the particle/crystallite size slightly decreases along with increasing Gd^{3+} incorporation. In the temperature range of 1100-1480 °C, the sintering kinetics of $(Y_{0.95-x}Gd_xEu_{0.05})_2O_3$ is mainly controlled by grain boundary diffusion with similar activation energies of ~230 kJ/mol. Gd^{3+} addition promotes grain growth and densification in the temperature range of 1100-1400 °C. The bandgap energies of the $(Y_{0.95-x}Gd_xEu_{0.05})_2O_3$ ceramics generally decrease with increasing *x*; however, they are much lower than those of the oxide powders. Both the oxide powders and the transparent ceramics exhibit the characteristic red emission of Eu^{3+} at ~613 nm under charge transfer excitation. Gd^{3+} incorporation enhances the photoluminescence and shortens the fluorescence lifetime of Eu^{3+}.

Fabrication of transparent Y_2O_3:Tb,Eu ceramics with color-tunable emission (Chapter V)

Transparent $(Y_{0.98-x}Tb_{0.02}Eu_x)_2O_3$ (*x*=0-0.04) ceramics with color-tunable emission have been successfully fabricated by vacuum sintering at the relatively low temperature of 1700 °C for 4 h. These ceramics have the in-line transmittances of ~73-76% at 613 nm, the wavelength of Eu^{3+} emission (the $^5D_0$Ÿ $^7F_2$ transition). Thermodynamic calculation indicates that the Tb^{4+} ions in the starting oxide powder can essentially be reduced to Tb^{3+} under ~10^{-3} Pa (the pressure for vacuum sintering) when the temperature is

above ~394 °C. The photoluminescence excitation spectra of the transparent $(Y_{0.98-x}Tb_{0.02}Eu_x)_2O_3$ ceramics exhibit one spin-forbidden (high-spin, HS) band at ~323 nm and two spin-allowed (low-spin, LS) bands at ~303 and 281 nm. Improved emissions were observed for both Eu^{3+} and Tb^{3+} by varying the excitation wavelength from 270 to 323 nm, without notably changing the color coordinates of the whole emission. The transparent $(Y_{0.98}Tb_{0.02})_2O_3$ ceramic exhibits the typical green emission of 544 nm Tb^{3+} (the $^5D_4$Ÿ $^7F_5$ transition). With increasing Eu^{3+} incorporation, the emission color of the $(Y_{0.98-x}Tb_{0.02}Eu_x)_2O_3$ ceramics can be precisely tuned from yellowish green to reddish orange via the effective energy transfer from Tb^{3+} to Eu^{3+}. At the maximum Eu^{3+} emission intensity (x=0.02), the ceramic shows a high energy transfer efficiency of ~85.3%. The fluorescence lifetimes of both the 544 nm Tb^{3+} and 613 nm Eu^{3+} emissions were found to decrease with increasing Eu^{3+} concentration.

Acknowledgements

As I look back my three-year Ph.D. life to study and work abroad in Japan, I found it was a really memorable period, during which I harvest so much knowledge and friendship and get to know many philosophy of life.

This thesis could be favourably accomplished owing to Prof. Yoshio Sakkaôs and Dr. Ji-Guang Liôs supervisions. They have abundant knowledge in the field of material science, give me many advices, ideas, supports and patience, and cultivate my systems thinking and rigorous academic attitude for scientific research that will make me lifelong benefit.

I gratefully acknowledge the China Scholar Council (CSC) for financial support during my Ph.D. period at University of Tsukuba, Japan. I feel very fortunate and glorious to become a Ph.D. student of Graduate School of Pure and Applied Sciences, University of Tsukuba and to be able to work at Materials Processing Unit, National Institute for Materials Science (NIMS), Japan.

Sincere thanks and best wishes are given to my reviewers, Prof. Takashi Sekiguchi, Prof. Hisanori Tanimoto and Prof. Kazuaki Sakoda for reviewing my thesis, proposing instructive suggestions and giving kind guidance.

I greatly appreciate Dr. Tohru S. Suzuki and Dr. Hideo Okuyama. They know everything and ensure all the research facilities in good condition so that our experiments could go well and we can obtain accurately scientific data.

Special thanks are due to the Materials Analysis Station and World Premier International Center for Materials Nanoarchitectonics (WPI-MANA) of National Institute for Materials Science (NIMS) for performing elemental analysis and allowing for access research facilities. Dr. Makito Nakatsu and Kiyotaka Iiyama patiently taught me how to use the analysis equipment.

I feel very lucky to get to know Mr. Kento Imai, Mr. Shotaro Musha, Mr. Kenya Hirai, Mr. Yuki Shimura and Mr. Yukihito Igarashi. They all very kind and give me enthusiastic introduction to Japanese culture and experimental help.

I would like to express my gratitude to Dr. Mrinalini Mishra, Dr. Wen-Wen Wu, Dr. Chika Matsunaga Dr. Chengjun Pan and Dr. Jin Nakamura for their selfless assistance.

I am very grateful to Dr. Renzhi Ma, Dr. De-Hai Ping, Dr. Chunfeng Hu and Dr. Mehdi Estili for technical support and good discussion.

I am so thankful to Mrs. Yuko Yamaguchi and Mrs. Masako Tamiya for their warm assistance in my daily life and matters.

I also would like to give my sincere gratitude to my friends and my fellow classmates who gave me their time in listening to me and helping me.

Most important of all, I would like to express my great appreciation and best wishes to my family for their love and support in all my life.

Thanks to every one

Bin Lu

Contents

Chapter Ⅰ

Introduction

- **Phosphor**
- **Luminescence**
- **Ceramic scintillator**
- **Layered rare-earth hydroxide**

1.1 Phosphors

Luminescent materials, usually known as ñphosphor materialsò or ñphosphorsò, are the chemical compounds that exhibit the optical phenomenon of luminescence upon stimulation or excitation by electromagnetic radiation. Most inorganic phosphors are consisted of a host crystal material and one or more intentionally introduced impurities, called activators. Activators doped into the host crystal are functional as the luminescent centre. The concentration of activators can be as low as tens of ppm, such as for donor acceptors, or can also be as high as 20% for rare-earth dopants. All of those elements employed as the host lattice and/or as activator as well as the plasma elements are given in the periodic table of the ñlightingò elements as shown in Fig. 1.1.[1]

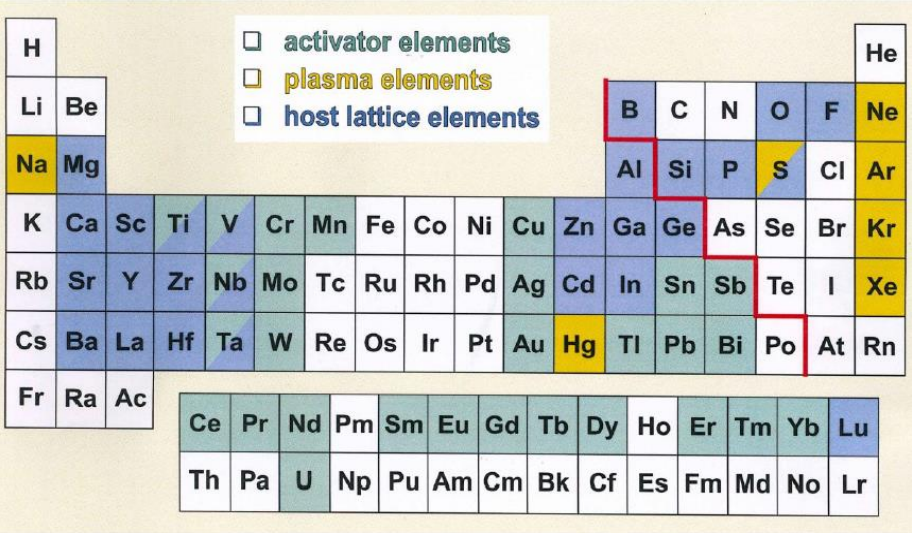

Fig. 1.1 Periodic table of the "lighting" elements.

The lanthanide series includes elements from atomic number 57 (La) to 71 (Lu), which is 15 elements. However, Y element is generally regarded as one more member of the lanthanide family, because the ionic radius of Y^{3+} (0.0900 nm) is close to that of Ho^{3+} (0.0901 nm),[2] leading to similar chemical properties. With the exception of La^{3+}, Y^{3+} and Lu^{3+}, all of Ln^{3+} ions are luminescent and their emission lines cover the entire spectrum, from UV (Gd^{3+}) to visible (e.g. Eu^{3+}, Pr^{3+}, Sm^{3+}, Tb^{3+}, Dy^{3+}, Tm^{3+}) and near-infrared (e.g. Pr^{3+}, Nd^{3+}, Ho^{3+}, Er^{3+}, Yb^{3+}) ranges. Ln^{3+} benefits from their characteristic incompletely filled 4*f* shell and exhibit unique optic, electric and magnetic properties. In the rare earth elements, the 4*f* electrons are shielded from the surroundings by the $5s^2$ and $5p^6$ electrons. Therefore, the optical transitions within the 4*f* configuration are hardly influenced by the environmental or crystal electric field except Ce^{3+}. The energy level diagram of 4*f* electrons of the trivalent rare earth ions was given out by Dieke et al.[3] (Appendix Fig. 1), in which the energy states were experimentally determined by considering the optical spectra of individual ions incorporated in $LaCl_3$ crystals. Light-emitting levels are indicated by semicircles below the bars. The width of the energy state bars gives the order of magnitude of the crystal field splitting, which is very small. The diagram is applicable to ions in almost all of the host lattices, because the 4*f* electrons hardly interact with the environmental electric field. The maximum variation of the energy states is very confined and is at most of the order of several hundred cm^{-1}.

Eu^{3+} as one of the key rare-earth activators has the red emission band of the trivalent oxidation state located at ~613 nm with a relatively highly photopic response of ~44%. Eu^{3+} has been incorporated into many host crystals for developing red light emitting phosphors, such as Ln_2O_3,[4-10] $LnVO_4$,[11,12] Ln_2O_2S,[13-15] $Ln_2O_2SO_4$,[16,17] etc. Eu^{3+}-activated red sesquioxide phosphors have in particular attracted considerable interest due to their high chemical durability and thermal stability, and are being extensively applied in various lighting and display systems, such as fluorescent lamp, white LED, high-resolution x-ray imaging detector, field emission display, flat-panel display, plasma display panel, and cathode-ray tube, and also in the fabrication of ceramic scintillator.[3-7] The phosphors display characteristic Eu^{3+} red emissions upon UV excitation into the charge transfer (CT) band arising from 2*p* orbital of O^{2-} to the 4*f* orbital of Eu^{3+}. Improved property of displays requires high-quality phosphors for high brightness and resolution with long-term stability. Phosphor particles of spherical shape, ultrafine size, good dispersion and narrow size distribution are desired owing to three reasons: (1) spherical powder can form a denser phosphor layer by close packing, but also minimizes the light scattering on particle surface to enhance the efficiency of photoluminescence (PL) and brightness;[18] (2) ultrafine powders provide small pixel sizes for improved resolution;[19-21] (3) well-dispersed and narrow size-distributed particles produce uniform luminescence over the whole phosphor screen.[22,23]

1.2 Luminescence

1.2.1 Classification

Luminescence can be distinguished by the various excitation sources, such as PL, CL, XL, EL and so forth (Tab. 1.1). [1,26]

Table 1.1. Different types of luminescence.

Luminescence type	Excitayion scource	Applications
photoluminescence (PL)	(UV) photons	fluorescent lamps, plasma displays
cathodoluminescence (CL)	electron beams	TV sets, monitors
x-ray luminescence (XL)	x-rays	scintillators
electroluminescence (EL)	electric current	LEDs, EL displays
chemoluminescence	chemical reaction energy	analytical chemistry
bioluminescence	biochemical reaction energy	analytical chemistry
sonoluminescence	ultrasound	ī
triboluminescence	mechanical energy	ī
fractoluminescence	fracture in certain crystals	ī
piezoluminescence	pressure on certain solids	ī

Luminescence can also be divided into phosphorescence and fluorescence by the difference in decay times[24] Fluorescence denotes an emission with a short decay time from ~10^{-6} to 10^{-4} ms, while phosphorescence is used to stand for the emission of a much longer decay time from a few minutes up to several hours.[25] According to quantum theory, in a fluorescence process, transitions arise from the singlet excited state where the electron does not change its spin direction. Whereas, sometimes under the appropriate

conditions a spin-flip could happen and a lower triplet excited state is created, which is the case in a phosphorescence process. Transitions from a triplet excited state are forbidden by the selection rules and have to wait for a long time until the electron spin flips back. Therefore, compared with fluorescence, phosphorescence is frequently of low intensity and could last for a while after the removal of the excitation source.

1.2.2 Luminescence process

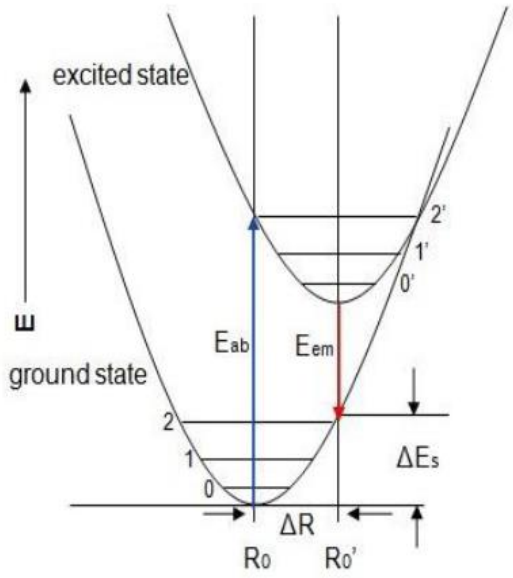

Fig. 1.2 Configurational coordinate diagram.

The configurational coordinate diagram frequently was utilized for explanation of the luminescence process as shown in Fig. 1.2, from which the potential energy E is plotted as a function of the configurational coordinate R, where R represents the distance between the luminescence centre and its coordinate neighbour. Optical transitions are represented vertically in the configurational coordinate diagram, because they are electronic and occur rapidly compared to nuclear motions. The ground state and excited state are shown in the form of parabolic potential wells. The luminescence centre is prompted from its ground state to an excited state after absorbing energy E_{ab}. The luminescence centres tend to stay in the minimum energy points of the excited state before a possible optical transition can occur. The difference between E_{ab} and the emission energy E_{em} is called the Stokes shift, denoted ΔE_s. It is also shown in Fig. 1.2, where there is a shift of ΔR between the minimum energy point of the ground state and excited state, since the chemical bond in the excited state is different from that in the ground state.

1.2.3 Concentration quenching

Quenching is a phenomenon of the reduction in radiative emission for the luminescent materials and can be caused by external factors such as an increase in temperature, or stoichiometric factors such as an increased amount of activator or sensitiser in the lattice (i.e. concentration quenching).

For the concentration quenching, the quenching tends to occur with the increasing concentration of an activator, as a result that there is a significant reduction in the average distance between these luminescent

centres. Concentration quenching can be attributed to pairing or aggregation of the activator ions, resulting in an increase in the non-radiative losses. This non-radiative decay may be induced by many possible factors, the most common of which include lattice defects. Lattice defects frequently act as sites where the energy is lost by non-radiative/cross relaxation between the activators and impurities.

1.2.4 Cross-relaxation

Cross-relaxation (also called self-quenching) is an energy transfer process between identical ions. In most case, the same kinds of ions are both a sensitizer and an activator. The rare earth ions frequently give rise to this kind of energy transfer owing to their complicated energy level structure.

Cross-relaxation process may become a major problem for quenching at a higher activator concentration. It may also occur between differing elements which have two pairs of energy levels separated by the same amount. The two bandgap energies may be equal or can be matched by one or two phonons. This process has been observed in many ions and it is a main factor in non-radiative relaxations especially at high concentrations.[27]

1.2.5 Energy transfer

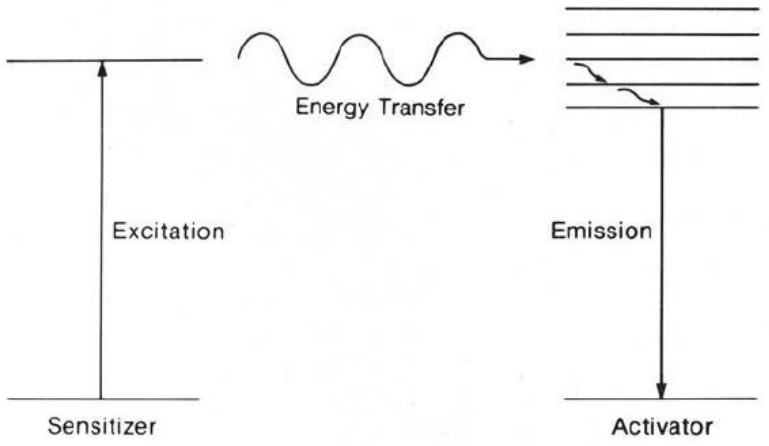

Fig. 1.3 Schematic diagram illustrating energy transfer between a sensitizer and activator.

Energy transfer is the radiative transition process by which the excitation center (host, activator or sensitizer) transfers the energy to luminescent center. Therefore, the improved luminescence of the phosphor can be achieved via energy transfer process between the donor and the acceptor. In a typical schematic diagram as shown in Fig. 1.3,[28] a donor is firstly excited to an upper energy level by absorbing the incident radiation (excitation source) on the phosphor. This excitation energy is then transferred (the electrons of donor returns to its ground state) by exciting an adjacent acceptor whose electrons then back-jump to its ground state with a phenomenon of luminescence emission. Such a transfer process is called non-radiative energy transfer. The donor and acceptor have excited state levels of approximately equal energy above their ground states, and the activator and sensitizer must be close enough in the host lattice for the transfer probability to be appreciable. The energy transfer process can occur when the emission line of the donor overlaps the absorption line of the acceptor. In the case of lack of spectral overlap, energy transfer may also take place via resonance condition (equal energy difference between the energy levels of the acceptor and the donor) and/or phonon mediated processes.

The theory of energy transfer resonance derived by Dexter et al.[29] has revealed that two luminescence centres, a donor and an acceptor (A and D) within a certain distance (*R*) with a certain interaction (i.e. exchange or multipole-multipole interaction) may be in resonance and transfer excitation energy from donor to acceptor. It depends on the average distance (*R*) between the donor and acceptor ions. Exchange interaction generally requires an *R* value of less than 0.3ï 0.4 nm; otherwise, the electric multipole interaction may dominate. The average separation *R* can be estimated from the following equation proposed by Blasse as follows:[30]

$$R = 2(\frac{3V}{4\pi X_C N})^{1/3} \qquad (1.1)$$

where *Xc* is the total concentration of the donor and acceptor ions, *N* is the cation number in the unit cell, *V* is the cell volume.

1.3 Yttria (Y_2O_3)

1.3.1 Crystal structure

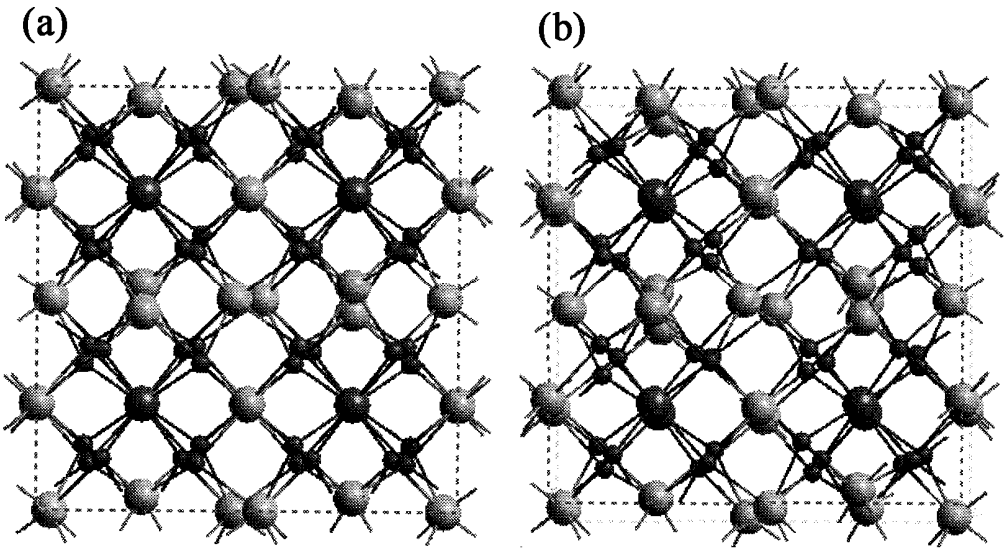

Fig. 1.4 Crystal structure of Y_2O_3. Along the [001] direction (a) and in a direction slightly deviated from [001] (b). The large light (dark) ball is for Y1 (Y2), and the smaller one is for O.

The crystal structure for yttria (Y_2O_3) is shown in Fig. 1.4.[31] The crystal structure of Y_2O_3 used in phosphors application is a body-centered cube of space group *Ia*3-(T^7_h) (No. 206). The cubic Y_2O_3 crystal belongs to C-type sesquioxide lattice, which has a total of 80 atoms per unit cell including 32 yttrium atoms and 48 oxygen atoms. The unit cell contains two inequivalent cation sites, that is, Y1 at the 8*a* site and Y2 at the 24*d* site, and one type of oxygen at the 48*e* site. The fluoritelike structure, named after the mineral bixbyite, can best be viewed as consisting of 64 slightly distorted mini-cubes with yttrium atoms sitting at the centers of 32 of the mini-cubes. The oxygen atoms are at six of the eight corners of the cube such that an approximate octahedral coordination for the cation is maintained. The missing oxygen atoms are either at the face diagonal (75%) or at the end of the body diagonal (25%) of the mini-cube. For mini-cubes having Y1 at the center, three oxygen atoms are at one face of the cube, and the other three oxygen atoms are at the opposite face. There are six equal Y1-O bonds of 0.2261 nm. For mini-cubes containing Y2, four oxygen

atoms are at one face and the other two at the opposite face. There are three different pairs of Y2-O bonds of 0.2249, 0.2278, and 0.2336 nm in length. On average, the Y1-O bonds are slightly shorter than the Y2-O bonds. Each oxygen atom is linked to one Y1 and three Y2 atoms in the form of a distorted tetrahedron. The shortest O-O separations are 0.2865 and 0.2927 nm. Figure 1.5 exhibits the two Y^{3+} sites in the lattice. Two of the corners are vacant and can be along a body or face diagonal of the cube which results in two Y^{3+} site symmetries called S_6 and C_2 ,respectively it is believed that the activators substitute these Y^{3+} sites. The ratio of C_2 to S_6 sites is 3 to 1.

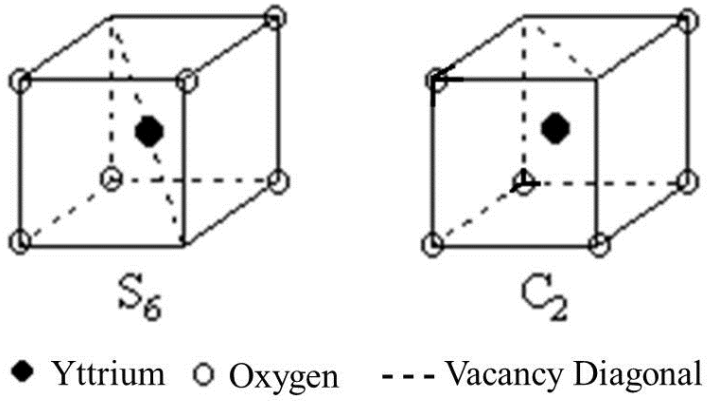

Fig. 1.5 The two Y^{3+} crystallographic symmetry sites in cubic Y_2O_3 lattice.

1.3.2 Properties

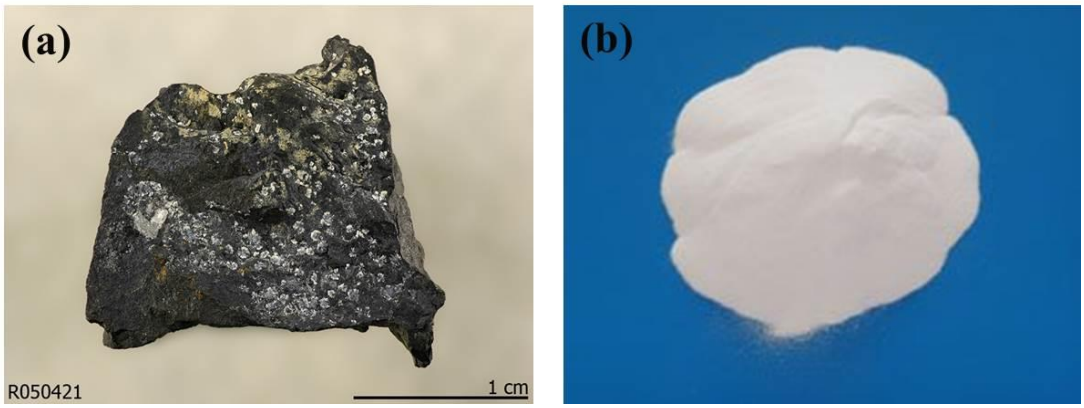

Fig. 1.6 Appearances of YPO_4 crystal (a) and Y_2O_3 powder (b).

Y_2O_3 is mainly extracted from the mineral Xenotime ($YPO_4·2H_2O$) as shown in Fig. 1.6. It is a refractory material with a high melting point of 2430 ºC. It has less thermal expansion than alumina, magnesia and zirconium.[32] It is soluble in acids and slightly soluble in water. The availably commercial products are in various purities between 99.9% and 99.999%.

Its properties include high thermal stability with a temperature of crystallographic stability up to 2325 ºC and good transparency to infrared radiation. It has an affinity for oxygen and sulphur and is used as an additive to stabilize zirconia and as a sintering aid in silicon nitride. As an optical ceramic, it transmits well in the infrared range, from 1 to 8 εm wavelength. The high infrared transmission, together with good resistance to erosion and thermal shock, makes it ideal for protection domes for infrared sensors. Y_2O_3 also is

an attractive host material used as a scintillator/ laser owing to its low cost, high dielectric constant (14-18), large band gap (5.6 eV), high melting point, high thermal conductivity (13.6 W/mK), refractive index (n_H=1.93 at λ=613 nm), high thermal stability, low phonon energy (380 cm-1), and good resistance to erosion and thermal shock.[33-35]

1.4 Transparent ceramic scintillators

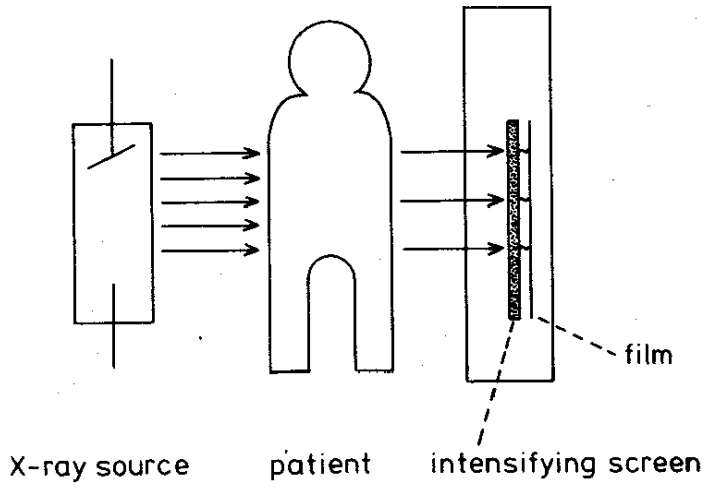

Fig. 1.7 Schematic representation of a medical radiography system .

Polycrystalline transparent ceramics have extensive applications in various areas, such as infrared windows/domes, lamp envelopes, transparent armors and laser and scintillator hosts.[36] By properly doping with activator ions, transparent ceramic scintillators may be attained by employing advanced powder processing and ceramic sintering techniques. Transparent ceramic scintillator is being widely developed to replace the conventional single crystal one due to the advantages of low cost, high dopant concentration, large-size and mass production and near-neat shaping. The materials can absorb and convert x-rays into visible photons to be applied in radiation detectors for medical diagnostics, industrial inspection, dosimetry, nuclear medicine and high-energy physics (Fig. 1.7).[37-39]

1.4.1 Properties

In order to achieve high-quality imaging and reduce the need to subject patientsô bodies to x-ray radiation, a high-efficiency scintillator should exhibit a high absorption coefficient for x-rays, high transparency, high light output, a short decay time and low radiation damage.[40] The detailed descriptions are list as follows:

(1) Absorption coefficient. If the x-ray photons are allowed to pass through the scintillator without absorption and creation of excitons that excite luminescent centers, the efficiency of the x-ray detection is diminished and also degrades the performance of the detection system. As the relation between the absorption coefficient (η_{abs}), theoretical density (ρ), and effective atomic number (Z_{eff}) can be expressed as $\eta_{abs}=\rho Z_{eff}^4$, a high theoretical density and atomic number are thus essential for a scintillator.

(2) Transparency. The transparency of the scintillator material is critical because the visible scintillation photon must be transported efficiently to the photodetector. The isotropically visible photon

emitted by scintillation must be transported to the photodetector by a combination of reflection and scattering at surfaces, as well as scattering within the material. Minimization of the visible photon path length is critical for scintillators that have intrinsic optical absorption at the emission wavelength because this results in efficiency losses due to self-absorption. Residual pores in the microstructure of the ceramics, however, can act as efficient scattering centers to weaken the effective photon transfer, and hence high transmittance for a scintillator is critical.

(3) Light output. Light output depends on the absorption coefficient of the scintillator at the X-ray excitation energy, the efficiency of exciton creation and capture at the luminescent centers, the intrinsic emission quantum efficiency of these centers, the scintillator geometry (surface structure and reflectors) and transparency, and the quantum efficiency of the diode at the emission wavelength.

(4) Decay time. Delayed emission from the scintillator after the incident X-ray beam is highly attenuated by the object being imaged can degrade image quality and reduce image resolution. The relationships between decay time and fluorescence lifetime can be expressed as $I=Aexp(-t/\tau)+B$, where I is the emission intensity, τ is the fluorescence lifetime, t is the decay time and A and B are constants. Therefore, the decay time/lifetime reflects the response time of the scintillator and also plays an important role in its system.

(5) Radiation damage. Stability and reproducibility of light output of a scintillator are critical to many applications. Radiation damage refers to the change of scintillation efficiency due to defect creation by the radiation dose. These defects are commonly color centers whose electronic structure imparts optical absorption bands at the scintillator emission wavelengths. As in the case of afterglow, the binding energy of the color center determines the longevity of the damage. In general, this energy is sufficiently large that damage can last from seconds to days at room temperature. Although radiation damage typically decreases the scintillation efficiency, there are exceptional cases where the efficiency increases. This is likely attributed to the modification or neutralization of defect centers that otherwise reduce the scintillatorôs quantum efficiency.

1.4.2 Sintering techniques

Polycrystalline transparent ceramics (including ceramic scintillators) are frequently fabricated by hot pressing (HP), hot isostatic pressing (HIP) and pressureless sintering (vacuum or atmosphere-controlled sintering). Compared with HP and HIP, pressureless sintering is cost effective and time efficient but requires sinterable powders.[41,42] Podowitz et al.[43] fabricated transparent Y_2O_3:Eu ceramics with a transmittance of ~71% at the wavelength of ~613 nm by HP plus HIP. Lu et al.[44] produced transparent Eu:$Y_{1.8}La_{0.2}O_3$ ceramics with the highest transmittance close to 80% over the wavelength range of 190-1400 nm and an approximate grain size of 55 μm via hydrogen sintering. Bagayev et al.[45] produced Y_2O_3-based ceramics with a highest transparency of ~81% at 1079 nm and average grain sizes of 1-130 μm by vacuum sintering at 1700-1950 °C for 10-20 h. Other sintering techniques also have been developed to produce transparent ceramics and have their respective advantages, including spark plasma sintering,[46,47] microwave sintering,[48] millimetre-wave sintering[49] and laser sintering,[50] but may find difficulties in fabricating the thick bulk of high transmittance in the visible region. Zhang et al.[46] fabricated transparent Y_2O_3 ceramics with a transmittance of 68% at the wavelength of 700 nm and a fine grain size of ~400 nm by spark plasma sintering. Esposito et al.[48] produced transparent YAG:Yb laser ceramics with a highest transparency of 65% in the wavelength region of 200-1100 nm and a grain size of 5-20 μm in a 24 GHz and 6 kW microwave

furnace. Ji et al.[50] made transparent Ta_2O_5 dielectric ceramics with a transparency up to 35% at 270-3000 nm using a CO_2 laser with a maximum power output of 2.5 kW.

1.4.3 Research progress

General Electric (GE) Company produced the first commercialized polycrystalline transparent ceramic scintillators with the composition of $Y_{1.34}Gd_{0.6}Eu_{0.06}O_3$ that successfully were used in premium X-ray CT.[33] This material possesses a transparency of ~72.8% and an average grain size of 30 μm at the wavelength of 610 nm. Some other types of ceramic scintillators were sequentially developed by GE, such as $Gd_3Ga_{4.96}Cr_{0.04}O_{12}$, $(Y,Gd)_2O_3$:Eu,Pr, Gd_2O_2S:Pr,Ce,F, $Gd_3Ga_5O_{12}$:Cr,Ce, $BaHfO_3$:Ce, etc. Recently, the other institutes and researchers also carried out relative studies.[51-61] Kim et al.[51] fabricated a $Gd_{1.54}Y_{0.4}Eu_{0.06}O_3$ ceramic scintillator with a low transparency, however, to achieve about higher light output than the $CdWO_4$ single crystal. Shen et al.[52] produced a LuAG ceramic scintillator with a transparency close to 80% in the visible range via vacuum sintering at 1800 °C for 10-20 h and addition of sintering aid of 0.01 wt% MgO and 0.2 wt% tetraethyl-ortho-silicate (TEOS). Li et al.[55] made a transparent $Y_{0.6}Gd_{1.34}Eu_{0.06}O_3$ ceramic scintillator with a transparency of 67.7% at the wavelength of 610 nm and a grain size of ~52 μm by vacuum sintering at 1670 °C. Apparently, the reports for high-quality Y_2O_3-based ceramic scintillator are relatively few and it is necessary to find a better way for synthesis readily sinterable powders for fabricating effective scintillators.

1.5 Layered rare-earth hydroxides

1.5.1 Feature and application

The layered double hydroxides (LDHs) with a generic formula of $[M^{2+}_{1-x}M^{3+}_x(OH)_2][A^{n-}]_{x/n}\cdot zH_2O$, have been widely studied, where M^{2+} may include Mg^{2+}, Zn^{2+} or Ni^{2+}, M^{3+} may be selected from Al^{3+}, Ga^{3+}, Fe^{3+} or Mn^{3+}, A^{n-} is a nonframework charge compensating inorganic or organic anion, e.g. CO_3^{2-}, Cl^-, SO_4^{2-}, RCO_2^-, and x is normally between 0.2– 0.4.[62] A breakthrough came in 2006 when Gandara et al.[63] found interlayer-anion exchangeable layered rare-earth hydroxides (LRHs) two-dimensional (2*D*) nanosheet morphology. Since then, LRHs have attracted considerable attention.[64-68] The LRHs not only have the similar ion exchange, intercalation and delamination properties with LDHs, but also have optical, electrical, magnetic and catalytic of trivalent rare-earth cations. LRHs thus have extensive applications in interlayer chemistry luminescence, catalysis and medical fields.[68]

(1) Interlayer chemistry. Anion exchange, which is unusual for inorganic materials, has wide industrial application. The anion selectivities have been given by Miyata et al.[69] in the sequence $I^- < NO_3^- < Br^- < Cl^- < F^- < OH^- < SO_4^{2-} < NYS^{2-}$ (Naphthol Yellow S) $< CO_3^{2-}$, and hence the interlayered monovalent anion is readily ion-exchanged by divalent anion. It is known that layered materials tend to swell and exfoliate into nanosheets in water or organic solvent under certain conditions. Similar to the procedures applicable for LDHs, the LRHs can be delaminated into single/few-layer nanosheets in formamide after exchanging the interlayer anions with larger organic ion.

(2) Photoluminescence Behavior. Much effort has been invested in the development of new materials exhibiting emissions in the visible region. Lanthanide family involves varied activator ions. Pr^{3+}, Sm^{3+}, Eu^{3+}, Tb^{3+}, Dy^{3+}, Ho^{3+}, Er^{3+} and Tm^{3+} exhibit deep red, orange, red, green, yellow, green, green and blue emissions, respectively. The layered rare-earth hydroxides, with rare-earth centers in the host, represent a new class of luminescent or up-conversion luminescent materials after selected doping or codoping activator ions. One

problem is that water molecules and hydroxyls are directly coordinated to the lanthanide metal centers, which imposes a drastic quenching effect on the emissions, and thus the emissions are far from industrial requirements. One strategy to address this disadvantage involves post-treatment. Hu et al. demonstrated that densely packed $(Gd_{0.95}Eu_{0.05})_2O_3$ film from annealing treatment of $(Gd_{0.95}Eu_{0.05})_8(OH)_{20}Cl_4$˜7.2$H_2O$ exhibits emission intensity 527 times that of precursor powder samples.[70] Interestingly, the conversion is quasi-topotactic with a close metal arrangement between the (001) lattice plane of the precursor hydroxide and (111) plane ofannealed oxide crystals. Zhu et al.[71] prepared Highly [111] oriented, dense $(Y_{0.95}Eu_{0.05})_2O_3$ phosphor films (~60 nm thick) with excellent optical transparency (~86%) and a greatly enhanced luminescence intensity (~4 times that of the powder form) have been constructed via self-assembly of ultra-thin Y/Eu LRHs nanoplates (Fig.1.8).

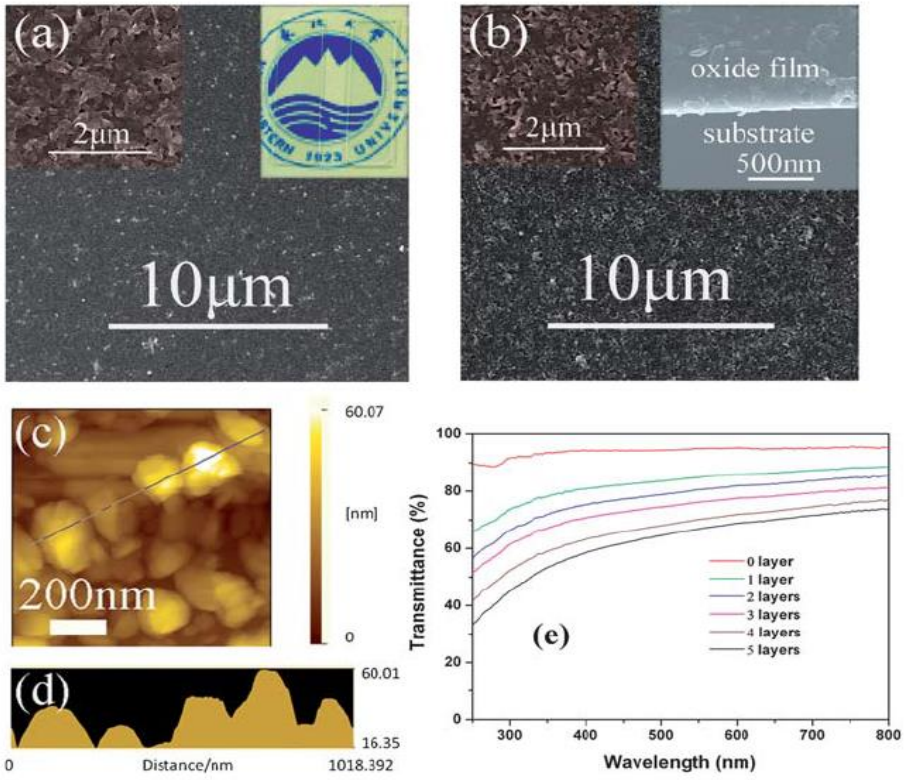

Fig. 1.8 Y/Eu LRH film (a) and the oxide film (b), its AFM image (c) and transmission spectra (d).

(3) Catalysis. Catalytic activity of lanthanide compounds is also a fascinating field. $Yb_8(OH)_{20}[C_{14}H_6O_2(SO_3)_2]_2$Å8$H_2O$ and $Y_8(OH)_{20}[C_{10}H_6(SO_3)_2]_2 \cdot 8H_2O$ with a great number of active centers and capability of varying the coordination number were reported to combine the catalytic properties of rare-earth atoms with the advantages of a solid catalyst, serving as excellent heterogeneous catalysts in green chemistry.[63,72]

(4) Medicine. The use of lanthanide complexes as a magnetic resonance imaging (MRI) contrast agent has proven to be invaluable in the diagnosis of several internal abnormalities. Among the lanthanide series, Gd^{3+} stands out because of its unique nature: high effective magnetic moment (seven unpaired electrons) and slow electronic relaxation rate from its symmetric *S*-state.[73,74] The potential application of the layered rare-earth hydroxides as a new MRI contrast agent was studied using an aqueous nanosheet suspension of $Gd_8(OH)_{20}Cl_4 \cdot 7.0H_2O$ by Lee et al.[75] The layered gadolinium hydroxide (LGdH) suspension exhibits a

sufficient contrast effect for T_1 weighted magnetic resonance imaging. This group subsequently developed a novel method for modifying the surface of magnetic-resonance-contrasting LGdH with water- and bio-compatibility and acid-resistance.[76] Firstly, the nitrate ion of $Gd_2(OH)_5NO_3 \cdot nH_2O$ was first exchanged with the oleate anion. And then, the delaminated layers were then modified with phospholipids with poly (ethylene glycol) (PEG) tail groups, resulting in a stable aqueous suspension of completely exfoliated layers having the ability for enhancing MRI contrast. Fluorescein (FS) anions were incorporated into the modified layers using the ready exchange of anions attached to an exfoliated layer forming a fluorescent colloid of LGdH, which allow the development of a multimodal probe combining optical and MR imaging. The scheme of the novel route is shown in Fig. 1.9.

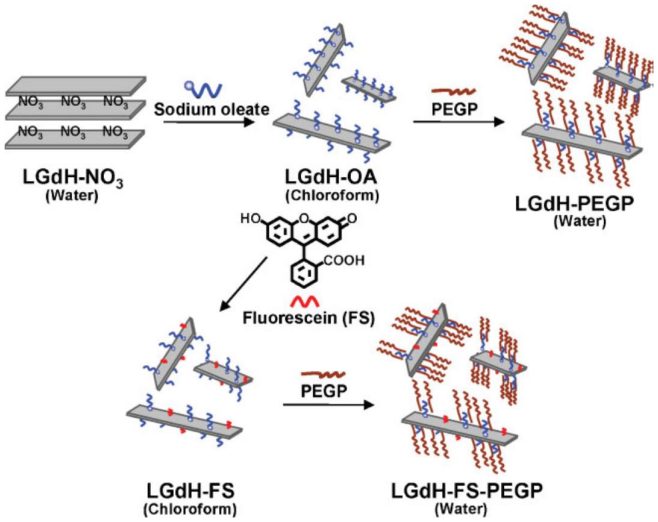

Fig. 1.9. The surface modification approach for fabricating LGdH-FS-PEGP.

1.5.2 Structure

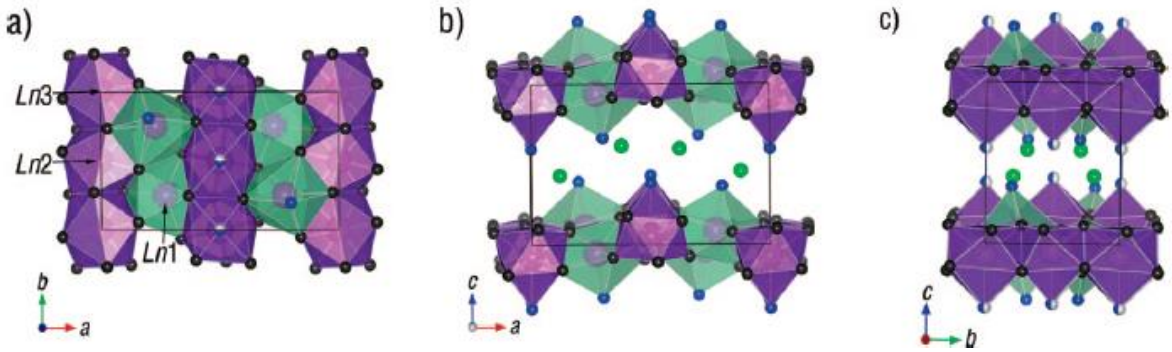

Fig. 1.10 $Ln_8(OH)_{20}Cl_4{}^{\sim}nH_2O$ unit cell viewed down the (a) c axis, (b) b axis, and (c) a axis.

LRHs with the orthorhombic cells and the general composition of $Ln_2(OH)_5A \cdot nH_2O$ or $Ln_8(OH)_{20}(A^{m-})_{4/m} \cdot nH_2O$ are composed of positively charged hydroxide layers of Ln^{3+} and exchangeable A^- anions located in the interlayer for charge balance, where A^- may include NO_3^-, Cl^- and Br^-[66,67] and Ln^{3+} may be selected from a wide range of the lanthanide family (including Y).[68,77,78] The orthorhombic cell viewing along the *c*, *b*, and *a* axes is shown in Fig. 1.10.[77] It can be seen that there are three crystallographically distinct sites for Ln

in the unit cell (shown as purple balls and labelled Ln1, Ln2, and Ln3), five distinct sites for hydroxyls, three for water molecules, and one unique site for chloride ions. Each hydroxyl acts as a μ_3-bridge connecting the lanthanide centers. All phases have two types of lanthanide metal environments containing 9- and 8-fold coordination corresponding local symmetries of C_1 and C_{4v}, respectively. Ln1 is surrounded by seven hydroxyls and one water molecule, $[Ln(OH)_7(H_2O)]$, forming a dodecahedron. The second lanthanide environment for Ln2 and Ln3 has oxygen atoms bonded to eight hydroxyls and one water molecule, $[Ln(OH)_8(H_2O)]$, forming a monocapped square antiprism with the capping position occupied by the water molecule. Each LnO_8 polyhedron is linked to two other LnO_8 polyhedra and four LnO_9 polyhedra via edges. These linked polyhedron units form a two-dimensional host layer parallel to the ab plane. One crystallographically unique A^- anion is located in the interlayer space. This indicates that the A^- ions are accommodated in the gallery as counterions typical for anionic clays.

1.5.3 Synthesis route

The reported routes for LRH synthesis include hydrothermal[63-66,79,80] and solvothermal[67] reactions and homogenous[77,78,81] and freezing-temperature precipitation.[82,83]

(1) Hydrothermal synthesis: It is a method to produce chemical compounds and materials using closed-system physical and chemical processes flowing in aqueous solutions at a fixed temperature and a pressure of above 1 atm. Gándara et al.[63] firstly prepared $Ln_8(OH)_{20}(A^{m-})_{4/m}\cdot nH_2O$ via hydrothermal synthesis. And then Fogg et al.[64,66] synthesized $Ln_2(OH)_5NO_3\cdot nH_2O$ (Ln=Y, Gd-Lu) and $Ln_2(OH)_5X\cdot 1.5H_2O$ (X = Cl, Br; Ln=Y, Dy, Er, Yb) LRHs, and investigated the ion-exchange properties. Zhu et al.[80] made $(Y_{1-x}Eu_x)_2(OH)_5NO_3\cdot nH_2O$ (x=0-1) and studied the Eu^{3+} effects on the resultant particle morphology, phase conversion to oxides and photoluminescence behaviors.

(2) Solvothermal reaction: Solvothermal reaction is very similar to the hydrothermal route, and the only difference being that the precursor solution is usually not aqueous. Lee et al.[67] obtained lager ion-radius $Ln_2(OH)_5NO_3\cdot nH_2O$ (Ln=Nd and La) by the solvothermal reaction using ethanol containing alkali-metal hydroxide (KOH, RbOH, or CsOH) as a solvothermal medium and demonstrated ion exchange reactions between NO_3^- and some organic anions such as decanoate, decanesulfonate and decylsulfate.

(3) Homogenous precipitation. Homogenous precipitation is a facile way for yielding various well-crystallized samples.[84-86] Lanthanide salts with anion source and hexamethylenetetramine (HMT) firstly were mixed and then the solution was heated at refluxing temperature with nitrogen gas protection for producing LRHs, by which the HMT slowly hydrolyze in acidic solution with the release of ammonia water and formaldehyde as follows:

$$(CH_2)_6N_4 + 10H_2O \rightarrow 4NH_4^+ + 4OH^- + 6HCHO$$

$$5OH^- + A^- + nH_2O + 2Ln^{3+} + nH_2O \rightarrow Ln_2(OH)_5A\cdot nH_2O$$

Geng et al.[77,78] systematically studied the products for all 15 cations (La-Lu as well as Y, except Pm) using the homogeneous precipitation to determine the formation range for the chloride and nitrate series as well as the crucial structural feature of LRHs. They obtained three different structures, such as $Ln(OH)_3$, the desired LRH phase, and other unknown phases for larger (La-Pr), intermediate (Nd-Tm, Y), and smaller lanthanides (Yb and Lu), respectively.

(4) Freezing temperature precipitation. The above mentioned three LRH synthesis routes frequently lead to thick plate-like crystallites with good crystallinity. Thick plates, however, are difficult to collapse upon calcination and the resultant oxides generally retain the plate-like morphology.[23,70] The crystal structure

of the LRH compounds can be viewed as a repetitive stacking of the host layer and interlayer anions along the *c*-axis (the [001] direction).[68] As the host layer is a close-packed low-energy crystal plane, the crystal preferentially grows up in a two-dimensional way, leading to the frequently observed plate-like morphologies. Moreover, crystal growth along the *c*-axis needs much higher activation energy. Supressing thickness growth along the [001] direction would thus be a feasible choice to produce nanosheets at low temperature. Wu et al.[82,83] directly produce nitrate-type LRH nanosheets of down to ~3 nm in thickness for a wide spectrum of Ln (Ln = Pr, Nd, Sm, Eu, Gd, Tb, Dy, Y, Ho, and Er), in large batch quantity (0.025 mol of $Ln_2(OH)_5NO_3{}^{\sim}nH_2O$) and via chemical precipitation at the freezing temperature without using any mineralizer. Based on this, we think freezing temperature synthesis may thus be a feasible way to acquire well-dispersed oxide powders from the ultrathin nanosheets.

1.6 Motivation and methodology

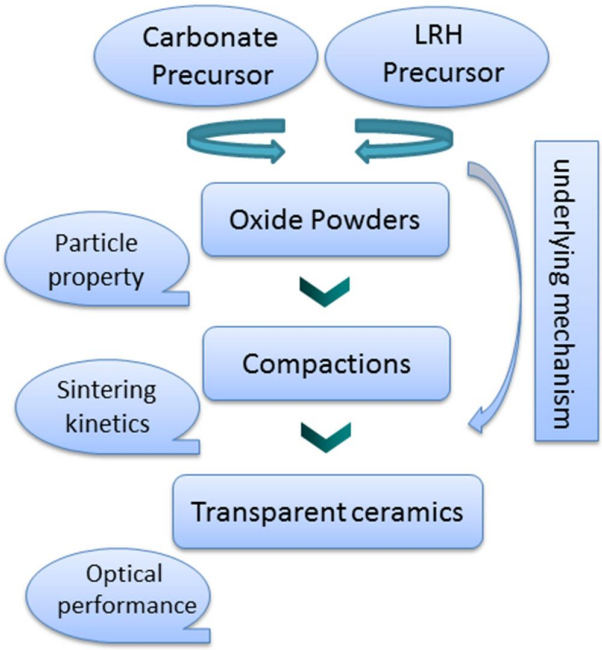

Fig. 1.11 Brief flow chart of processing technology.

As discussed in 1.4.2, vacuum sintering is a cost-effective technique but requires the sinterable powders, properties of which are, however, significantly affected by their precursors.

Therefore, the motivation for this thesis includes: (1) Synthesis and comparison of three type precursors (carbonate and nitrite- and sufate-contained LRHs) via advanced powder processing technique and proof positive of freezing-temperature technique for LRH synthesis is a good way for further yielding readily sinterable powders. (2) Fabrication of highly optical-quality transparent Y_2O_3-based ceramics via cost effective and time efficient vacuum sintering technique. The brief processing flow chart for ceramic processing is shown in Fig.1.11.

Based on this, furthermore, the following items and underlying mechanisms should be revealed and deciphered. (1) Systematical studies in powder synthesis for producing sinterable oxide powder shoud be carried out, including nucleation kinetics, photoluminescence behaviors and synthesis parameter effects (e.g. aging time, molar ratio of pricipitation/cation, $[Ln^{3+}]$ concentration, the amount of anion for ion exchange,

particle-calcination temperature and so forth); (2) Detailed comparation between nitrite- and sufate-contained LRHs for the final oxide powder and sintered bodies, such as particle mophology, particle size distribution, linear shrinkage, linear shrinkage rate, evolution of ceramic microstructure, relative density, dihedral angle and so forth; (3) In other to sinter highly transparent ceramics with fine grain size at relatively low temperature and short holding time, effects of sintering temperature and heating rate were invesigated; (4) Diffusion mechanism of YGO:Eu material as well as the role of Gd^{3+} substitution for Y^{3+} was revealed for understanding the sintering kinetics using the combined techniques of constant-rate-of-heating sintering and isothermal sintering; (5) The effective energy transfer from Tb^{3+} to Eu^{3+} was demonstrated to achieve color-tunable emission and enhanced emission intensity via co-doped Tb^{3+} and Eu^{3+} and varied Eu^{3+} concentration in Y_2O_3 ceramic host.

1.7 References

[1]T. Justel, H. Nikol, and C. Ronda, ñNew Developments in the Field of Luminescent Materials for Lighting and Displays,ò *Angew. Chem. Int. Ed.*, **37** [22] 3084-103 (1998).

[2]R. D. Shannon, ñRevised Effective Ionic Radii and Systematic Studies of Interatomic Distances in Halides and Chalcogenides,ò *Acta Crystallogr.*, **A32** 751-67 (1976).

[3]G. H. Dieke and H. M. Crosswhite, ñThe Spectra of the Doubly and Triply Ionized Rare Earths,ò *Appl. Optics*, **2** [7] 675-86 (1963).

[4]G. Wakefield, E. Holland, P. J. Dobson, and J. L. Hutchison, ñLuminescence Properties of Nanocrystalline Y_2O_3:Eu,ò *Adv. Mater.*, **13** [20] 1557-60 (2001).

[5]A. Paulraj, P. Natarajan, K. Munnisamy, M. K. Nagoor, K. P. Nattar, B. Abdulrazak, and J. Duraisamy, ñPhotoluminescence Efficiencies of Nanocrystalline versus Bulk Y_2O_3:Eu Phosphor-Revisited,ò *J. Am. Ceram. Soc.*, **94** [5] 1627-33 (2011).

[6]L. E. Shea, J. McKittrick, and O. A. Lopez, ñSynthesis of Red-Emitting, Small Particle Size Luminescent Oxides Using an Optimized Combustion Process,ò *J. Am. Ceram. Soc.*, **79** [12] 3257-65 (1996).

[7]S.-H. Byeon, M.-G. Ko, J.-C. Park, and D.-K. Kim, ñLow-Temperature Crystallization and Highly Enhanced Photoluminescence of $Gd_{2-x}Y_xO_3$:Eu^{3+} by Li Doping,ò *Chem. Mater.*, **14** [2] 603-8 (2002).

[8]E. Zych, M. Wawrzyniak, A. Kossek, J. Trojan-Piegza, and L. Kepinski, ñNew Synthesis Procedure for Nanoparticulate Lu_2O_3:Eu and Spectroscopy of the Product,ò *J. Alloy. Compd.*, **451** [1-2] 591-4 (2008).

[9]Y. Gao, J. Gong, M. Fan, Q. Fang, Q. Wang, N. Wang, W. Han, and Z. Xu, ñLarge-Scale Synthesis of Lu_2O_3:Ln^{3+} (Ln^{3+}=Eu^{3+}, Tb^{3+}, Yb^{3+}/Er^{3+}, Yb^{3+}/Tm^{3+}, and Yb^{3+}/Ho^{3+}) Microspheres and their Photoluminescence Properties,ò *Mater. Res. Bull*, **47** [12] 4137-45 (2012).

[10]H. Rétot, S. Blahuta, A. Bessière, B. Viana, B. LaCourse, and E. Mattmann, ñImproved Scintillation Time Response in $(Lu_{0.5}Gd_{0.5})_2O_3$:Eu^{3+} Compared with Lu_2O_3:Eu^{3+} Transparent Ceramics,ò *J. Phys. D: Appl. Phys.*, **44** [23] 235101 (2011).

[11]V. K. Klochkov, A. V. Grigorova, O. O. Sedyh, and Y. V. Malyukin, ñCharacteristics of $nLnVO_4$:Eu^{3+} (Ln = La, Gd, Y, Sm) Sols with Nanoparticles of Different Shapes and Sizes,ò *J. Appl. Spectrosc.*, **79** [5] 726-30 (2012).

[12]W. J. Park, M. K. Jung, S. J. Im, and D. H. Yoon, ñPhotoluminescence Characteristics of Energy Transfer between Bi^{3+} and Eu^{3+} in $LnVO_4$:Eu, Bi (Ln=Y, La, Gd),ò *Colloid Surf. A-Physicochem. Eng. Asp.*, **313-314** [1] 373-7 (2008).

[13]X. J. Wang, J.-G. Li, Q. Zhu, X. D. Li, X. D. Sun, and Y. Sakka, ñFacile and Green Synthesis of $(La_{0.95}Eu_{0.05})_2O_2S$ Red Phosphors with Sulfate-Ion Pillared Layered Hydroxides as a New Type of Precursor: Controlled Hydrothermal Processing, Phase Evolution and Photoluminescence,ò *Sci. Technol. Adv. Mater.*, **15** [1] 014204 (2014).

[14]Q. L. Dai, S. W. Song, M. Y. Wang, X. Bai, B. Dong, R. F. Qin, X. S. Qu, and H. Zhang, ñSize and Concentration Effects on the Photoluminescence of La_2O_2S:Eu^{3+} Nanocrystals,ò *J. Phys. Chem. C*, **112** [49] 19399-404 (2008).

[15]C.-C. Kang, R.-S. Liu, J.-C. Chang, and B.-J. Lee, ñSynthesis and Luminescent Properties of a New Yellowish-Orange Afterglow Phosphor Y_2O_2S:Ti,Mg,ò *Chem. Mater.*, **15** [21] 3966-8 (2003).

[16]R. Manigandan, K. Giribabu, R. Suresh, S. Munusamy, S. P. Kumar, S. Muthamizh, T. Dhanasekaran, A. Padmanaban, and V. Narayanan, ñSynthesis, Growth and Photoluminescence Behaviour of $Gd_2O_2SO_4$:Eu^{3+} Nanophosphors: the Effect of Temperature on the Structural, Morphological and Optical Properties,ò *RSC Adv.*, **5** [10] 7518-21 (2015).

[17]J. B. Lian, ñSynthesis, Structure and Properties of Rare Earth Ions Doped Gadolinium Oxysulfate and Oxysulfide Luminescent Materialsò; Ph.D. Thesis, Northeastern University, July 2009.

[18]T. Hirai, T. Hirano, and I. Komasawa, ñPreparation of Y_2O_3:Eu^{3+} Phosphor Fine Particles using an Emulsion Liquid Membrane System,ò *J. Mater. Chem.*, **10** [10] 2306-10 (2000).

[19]H. S. Yoo, H. S. Jang, W. B. Im, J. H. Kang, and D. Y. Jeon, ñParticle Size Control of a Monodisperse Spherical Y_2O_3:Eu^{3+} Phosphor and its Photoluminescence Properties,ò *J. Mater. Res.*, **22** [7] 2017-24 (2007).

[20]J.-G. Li, X. D. Li, X. D. Sun, and T. Ishigaki, ñMonodispersed Colloidal Spheres for Uniform Y_2O_3:Eu^{3+} Red-Phosphor Particles and Greatly Enhanced Luminescence by Simultaneous Gd^{3+} Doping,ò *J. Phys. Chem. C*, **112** [31] 11707-16 (2008).

[21]C. Adrian, S. Reto, and E. P. Sotiris, ñCubic or Monoclinic Y_2O_3:Eu^{3+} Nanoparticles by One Step Flame Spray Pyrolysis,ò *Chem. Phys. Lett.*, **415** [4-6] 193-7 (2005).

[22]J.-G. Li, Q. Zhu, X. D. Li, X. D. Sun, and Y. Sakka, ñColloidal Processing of Gd_2O_3:Eu^{3+} Red Phosphor Monospheres of Tunable Sizes: Solvent Effects on Precipitation Kinetics and Photoluminescence Properties of the Oxides,ò *Acta Mater.*, **59** [9] 3688-96 (2011).

[23]X. L. Wu, J.-G. Li, J. K. Li, Q. Zhu, X. D. Li, X. D. Sun, and Y. Sakka, ñLayered Rare-Earth Hydroxide and Oxide Nanoplates of the Y/Tb/Eu System: Phase-Controlled Processing, Structure Characterization and Color-Tunable Photoluminescence via Selective Excitation and Efficient Energy Transfer,ò *Sci. Technol. Adv. Mater.*, **14** [1] 015006 (2013).

[24]R. Stone, ñAn Investigation into Novel Red Emitting Phosphors and their Applicationsò; Ph.D. Thesis, Brunel University, September 2011.

[25]S. F. Ross, A. H. William, N. B. Kamala, and D. A. Mohan, ñEffects of Crystallite Grain Size on the Triboluminescent Emmision for EuD_4TEA,ò *Adv. Mat. Lett.*, **4** [8] 605-9 (2013).

[26]X. Yan, ñPhosphors for Lighting Applicationsò; Ph.D. Thesis, Brunel University, July 2012.

[27]G. H. Mhlongo, ñLuminescence Investigation of Trivalent Rare Earth Ions in Sol-Gel Derived SiO_2 and ZnO Co-Doped SiO_2:Pr^{3+}ò; Ph.D. Thesis, University of Free State, May 2011.

[28]J. A. Deluca, ñAn Introduction to Luminescence in Inorganic Solides,ò *J. Chem. Educ.*, **57** [8] 541-5 (1980).

[29]D. L. Dexter, and J. H. Schulman, ñTheory of Concentration Quenching in Inorganic Phosphors,ò *J. Chem. Phys.*, **22** [6] 1063-70 (1954).

[30]G. Blasse, ñEnergy Transfer between Inequivalent Eu^{2+} Ions,ò *J. Solid State Chem.*, **62** [2] 207-11 (1986).

[31]Y.-N. Xu, Z.-Q. Xu, and W. Y. Ching, ñElectronic, Structural, and Optical Properties of Crystalline Yttria,ò *Phys. Rev. B*, **56** [23] 14993-15000 (1997).

[32]Y. K. Saltoun, ñAn Investigation of the Synthesis and Properties of Nano Crystalline Y_2O_3:Eu^{3+}ò; Ph.D. Thesis, Brunel University, September 2011.

[33]P. Packiyaraj and P. Thangadurai, ñStructural and Photoluminescence Studies of Eu^{3+} Doped Cubic Y_2O_3 Nanophosphors,ò *J. Lumin.*, **145** 997-1003 (2014).

[34]E. E. Brown, U. Hoemmerich, A. Bluiett, C. Kucera, J. Ballato, and S. Trivedi, ñNear-Infrared and Upconversion Luminescence in Er:Y_2O_3 Ceramics under 1.5 μm Excitation,ò *J. Am. Ceram. Soc.*, **97** [7] 2105-10 (2014).

[35]S. Z. Lu, Q. H. Yang, H. J. Zhang, Y. G. Wang, D. D. Huang, Q. Wang, and Z. Y. Wei, ñSpectroscopic Characteristics and Laser Performance of Nd:$Y_{1.8}La_{0.2}O_3$ Transparent Ceramics,ò *IEEE J. Quantum Electron.*, **49** [3] 293-300 (2013).

[36]S. F. Wang, J. Zhang, D. W. Luo, F. Gu, D. Y. Tang, Z. L. Dong, G. E. B. Tan, W. X. Que, T. S. Zhang S. Li, and L. B. Kong, ñTransparent Ceramics: Processing, Materials and Applications,ò *Prog. Solid State Chem.*, **41** [1-2], 20-54 (2013).

[37]G. Blasse and B. C. Crabmaier, Luminescent Materials. Springer-Verlag Telos, 1994.

[38]C. D. Greskovich, D. Cusano, D. Hoffman, and R. J. Riedner, ñCeramic Scintillators for Advanced, Medical X-ray Detectors,ò *Am. Ceram. Soc. Bull.*, **71** [7] 1120-30 (1992).

[39]J. K. Li, J.-G. Li, Z. J. Zhang, X. L. Wu, S. H. Liu, X. D. Li, X. D. Sun, and Y. Sakka, ñGadolinium Aluminate Garnet ($Gd_3Al_5O_{12}$): Crystal Structure Stabilization via Lutetium Doping and Properties of the $(Gd_{1-x}Lu_x)_3Al_5O_{12}$ Solid Solutions (x = 0ï 0.5),ò *J. Am. Ceram. Soc.*, **95** [3] 931-6 (2012).

[40]C. Greskovich, and S. Duclos, ñCeramic Scintillators,ò *Annu. Rev. Mater. Sci.*, **27** 69-88 (1997).

[41]Y. Wang, B. Lu, X. D. Sun, T. Sun, and H. Xu, ñSynthesis of Nanocrystalline Sc_2O_3 Powder and Fabrication of Transparent Sc_2O_3 Ceramics,ò *Adv. Appl. Ceram.*, **110** [2] 95-8 (2011).

[42]Y. H. Huang, D. L. Jiang, J. X. Zhang, Q. L. Lin, and Z. R. Huang, ñSintering of Transparent Yttria Ceramics in Oxygen Atmosphere,ò *J. Am. Ceram. Soc.*, **93** [10] 2964-7 (2010).

[43]S. R. Podowitz, R. Gaume, and R. S. Feigelson, ñEffect of Europium Concentration on Densification of Transparent Eu:Y_2O_3 Scintillator Ceramics Using Hot Pressing,ò *J. Am. Ceram. Soc.*, **93** [1], 82-8 (2010).

[44]S. Z. Lu, Q. H. Yang, Y. G. Wang, Y. H. Li, and D. D. Huang, ñLuminescent Properties of Eu:$Y_{1.8}La_{0.2}O_3$ Transparent Ceramics for Potential White LED Applications,ò *Opt. Mater.*, **35** [4] 718-21 (2013).

[45]S. N. Bagayev, V. V. Osipov, V. A. Shitov, E. V. Pestryakov, V. S. Kijko, R. N. Maksimov, K. E. Lukyashin, A. N. Orlov, K. V. Polyakov, and V. V. Petrov, ñFabrication and Optical Properties of Y_2O_3-Based Ceramics with Broad Emission Bandwidth,ò *J. Eur. Ceram. Soc.*, **32** [16] 4257-62 (2012).

[46]H. B. Zhang, B.-N. Kim, K. Morita, H. Yoshida, K. Hiraga, Y. Sakka, and J. Ballato, ñFabrication of Transparent Yttria by High-Pressure Spark Plasma Sintering,ò *J. Am. Ceram. Soc.*, **94** [10] 3206-10 (2011).

[47]S. Grasso, C. Hu, G. Maizza, B. Kim, and Y. Sakka, ñEffects of Pressure Application Method on Transparency of Spark Plasma Sintered Alumina,ò *J. Am. Ceram. Soc.*, **94** [5] 1405-9 (2011).

[48]L. Esposito, A. Piancastelli, Y. Bykov, S. Egorov, and A. Eremeev, ñMicrowave Sintering of Yb:YAG Transparent laser Ceramics,ò *Opt Mater*, **35** [4], 761-5 (2013).

[49]S. V. Egorov, Y. V. Bykov, A. G. Eremeev, and A. A. Sorokin, ñLaser Ceramics Sintering by Millimeter-Wave Heating,ò *Radiophys. Quantum Electron.*, **56** [8-9] 574-81 (2014) .

[50]L. Ji and Y. Jiang, ñLaser Sintering of Transparent Ta_2O_5 Dielectric Ceramics,ò *Mater. Lett.*, **60** [12] 1502-4 (2006).

[51]Y. K. Kim, H. K. Kim, D. K. Kim, and G. S. Cho, ñSynthesis of Eu-Doped $(Gd,Y)_2O_3$ Transparent Optical Ceramic Scintillator,ò *J. Mater. Res.*, **19** [2] 413-6 (2004).

[52]Y. Q. Shen, Y. Shi, X. Q. Feng, Y. B. Pan, J. Li, Y. P. Zeng, M Nikl, A. Kranikov, A. Vedda, and F. Moretti, ñThe Harmful Effects of Sintering Aids in Pr:LuAG Optical Ceramic Scintillator,ò *J. Am. Ceram. Soc.*, **95** [7] 2130-2 (2012).

[53]X. D. Li, X. D. Sun, J.-G. Li, Z. M. Xiu, T. Gao, Y. N. Liu, and X. Z. Hu, ñCharacterization of High-Gadolinium $Y_{0.6}Gd_{1.34}Eu_{0.06}O_3$ Powder and Fabrication of Transparent Ceramic Scintillator Using Pressureless Sintering,ò *Int. J. Appl. Ceram. Technol.*, **7** [S1] E1-8 (2010).

[54]G. Cho, Y. K. Kim, S. H. Cho, D. K. Kim, B.-J. Kim, H. J. Seo, and H. K. Kim, ñSynthesis and Characterization of Doped Ceramic Scintillators Based on $(Gd,Y)_2O_3$,ò *IEEE Nucl. Sci. Symp. Conf. Rec.*, **3** 1314-7 (2005).

[55]Q. W. Chen, Y. Shi, L. Q. An, J. Y. Chen, and J. L. Shi, ñFabrication and Photoluminescence Characteristics of Eu^{3+}-Doped Lu_2O_3 Transparent Ceramics,ò *J. Am. Ceram. Soc.*, **89** [6] 2038-42 (2006).

[56]Z. M. Seeley, J. D. Kuntz, N. J. Cherepy, and S. A. Payne, ñTransparent Lu_2O_3:Eu Ceramics by Sinter and HIP Optimization,ò *Opt. Mater.*, **33** [11], 1721-6 (2013).

[57]Z. Seeley, N. Cherepy, and S. Payne, ñTwo-Step Sintering of $Gd_{0.3}Lu_{1.6}Eu_{0.1}O_3$ Transparent Ceramic Scintillator,ò *Opt. Mater. Express*, **3** [7], 908-12 (2013).

[58]Z. M. Seeley, N. J. Cherepy, and S. A. Payne, ñHomogeneity of Gd-Based Garnet Transparent Ceramic Scintillators for Gamma Spectroscopy,ò *J. Cryst. Growth*, **379** [15], 79-83 (2013).

[59]N. J. Cherepy, S. A. Payne, S. J. Asztalos, G. Hull, J. D. Kuntz, T. Niedermayr, S. Pimputkar, J. J. Roberts, R. D. Sanner, T. M. Tillotson, et al., ñScintillators with Potential to Supersede Lanthanum Bromide,ò *IEEE Trans. Nucl. Sci.*, **56** [3], 873-80 (2009).

[60]J. Xu, L. C. Fan, Y. Shi, J. L. Li, J. J. Xie, and F. Lei, ñScintillation and Luminescent Properties of Cerium Doped Lutetium Aluminum Garnet (Ce:LuAG) Powders and Transparent Ceramics,ò *IEEE Trans. Nucl. Sci.*, **61** [1], 373-9 (2014).

[61]S. P. Liu, X. Q. Feng, Y. Shi, L. X. Wu, J. L. Luo, W. Wang, and Y. B. Pan, ñFabrication, Microstructure and Properties of Highly Transparent Ce^{3+}:$Lu_3Al_5O_{12}$ Scintillator Ceramics,ò *Opt. Mater.*, **36** [12], 1973-7 (2014).

[62]Q. Wang and D. OõHare, ñRecent Advances in the Synthesis and Application of Layered Double Hydroxide (LDH) Nanosheets,ò *Chem. Rev.*, **112** [7] 4124-55 (2012).

[63]F. Gándara, J. Perles, N. Snejko, M. Iglesias, B. Gómez-Lor, E. Gutiérrez-Puebla, and M. Á. Monge, ñLayered Rare-Earth Hydroxides: A Class of Pillared Crystalline Compounds for Intercalation Chemistry,ò *Angew. Chem. Int. Ed.*, **45** [47] 7998-8001 (2006).

[64]L. J. McIntyre, L. K. Jackson, and A. M. Fogg, ñ$Ln_2(OH)_5NO_3{\cdot}xH_2O$ (Ln=Y, Gd-Lu): A Novel Family of Anion Exchange Intercalation Hosts,ò *Chem. Mater.*, **20** [1] 335-40 (2008).

[65]K.-H. Lee and S.-H. Byeon, ñExtended Members of the Layered Rare-Earth Hydroxides Family, $RE_2(OH)_5NO_3{\cdot}nH_2O$ (RE=Sm, Eu, and Gd): Synthesis and Anion-Exchange Behaviour,ò *Eur. J. Inorg. Chem.*, **2009** [7] 929-36 (2009).

[66]L. Poudret, T. J. Prior, L. J. McIntyre, and A. M. Fogg, ñSynthesis and Crystal Structures of New Lanthanide Hydroxyhalide Anion Exchange Materials, $Ln_2(OH)_5X{\cdot}1.5H_2O$ (X=Cl, Br; Ln=Y, Dy, Er, Yb),ò *Chem. Mater.*, **20** [24] 7447-53 (2008).

[67]K.-H. Lee and S.-H. Byeon, ñSynthesis and Aqueous Colloidal Solutions of $RE_2(OH)_5NO_3{\cdot}nH_2O$ (RE = Nd and La),ò *Eur. J. Inorg. Chem.*, **2009** [31] 4727-32 (2009).

[68]F. X. Geng, R. Z. Ma, and T. Sasaki, ñAnion-Exchangeable Layered Materials Based on Rare-Earth Phosphors: Unique Combination of Rare-Earth Host and Exchangeable Anions,ò *Acc. Chem. Res.*, **43** [9] 1177-85 (2010).

[69]S. Miyata, ñAnion-Exchange Properties of Hydrotalcite-Like Compounds,ò *Clays Clay Miner.*, **31** [4], 305-11 (1983).

[70]L. F. Hu, R. Z. Ma, T. C. Ozawa, and T. Sasaki, ñOriented Monolayer Film of Gd_2O_3:0.05Eu Crystallites: Quasi-Topotactic Transformation of the Hydroxide Film and Drastic Enhabcement of Photoluminescence Properties,ò *Angew. Chem. Int. Ed.*, **48** [21] 3846-9 (2009).

[71]Q. Zhu, J.-G. Li, C. Y. Zhi, R. Z. Ma, T. Sasaki, J. X. Xu, C. H. Liu, X. D. Li, X. D. Sun, and Y. Sakka, ñNanometer-Thin Layered Hydroxide Platelets of $(Y_{0.95}Eu_{0.05})_2(OH)_5NO_3{\cdot}xH_2O$: Exfoliation-Free Synthesis, Self-Assembly, and the Derivation of Dense Oriented Oxide Films of High Transparency and Greatly Enhanced Luminescence,ò *J. Mater. Chem.*, **21** [19] 6903-8 (2011).

[72]F. Gándara, E. G. Puebla, M. Iglesias, D. M. Proserpio, N. Snejko, and M. Á. Monge, ñControlling the Structure of Arenedisulfonates toward Catalytically Active Materials,ò *Chem. Mater.*, **21** [4] 655-61 (2009).

[73]P. Caravan, J. J. Ellison, T. J. McMurry, and R. B. Lauffer, ñGadolinium(III) Chelates as MRI Contrast Agents: Structure, Dynamics, and Applications,ò *Chem. Rev.*, **99** [9] 2293-352 (1999).

[74]S. Aime, M. Botta, M. Fasano, and E. Terreno, ñPrototropic and Water-Exchange Processes in Aqueous Solutions of Gd(III) Chelates,ò *Acc. Chem. Res.*, **32** [11] 941-9 (1999).

[75]B.-I. Lee, K. S. Lee, J. H. Lee, I. S. Lee, and S.-H. Byeon, ñSynthesis of Colloidal Aqueous Suspensions of a Layered Gadolinium Hydroxide: a Potential MRI Contrast Agent,ò *Dalton Trans.*, **14** 2490-5 (2009).

[76]Y.-S. Yoon, B.-I. Lee, K. S. Lee, S. H. Im, S.-H. Byeon, J. H. Lee, and I. S. Lee, ñSurface Modification of Exfoliated Layered Gadolinium Hydroxide for the Development of Multimodal Contrast Agents for MRI and Fluorescence Imaging,ò *Adv. Funct. Mater.*, **19** [21] 3375-80 (2009).

[77]F. X. Geng, Y. Matsushita, R. Z. Ma, H. Xin, M. Tanaka, F. Izumi, N. Iyi, and T. Sasaki, ñGeneral Synthesis and Structural Evolution of a Layered Family of $Ln_8(OH)_{20}Cl_4{\cdot}nH_2O$ (Ln=Nd, Sm, Eu, Gd, Tb, Dy, Ho, Er, Tm, and Y),ò *J. Am. Chem. Soc.*, **130** [48] 16344-50 (2008).

[78]F. X. Geng, Y. Matsushita, R. Z. Ma, H. Xin, M. Tanaka, N. Iyi, and T. Sasaki, ñSynthesis and Properties of Well-Crystallized Layered Rare-Earth Hydroxide Nitrates from Homogeneous Precipitation,ò *Inorg. Chem.*, **48** [14] 6724-30 (2009).

[79]X. L. Wu, J.-G. Li, Q. Zhu, J. K. Li, R. Z. Ma, T. Sasaki, X. D. Li, X. D. Sun, and Y. Sakka, ñThe Effects of Gd^{3+} Substitution on the Crystal Structure, Site symmetry, and Photoluminescence of Y/Eu Layered Rare-Earth Hydroxide (LRH) Nanoplates,ò *Dalton Trans.*, **41** [6] 1854-61 (2012).

[80]Q. Zhu, J.-G. Li, C. Y. Zhi, X. D. Li, X. D. Sun, Y. Sakka, D. Golberg, and Y. Bando, ñLayered Rare-Earth Hydroxides (LRHs) of $(Y_{1-x}Eu_x)_2(OH)_5NO_3{\cdot}nH_2O$ (x = 0-1): Structural Variations by Eu^{3+} Doping, Phase Conversion to Oxides, and the Correlation of Photoluminescence Behaviors,ò *Chem. Mater.*, **22** [14] 4204-13 (2010).

[81]Y. S. Zhao, J.-G. Li, M. X. Guo, and X. J. Yang, ñStructure and Photoluminescent Investigation of LTbH/LEuH Nanosheets and their Color-Tunable Colloidal Hybrids,ò *J. Mater. Chem. C*, **1** [22] 3584-92 (2013).

[82]X. L. Wu, ñNitrate-Type Layered Rare-Earth Hydroxides: Controlled Synthesis, Interlayer Ion Exchange, Sructure Characterization, and Applications in Photoluminescenceò; Ph.D. Thesis, Northeastern University, October 2013.

[83]X. L. Wu, J.-G. Li, Q. Zhu, W. G. Liu, J. Li, X. D. Li, X. D. Sun, and Y. Sakka, ñOne-Step Freezing Temperature Crystallization of Layered Rare-Earth Hydroxide ($Ln_2(OH)_5NO_3{\cdot}nH_2O$) Nanosheets for a Wide Spectrum of Ln (Ln=Pr-Er, and Y), Anion Exchange with Fluorine and Sulfate, and Microscopic Coordination Probed via Photoluminescence,ò *J. Mater. Chem. C*, **3** [14] 3428-37 (2015).

[84]J.-G. Li, T. Ikegami, T. Mori, and Y. Yajima ñSc_2O_3 Nanopowders via Hydroxyl Precipitation: Effects of Sulfate Ions on Powder Properties,ò *J. Am. Ceram. Soc.*, **87** [6] 1008ï 13 (2004).

[85]J.-G. Li, T. Ikegami, and T. Mori, ñFabrication of Transparent, Sintered Sc_2O_3 Ceramics,ò *J. Am. Ceram. Soc.*, **88** [4] 817ï 21 (2005).

[86]B. Lu, Y. Wang, X. D. Sun, and T. Sun, ñSynthesis of Sc_2O_3 Nanopowders and Fabrication of Transparent, Two-Step Sintered Sc_2O_3 Ceramics,ò *Adv. Appl. Ceram.*, **111** [7] 389-92 (2012).

Chapter Ⅱ

Ammonium hydrogen carbonate precipitation route for yielding red $(Gd,Ln)_2O_3$:Eu (Ln=Y, Lu) phosphors and transparent Y_2O_3:Eu ceramics

- **Effects of processing parameters on $(Gd_{0.75}Y_{0.2}Eu_{0.05})_2O_3$ particles**
- **Characterization of $(Gd_{0.95-x}Ln_xEu_{0.05})_2O_3$ compounds**
- **Fabrication of transparent $(Y_{0.95}Eu_{0.05})_2O_3$ ceramics**

2.1 Introduction

As described in Chapter Ⅰ, Eu^{3+} activated Gd_2O_3, Y_2O_3 and Lu_2O_3 as three kinds of well-known red phosphors are extensively applied in various lighting and display systems. The three phosphors display characteristic Eu^{3+} emissions at the wavelength of ~613 nm upon UV excitation into the charge transfer (CT) band (2*p* orbital of O^{2-} to the 4*f* orbital of Eu^{3+}).[1-8] Improved property of displays requires high-quality phosphors for high brightness and resolution with long-term stability. Phosphor particles of spherical morphology, ultrafine size, good dispersion and narrow size distribution are desired owing to three reasons: (1) spherical- shape powder can form a denser phosphor layer by close packing and minimizes the light scattering on particle surface to enhance the efficiency of photoluminescence (PL) and brightness;[9] (2) ultrafine powders provide small pixel sizes for improved resolution;[10-13] (3) well-dispersed and narrow size-distributed particles produce uniform luminescence over the whole phosphor screen.[14,15]

The $(Gd,Ln)_2O_3$:Eu (Ln=Y, Lu) solid solutions were selected to investigate herein based on the following three major reasons:

(1) Gd_2O_3:Eu phosphor may exhibit much stronger PL intensity and CT band than Y_2O_3:Eu and Lu_2O_3:Eu ones due to its lower electronegativity for Gd^{3+}. Generally, the PL intensity of Ln_2O_3:Eu phosphor can be significantly enhanced at elevated synthesis temperature. However, Gd_2O_3:Eu will undergo a transformation from a cubic to a monoclinic (or hexagonal) phase upon heating (>1250 °C), by which its PL intensity would be sharply lowered.

(2) The ionic radius of Y^{3+} (0.0900 nm) is close to that of Ho^{3+} (0.0901 nm),[16] resulting in similar chemical properties, and thus Y is generally regarded as a member of the lanthanide family. Y_2O_3 is cost effective, and hence its doping into Gd_2O_3:Eu red phosphor not only owns low-cost advantage but also achieves enhanced PL intensity. Additionally, Y^{3+} addition can effectively suppress the phase transformation of Gd_2O_3 through formation of a continuous solid-solution formation. $(Gd,Y)_2O_3$:Eu is a promising material to be utilized for fluorescent lamp, white LEDs, and can also be densified into transparent ceramic scintillator by advanced sintering technique.[17,18]

(3) Lu^{3+} has smaller ionic radius than Y^{3+}, and thus its doping may be more effective to stabilize the cubic structure of Gd_2O_3. In addition, Lu^{3+} possesses high absorption of x-rays to reduce the multiple scattering of light because of its high density and high effective atomic number. It has been demonstrated to be advantageous as the x-ray stopping material in ceramic scintillator.[19-21]

The commercial Eu^{3+} doped sesquioxide phosphors are conventionally produced by high-temperature solid-phase reaction and ball-milling treatment, which frequently induce large particle size, considerable agglomeration and undesired contamination. Therefore, wet chemical routes are necessary in the synthesis of fluorescent powders. Based on previous reports,[10-12,14,22-30] urea-based homogeneous precipitation (UBHP) technique is found to be a good tool to acquire uniform and monodispersed particles. Compared with the UBHP, ammonium hydrogen carbonate (AHC) precipitation is much more time-efficient, cost-effective, operation-simple and high-yield. In this chapter, $(Gd,Ln)_2O_3$:Eu (Ln=Y, Lu) red phosphor powders were studied for their synthesis, formation mechanism, compositional impacts and luminescence properties.

2.2 Experimental procedures

2.2.1 Powder synthesis and characterization

The starting materials were $Gd(NO_3)_3 \cdot 6H_2O$ (>99.95% pure, Kanto Chemical Co., Inc., Tokyo, Japan), $Y(NO_3)_3 \cdot 6H_2O$ (>99.99% pure, Kanto Chemical) and $Eu(NO_3)_3 \cdot 6H_2O$ (>99.95% pure, Kanto Chemical).

$Lu(NO_3)_3$ was prepared by dissolving a Lu_2O_3 powder (>99.95% pure, Kanto Chemical) in an excessive amount of nitric acid at ~90 °C.

In a typical synthetic procedure, precipitated precursors $(Gd_{0.95-x}Ln_xEu_{0.05})_2O_3$ (Ln=Y and Lu, x=0-0.95) were produced by dropwise addition of AHC (ultrahigh purity, Kanto Chemical) solution (1.5M) into a mixed mother liquor (0.15 M for total cationic concentration) at selected AHC/ total cation molar ratio (R) under magnetic stirring at room temperature. For typical synthesis, the x value was selected from 0 to 0.95 and the molar ratio of Eu^{3+} to total cations was fixed at 5 at%, optimal Eu^{3+} concentrations were reported to be 5 at% for Y_2O_3:Eu[12,31] and 5-7 at% for Gd_2O_3:Eu.[32-34] The resultant suspension, after aging for different times, was filtered and repeatedly washed with distilled water to remove byproduct. The precipitate cake was then rinsed by anhydrous alcohol to remove water, followed by drying at 80 °C. The dried precursors were lightly crushed with an alumina mortar and a pestle, and then calcined in a tube furnace under flowing oxygen gas (250 mL/min) at 1100 °C for 4 h with a heating rate of 5 °C /min in the ramp stage.

Compositions of the precursor was determined for cation contents were detected by the inductively coupled plasma (ICP) spectroscopic approach with an accuracy of 0.01 wt% (Model SPS3520, SII Nanotechnology Inc., Tokyo, Japan), for carbon on a carbon/sulfur determinator with a detection limit of 0.01 wt% (Model CS-444LS, LECO Co., Michigan, USA), and for NH_4^+ by the standard distillation-titrimetric method with an experimental error of ±0.1 wt%. The precursors and their oxides were characterized using thermogravimetry (TG; Model 6200, SII Nanotechnology Inc.), Brunauerï Emmettï Teller analysis (BET; Model Autosorb-iQ, Quantachrome Instruments, Florida, USA), x-ray diffractometry (XRD; Model RINT2200, Rigaku Corporation, Japan), field-emission scanning electron microscopy (FE-SEM; Model S-5000, Hitachi, Tokyo), laser diffraction particle size analysis (LDPSA, Model Horiba LA-920, Kyoto, Japan), and fluorescence spectroscopy (Model FP-6500, JASCO, Tokyo).

Cubic C-type sesquioxide lattice has eighty atoms per unit cell and its x-ray density can be calculated from equation 2.1.

$$d_{th} = \frac{32\times[(1-m-n)M_{Y/Lu}+mM_{Gd}+nM_{Eu}+1.5M_O]}{a^3 N_A} \qquad (2.1)$$

where M_i stands for atomic weight of element i (i = Y/ Lu, Gd, Eu and O), N_A is the Avogadro constant, a is the lattice constant, while m and n denote the atomic percentages of Gd^{3+} and Eu^{3+}, respectively.

2.2.2 Compaction, sintering, and characterization of transparent ceramics

The oxide powders for sintering were cold isostatically pressed under ~400 MPa into green bodies. Vacuum sintering was subsequently performed in a tungsten-heater furnace at 1700 temperatures for 4 h under a pressure of less than 10^{-3} Pa. The obtained ceramics were finally double-side polished to a thickness of ~1 mm to measure in-line transmittance on a UV/VIS/NIR spectrophotometer (Model SolidSpec-3700DUV, Shimadzu, Kyoto) over the wavelength region of 200-2000 nm.

2.3 Results and discussion

2.3.1 Effects of R on $(Gd_{0.75}Y_{0.2}Eu_{0.05})_2O_3$ precursors and their oxides

AHC/ total cation molar ratio (R) has significant effects on the nature of precipitated precursors, and the impact of R on the morphologies of the $(Gd_{0.75}Y_{0.2}Eu_{0.05})_2O_3$ precursors is shown in Fig. 2.1.

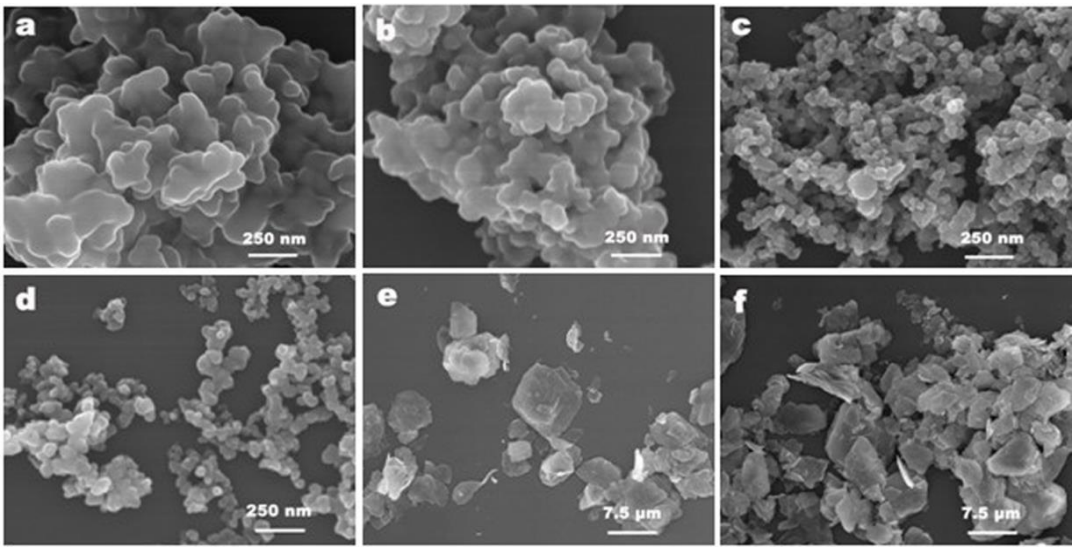

Fig. 2.1. FE-SEM micrographs showing morphologies of the $(Gd_{0.75}Y_{0.2}Eu_{0.05})_2O_3$ precursors obtained under typical synthetic conditions, with *R*=1 (a), *R*=2 (b), *R*=3 (c), *R*=4.5 (d), *R*=7.5 (e), and *R*=15 (f) and a fixed aging time of 1 h.

Figure 2.1 shows the effects of *R* on morphologies of the $(Gd_{0.75}Y_{0.2}Eu_{0.05})_2O_3$ precipitated with an aging time of 1 h. At *R*=1-4.5, the colloidal precursors appear spherical and are composed of ultrafine primary particles (Figs. 2.1a-d), while those acquired at *R*=7.5-15 display nonuniform mixtures and consist of very large and small platelike particles (Figs. 2.1e,f). Especially at low *R* (*R*=1-2), the precursor powders strongly agglomerate, which is probably because the low pH is close to their isoelectric points.

In water solution, Ln^{3+} ions are hydrated to $[Ln(H_2O)_6]^{3+}$ and then undergo hydrolysis to form $[Ln(OH)_x(H_2O)_{(6-x)}]^{3-x}$ species (Eqs. 2.2 and 2.3). However, the AHC solution contains lots of ionic species, such as HCO_3^-, CO_3^{2-}, OH^-, NH_4^+ and H^+. Compositions of the precursors formed from the reaction systems depend on the competition of the ionic species that combine with the Ln^{3+} (Eqs. 2.4-6).

$$Ln^{3+} + 6H_2O \rightarrow [Ln(H_2O)_6]^{3+} \qquad (2.2)$$

$$[Ln(H_2O)_6]^{3+} + xH_2O \rightarrow [Ln(OH)_x(H_2O)_{(6-x)}]^{3-x} + xH_3O^+ \qquad (2.3)$$

$$[Ln(OH)_x(H_2O)_{(6-x)}]^{3-x} + 3HCO_3^- + (x+n-7)H_2O \rightarrow Ln(OH)CO_3 \cdot nH_2O + 2CO_2 + xOH^- \qquad (2.4)$$

$$2Ln(OH)CO_3 \cdot nH_2O + HCO_3^- \rightarrow Ln_2(CO_3)_3 \cdot nH_2O + OH^- + H_2O \qquad (2.5)$$

$$Ln_2(CO_3)_3 \cdot nH_2O + CO_3^{2-} + 2NH_4^+ \rightarrow 2NH_4Ln(CO_3)_2 \cdot n\,H_2O \qquad (2.6)$$

Figure 2.2 exhibits XRD patterns of the $(Gd_{0.75}Y_{0.2}Eu_{0.05})_2O_3$ precursors obtained at *R*=1-15 and an aging time of 1 h. At *R*=1-4.5, the precursor powders are amorphous, corresponding to their rounded particle morphologies (Figs. 2.1a-d). As *R* increases above 7.5, the precursor powders significantly improve their crystallinities and show the characteristic two-dimensional shapes of layered rare-earth carbonates (Figs. 2.1e,f).[35]

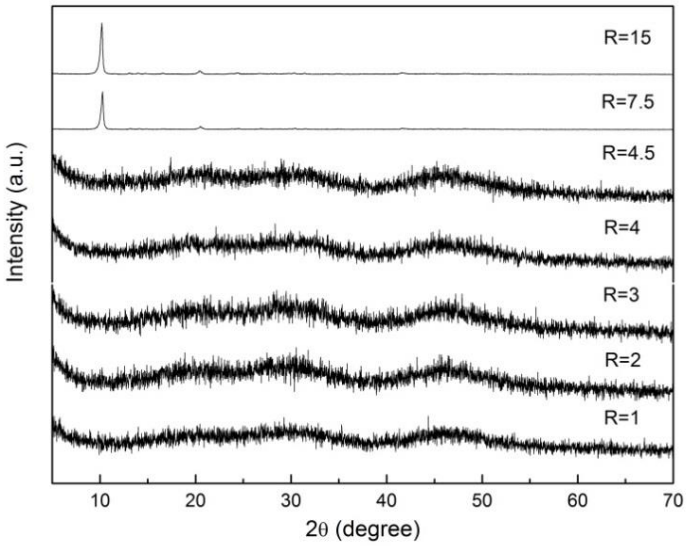

Fig. 2.2 XRD peaks of the $(Gd_{0.75}Y_{0.2}Eu_{0.05})_2O_3$ precursors obtained at *R*=1-15.

Table 2.1 Elemental content (wt%) of precursor powders prepared under typical synthesis conditions.

R	Aging (h)	Gd	Y	Eu	C	N	Approx. formula
1	1	47.2	4.9	3.4	6.4	-	$(Gd_{0.67}Y_{0.12}Eu_{0.05})_2(CO_3)_{2.52}\cdot 2.4H_2O$
4.5	1	44.8	6.7	2.8	7.3	-	$(Gd_{0.75}Y_{0.2}Eu_{0.05})_2(CO_3)_3\cdot 4H_2O$
4.5	10	45.8	7.2	2.9	7.3	0.92	$(NH_4)_{0.36}(Gd_{0.75}Y_{0.2}Eu_{0.05})_2(CO_3)_{3.18}\cdot 2.4H_2O$
7.5	1	37.8	5.6	2.4	7.4	3.1	$(NH_4)_{1.4}(Gd_{0.75}Y_{0.2}Eu_{0.05})_2(CO_3)_{3.7}\cdot 5.6H_2O$

Elemental analysis reveals that the precursors synthesized at *R*=1-4.5 have an approximate composition of hydrated carbonate, but low *R* (e.g. *R*=1) would cause a cationic component deviation owing to the incomplete precipitation (Table 2.1). At *RÓ*7.5, the platelike precursors are hydrated ammonium rare-earth carbonate that has layered structure with lanthanum and carbonate ions forming planes which are separated by planes of water molecules.[35]

Figure 2.3 shows the TG curves of two $(Gd_{0.75}Y_{0.2}Eu_{0.05})_2O_3$ precursors prepared at *R*=4.5 and *R*=7.5, which have been determined to possess a chemical composition of $(Gd_{0.75}Y_{0.2}Eu_{0.05})_2(CO_3)_3\cdot 4H_2O$ and $(NH_4)_{1.4}(Gd_{0.75}Y_{0.2}Eu_{0.05})_2(CO_3)_{3.7}\cdot 5.6H_2O$, respectively (Table 2.1).

The two precursors convert into oxide by four major steps. For the former, the initial decomposition (below 300 °C) is mainly due to dehydration and leads to a weight loss (-13.3%), which is consistent with theoretical value (-13.4%). And the weight losses of -29.8%, -33.7% and -37.8% for the other three steps also agrees with the calculated weight loss of -29.7%, -33.8% and -37.9%, respectively, which are mainly due to the removal of carbon dioxide.

The thermal decomposition processes of the latter is sililar to the former. The decomposition processes of the two precursors may be deduced as follows.

$$Ln_2(CO_3)_3 \cdot 4H_2O \xrightarrow[<300°C]{dehydration} Ln_2(CO_3)_3 \xrightarrow[300\text{-}600°C]{decarbonization}$$

$$\begin{cases} Ln_2O(CO_3)_2 \xrightarrow[600\text{-}680°C]{decarbonization} Ln_2O_2(CO_3) \xrightarrow[>680°C]{decarbonization} Ln_2O_3 \\ Ln_2O_3 \xrightarrow[>600°C]{crystallite\ growth} Ln_2O_3 \end{cases}$$

$$(NH_4)_{1.4}Ln_2(CO_3)_{3.7} \cdot 5.6H_2O \xrightarrow[<350°C]{dehydration\ and\ dea\,min\,ation} Ln_2(CO_3)_3 \xrightarrow[350\text{-}600°C]{decarbonization}$$

$$\begin{cases} Ln_2O(CO_3)_2 \xrightarrow[600\text{-}680°C]{decarbonization} Ln_2O_2(CO_3) \xrightarrow[>680°C]{decarbonization} Ln_2O_3 \\ Ln_2O_3 \xrightarrow[>600°C]{crystallite\ growth} Ln_2O_3 \end{cases}$$

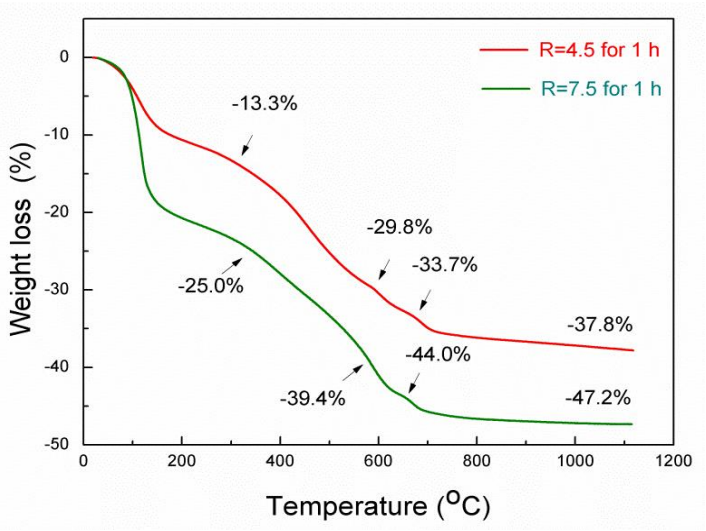

Fig. 2.3 TG traces for the $(Gd_{0.75}Y_{0.2}Eu_{0.05})_2O_3$ precursors prepared at *R*=4.5 and *R*=7.5, respectively.

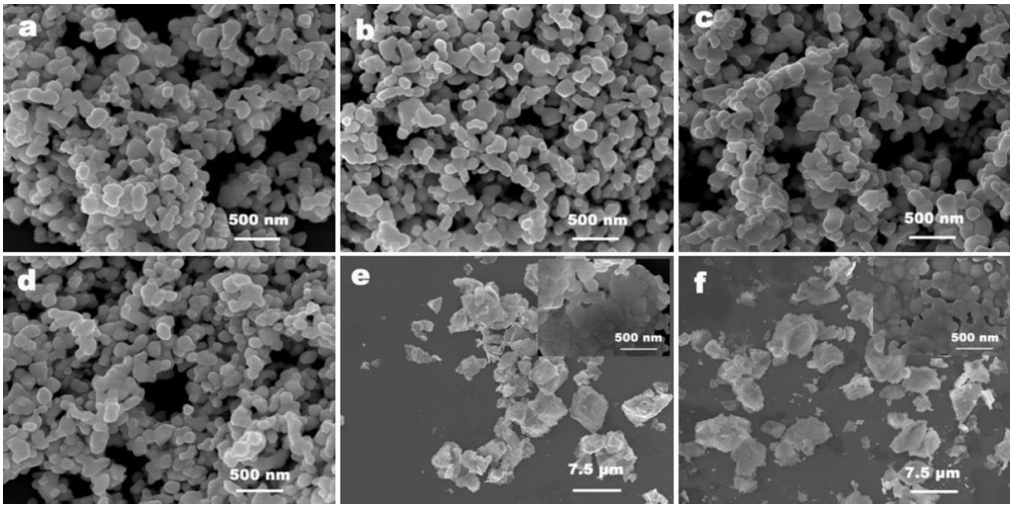

Fig. 2.4 FE-SEM micrographs of the $(Gd_{0.75}Y_{0.2}Eu_{0.05})_2O_3$ oxides calcined at 1100 °C for 4 h, obtained from the precursors of *R*=1 (a), *R*=2 (b), *R*=3 (c), *R*=4.5 (d), *R*=7.5 (e), and *R*=15 (f).

Figure 2.4 reveals that the calcined oxide powders generally retain the original morphologies of their respective precursors. The inside grains of the oxides calcined from the precursors of high *R* (e.g. *R*=7.5-15)

are apparently coarsening together and crystal boundaries appear (the insets in Figs. 2.4e,f), because the thick plates are difficult to collapse via single calcination. At *R*=4.5, the particles exhibit excellent morphology and the synthesis is mass production, and hence aging-time effect was subsequently studied under fixed *R*=4.5.

2.3.2 Aging-time impact on $(Gd_{0.75}Y_{0.2}Eu_{0.05})_2O_3$ precursors and their oxides

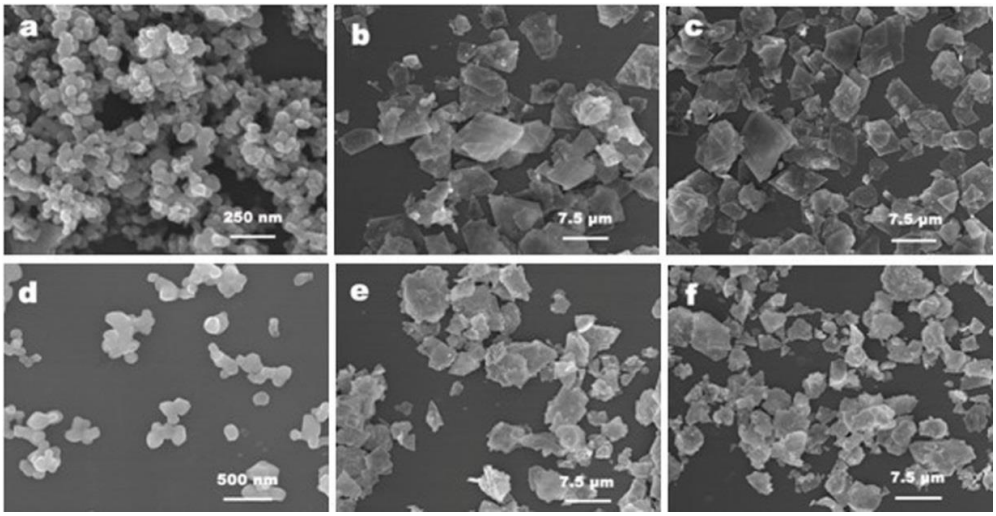

Fig. 2.5 FE-SEM micrographs showing morphologies of the $(Gd_{0.75}Y_{0.2}Eu_{0.05})_2O_3$ precursors and their oxides: the precursors synthesized at an aging time of 3 h (a), 6 h (b) and 10 h (c); and (d)-(f) for their oxides, respectively.

Figure 2.5 exhibits the impact of aging time on properties of the $(Gd_{0.75}Y_{0.2}Eu_{0.05})_2O_3$ precursors and their oxides at *R*=4.5. At an aging time of 3 h, the precursor is also spherical (Fig. 2.5a) and its calcination production is well dispersed (Fig. 2.5d). As the aging time increases to 6 h, both the precursor and its oxide transform into a platelike morphology (Figs. 5b, e). At the aging time over 10 h, the precursor also retains the layered structure, but may be composed of two phases (hydrated ammonium rare-earth carbonate and hydrated carbonate), as shown by the combined results of element analysis (Table 2.1) and the XRD analysis (Fig. 2.6).

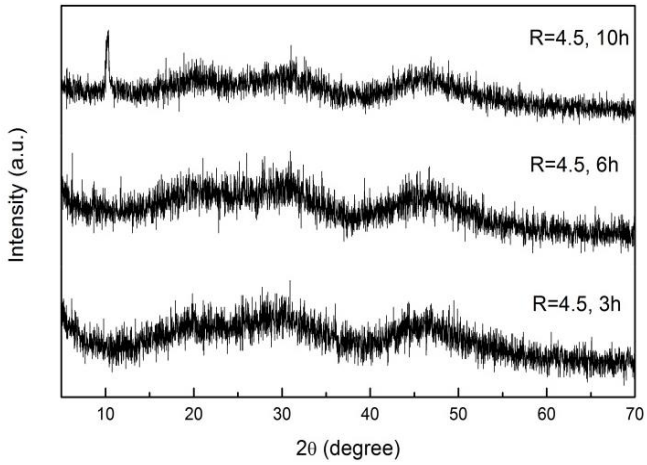

Fig 2.6 XRD patterns of the $(Gd_{0.75}Y_{0.2}Eu_{0.05})_2O_3$ precursors obtained at *R*=4.5 and an aging time of 3-10 h.

2.3.3 Synthesis and characterization of $(Gd,Ln)_2O_3$:Eu compounds

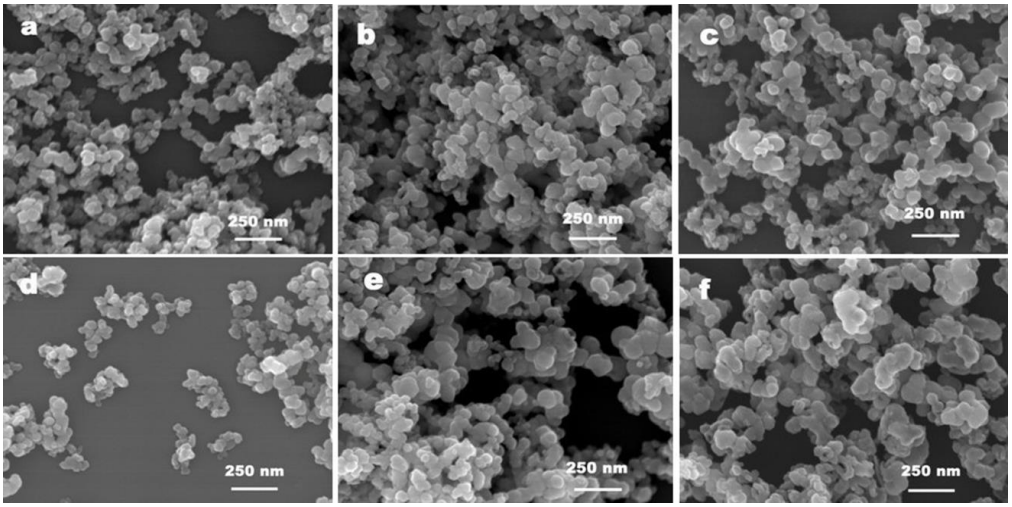

Fig. 2.7 FE-SEM micrographs of $(Gd_{0.95-x}Ln_xEu_{0.05})_2O_3$ precursor powders with Ln=Y, x=0 (a), x=0.6 (b), and x=0.95 (c); Ln=Lu, x=0.1 (d), x=0.6 (e), and x=0.95 (f).

A series of $(Gd_{0.95-x}Ln_xEu_{0.05})_2O_3$ (Ln=Y and Lu, x=0-0.95) powders were prepared under the optimized R (4.5) and aging time (3 h).

Figures 2.7a-c are FE-SEM micrographs showing morphologies of $(Gd_{0.95-x}Y_xEu_{0.05})_2O_3$ (x=0, 0.6, and 0.95) precursors. These precursors exhibit spherical shapes and the particle sizes increase with more Y^{3+} incorporation (~50, 68 and 78 nm for x=0, 0.6 and 0.95, respectively, as measured from the FE-SEM micrographs). The composition-dependent particle size is closely related with the nucleation and particle growth processes. That is, the occurrence of precipitation depends on supersaturation as the equation $S=a_Aa_B/K_{sp}$,[36] where a_A and a_B are the activities of partially hydrolyzed cation $[Ln(OH)_x(H_2O)_{6-x}]^{3-x}$ and anion (CO_3^{2-}), and K_{sp} is the solubility product constant. Nucleation starts only when S reaches the critical supersaturation S*. The solubility of a lanthanide basic carbonate increases with decreasing Ln^{3+} radius.[12] According to the lanthanide contraction law, the K_{sp} value increases in the order $Eu(OH)CO_3$ < $Gd(OH)CO_3$ < $Y(OH)CO_3$. Thus, $Eu(OH)CO_3$ and $Gd(OH)CO_3$ are formed in priority to play the role of crystal nuclei. As the Eu^{3+} cation and AHC concentration are fixed, more Gd^{3+} induces a higher nucleation density followed by smaller particle size. The deviating chemical composition of the precursor prepared at R=1 for 1 h also supports our interpretation (Table 2.1).

Figures 2.7d-f exhibit the morphologies of $(Gd_{0.95-x}Lu_xEu_{0.05})_2O_3$ (x=0.1, 0.6, 0.95) precursors. It can be observed that a higher Lu^{3+} content causes much larger particles of frequently empty interiors (~56, 78 and 101 nm for x=0.1, 0.6, and 0.95, respectively, as measured from the FE-SEM micrographs). It can be interpreted from the nucleation kinetics among $Lu(OH)CO_3$, $Eu(OH)CO_3$ and $Gd(OH)CO_3$. Although the K_{sp} increases in the order $Eu(OH)CO_3$ < $Gd(OH)CO_3$ < $Lu(OH)CO_3$, the relatively high degree of hydrolysis for Lu^{3+} may dominate here. As the higher hydrolysis degree of Lu^{3+} induces a higher activity of $[Lu(OH)_x(H_2O)_{6-x}]^{3-x}$, $Lu(OH)CO_3$ is thus produced in priority in the ternary Gd-Lu-Eu system. Meanwhile, high degree of hydrolysis also leads to a low pH value in the nitrate solution (Eq. 2.3). Therefore, when the AHC was added, lots of small bubbles would be generated via chemical decomposition of AHC (Eq. 2.7), which may provide crystal nuclei to form the hollow structures. Based on our previous reports,[37,38] such a phenomenon is also observed for Sc-containing compound with high degree of hydrolysis.

$$H^+ + HCO_3^- \rightarrow CO_2 + H_2O \qquad (2.7)$$

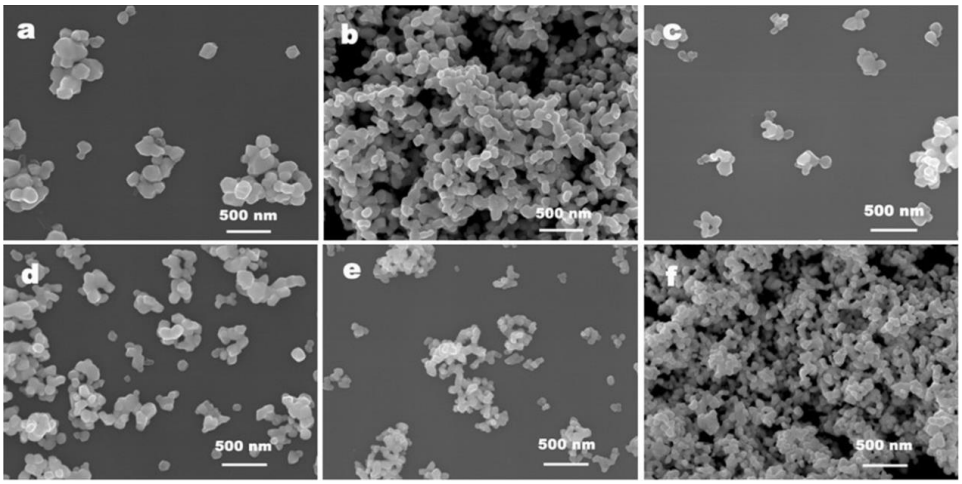

Fig. 2.8 FE-SEM micrographs of $(Gd_{0.95-x}Ln_xEu_{0.05})_2O_3$ oxide powders with Ln=Y, x=0 (a), x=0.6 (b), and x=0.95 (c); Ln=Lu, x=0.1 (d), x=0.6 (e), and x=0.95 (f).

Figure 2.8 shows morphologies of the $(Gd_{0.95-x}Y_xEu_{0.05})_2O_3$ (x=0, 0.6, 0.95) and $(Gd_{0.95-x}Lu_xEu_{0.05})_2O_3$ (x=0.1, 0.6, 0.95) oxide powders calcined at 1100 °C for 4 h. All the particles are ultrafine, uniform in size, well-dispersed and rounded in particle shape.

Table 2.2 $S_{BET,}$ crystallite size, SEM size and particle size of $(Gd,Y)_2O_3$:Eu oxides.

Y^{3+} content (%)	S_{BET} (m^2/g)	XRD (nm)	SEM (nm)	LDPSA (nm)
0	6.8	46.3	187	288
10	12.3	46.3	165	303
20	12.7	41.6	156	216
40	14.5	46.3	153	218
60	19.4	38.0	120	182
80	21.7	41.7	115	145
95	15.4	41.7	116	142

Table 2.3 $S_{BET,}$ crystallite size, SEM size and particle size of $(Gd,Lu)_2O_3$:Eu oxides.

Lu^{3+} content (%)	S_{BET} (m^2/g)	XRD (nm)	SEM (nm)	LDPSA (nm)
10	15.4	46.3	126	199
20	18.3	38.0	106	173
40	19.2	38.0	105	216
60	19.7	34.8	87	154
80	16.8	34.8	78	224
95	15.4	34.8	80	328

Tables 2.2 and 2.3 give out the S_{BET} value, the grain size calculated by XRD, the statistical FE-SEM particle size using WinRoof image analysis software and LDPSA size of $(Gd,Ln)_2O_3$:Eu oxides.

The grain sizes of the oxide powders generally decrease along with more Y^{3+}/Lu^{3+} addition. The lattice constants of $(Y_{0.95}Eu_{0.05})_2O_3$ (1.061 nm, Fig. 2.10) and $(Lu_{0.95}Eu_{0.05})_2O_3$ (1.040 nm) are smaller than that of $(Gd_{0.95}Eu_{0.05})_2O_3$ (1.080 nm). Mass diffusion in $(Y_{0.95}Eu_{0.05})_2O_3$ and $(Lu_{0.95}Eu_{0.05})_2O_3$ may be slower than that in $(Gd_{0.95}Eu_{0.05})_2O_3$ during thermal decomposition, leading to smaller grain sizes at a higher Y^{3+}/Lu^{3+} concentration. The SEM sizes of the oxides also generally decrease along with more Y^{3+}/Lu^{3+} addition. LDPSA is operative in detecting agglomerates.[39] Some relatively small particle sizes detected by LDPSA imply less agglomeration and higher dispersion of the powders.

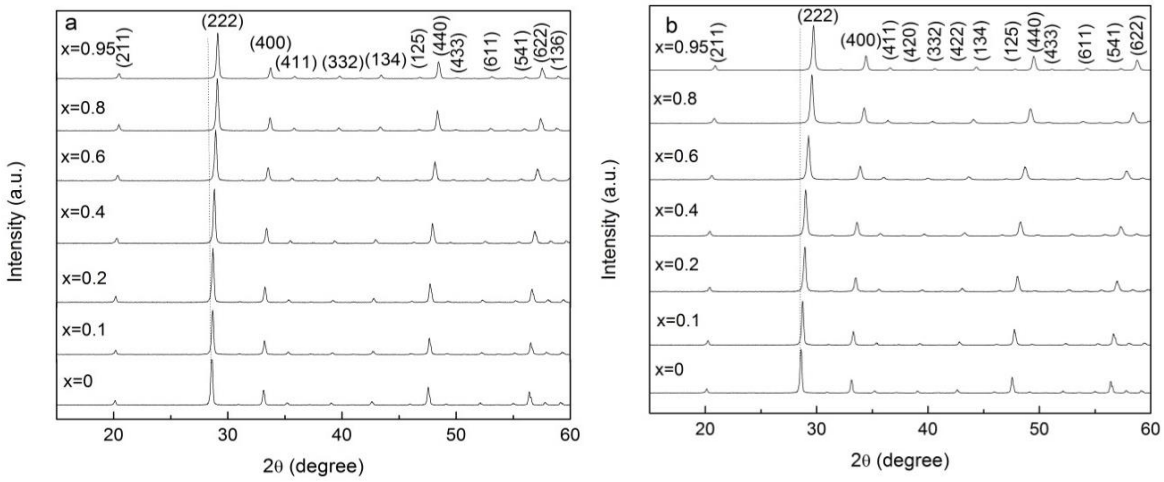

Fig. 2.9 XRD patterns of $(Gd,Ln)_2O_3$:Eu oxide powders with the composition $(Gd_{0.95-x}Y_xEu_{0.05})_2O_3$ (a) and $(Gd_{0.95-x}Lu_xEu_{0.05})_2O_3$ (b).

The XRD patterns of the $(Gd,Ln)_2O_3$:Eu oxide powders calcined at 1100 °C for 4 h are shown in Fig. 2.9. The XRD peaks of the two kinds of solid solutions shift toward the high angle side with increasing Y^{3+}/Lu^{3+} incorporation. Obviously, Y^{3+} and Lu^{3+} doping leads to a gradual contraction in the unit cell of the cubic crystal because of the smaller ionic radius of Y^{3+} and Lu^{3+} than that of Gd^{3+} and Eu^{3+}.

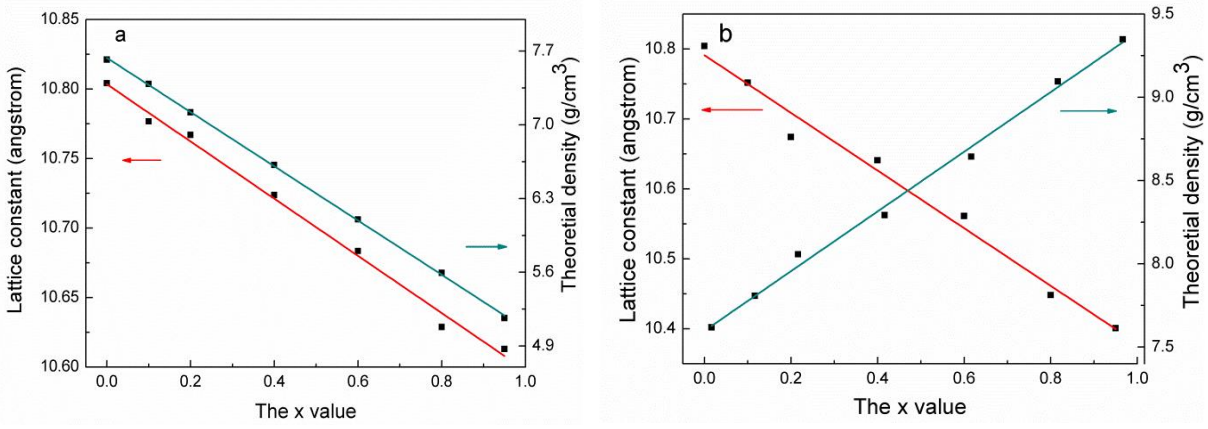

Fig. 2.10 lattice constants and theoretical densities of the $(Gd,Ln)_2O_3$:Eu solid solutions with the composition $(Gd_{0.95-x}Y_xEu_{0.05})_2O_3$ (c) and $(Gd_{0.95-x}Lu_xEu_{0.05})_2O_3$ (d).

Figure 2.10 shows the results of calculated lattice constants and theoretical densities of the $(Gd_{0.95-x}Ln_xEu_{0.05})_2O_3$ solid solutions. The cell parameters linearly decrease along with increasing *x*, which observes the Vegardôs law, suggesting that homogeneous solid solutions have been formed. The theoretical densities calculated with the lattice constants linearly decrease along with more Y^{3+} addition owing to its lower atomic number than Gd^{3+}, while the theoretical densities increase at a higher Lu^{3+} content since it is much heavier than Gd^{3+}.

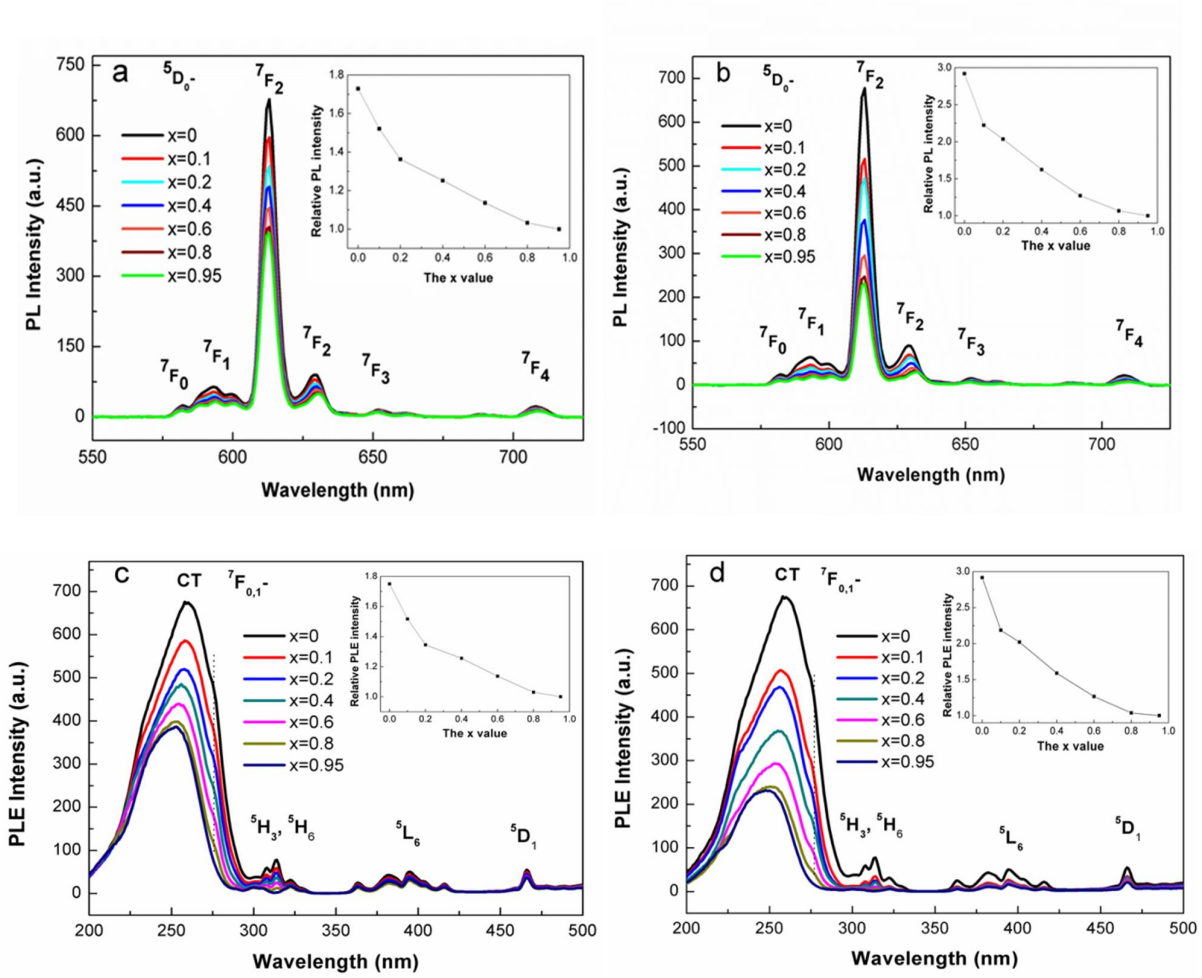

Fig. 2.11 Photoluminescence (PL) behaviors of the $(Gd_{0.95-x}Y_xEu_{0.05})_2O_3$ (a) and $(Gd_{0.95-x}Lu_xEu_{0.05})_2O_3$ phosphors (b). Photoluminescence excitation (PLE) spectra of the $(Gd,Ln)_2O_3$:Eu phosphors with the composition $(Gd_{0.95-x}Y_xEu_{0.05})_2O_3$ (a) and $(Gd_{0.95-x}Lu_xEu_{0.05})_2O_3$ (b). The PL spectra were obtained under excitations with the peak wavelengths of the CT bands and the PLE spectra were obtained by monitoring the 613 nm emissions of Eu^{3+}.

Figures 2.11a and b show PL spectra of $(Gd,Ln)_2O_3$:Eu phosphors. Both the $(Gd,Y)_2O_3$:Eu and $(Gd,Lu)_2O_3$:Eu oxide powders exhibit the typical red emissions of Eu^{3+} from $^5D_0$Ÿ ^7F_J (J=0, 1, 2, 3, 4) transitions. The strongest emission peak at 613 nm and that at 630 nm are assigned to the $^5D_0$Ÿ $^7F_2$ transitions of Eu^{3+}. The group of emission peaks at 587, 592 and 598 nm derives from $^5D_0$Ÿ $^7F_1$ of Eu^{3+}, while those at 582, 652 and 708 nm are associated with the $^5D_0$Ÿ $^7F_0$, $^5D_0$Ÿ $^7F_3$ and $^5D_0$Ÿ $^7F_4$ transitions, respectively.

The excitation spectra of $(Gd,Ln)_2O_3$:Eu powders obtained by monitoring the 613 nm Eu^{3+} emission are shown in Figs. 2.11c and d. The main bands at 248-258 nm are caused by the transition by charge transfer (CT), that is, electronic transition from the 2*p* orbital of O^{2-} to the 4*f* orbital of Eu^{3+}, the peaks at 217-

235 nm as the left shoulder of the broad CT bands are ascribed to the absorption of host lattice of rare earth oxide, and the right ones at 276 nm are owing to the $^8S_{7/2}$Ÿ ^6I_J internal *f-f* transition of Gd^{3+}.[6] The overlapped bands from 300 to 335 nm arise from the $^8S_{7/2}$Ÿ ^6P_J of Gd^{3+} and $^7F_{0,1}$Ÿ $^5H_3/^5H_6$ transitions of Eu^{3+}. The two types of bands can be distinguished by comparing with the non-Gd^{3+}-containing samples, whose peaks at 308 and 314 nm are only for the $^8S_{7/2}$Ÿ ^6P_J transition of Gd^{3+}. The other weak peaks beyond 350 nm are ascribed to the intra-$4f^6$ electronic transition of Eu^{3+}.

The PL and PLE intensities of $(Gd,Ln)_2O_3$:Eu particles mainly depend on the content of Gd^{3+}, since the different electronegativities among Gd^{3+}, Y^{3+} and Lu^{3+} result in diverse abilities to attract electrons and even shifted peak locations of CT bands[12,22] (6 nm for $(Gd,Y)_2O_3$:Eu and 10 nm for $(Gd,Lu)_2O_3$:Eu). The low electronegativity for Gd^{3+} (1.20) induces an easy electron transfer, and thus enhanced PL intensity is observed, although the larger particle size also contributes to the relatively strong emission. Additionally, for $(Gd,Y)_2O_3$:Eu and $(Gd,Lu)_2O_3$:Eu powders containing the same Gd^{3+} concentration, the PL/PLE intensities are in the order $(Gd,Lu)_2O_3$:Eu < $(Gd,Y)_2O_3$:Eu. Such a phenomenon is also due to the lower electronegativity of Y^{3+} (1.22) than that of Lu^{3+} (1.27). In this work, the PL intensity of $(Gd_{0.95}Eu_{0.05})_2O_3$ powder at 613 nm is about 1.7 times that of the $(Y_{0.95}Eu_{0.05})_2O_3$ one and 2.9 times that of $(Lu_{0.95}Eu_{0.05})_2O_3$, which are similar to the relative CT band intensity ratios.

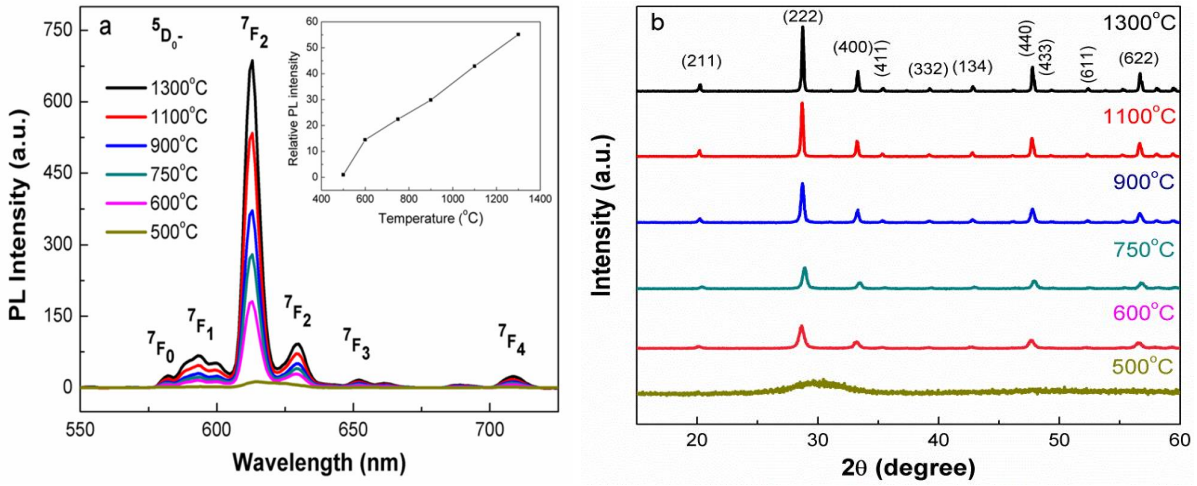

Fig. 2.12 The effects of calcination temperature on PL intensity of the $(Gd_{0.75}Y_{0.2}Eu_{0.05})_2O_3$ phosphors (a) and XRD patterns of the calcination products of the $(Gd_{0.75}Y_{0.2}Eu_{0.05})_2O_3$ sample (b).The PL spectra were obtained via excitation at 258 nm.

Calcination temperature also plays an important role in PL of the oxide phosphors and the results are shown in Fig. 2.12a with the $(Gd_{0.75}Y_{0.2}Eu_{0.05})_2O_3$ sample as an example. The PL intensity increases with rising calcination temperature, by which in that the component distributions among Gd^{3+}, Y^{3+} and Eu^{3+} are more homogeneous and would alleviate localized concentration quenching of Eu^{3+}. Improved crystallinity (Fig. 2.12b) and larger particle size are another two important reasons. The phosphor powder calcined at 500 °C shows low emission intensity probably owing to the combined effects of disordered coordination between Ln^{3+} and O^{2-} in the amorphous phase (Fig. 2.12b) and the presence of CO_3^{2-} in the intermediate calcination product (Fig. 2.3), which may raise the non-radiative relaxation rate. The PL intensity is greatly improved as the temperature increases to 600 °C, due to the phase transformation from an amorphous to cubic phase. As a result, a linear increase in PL intensity is observed at a higher calcinations temperature between 600 °C and 1300 °C (the inset in Fig. 2.12a).

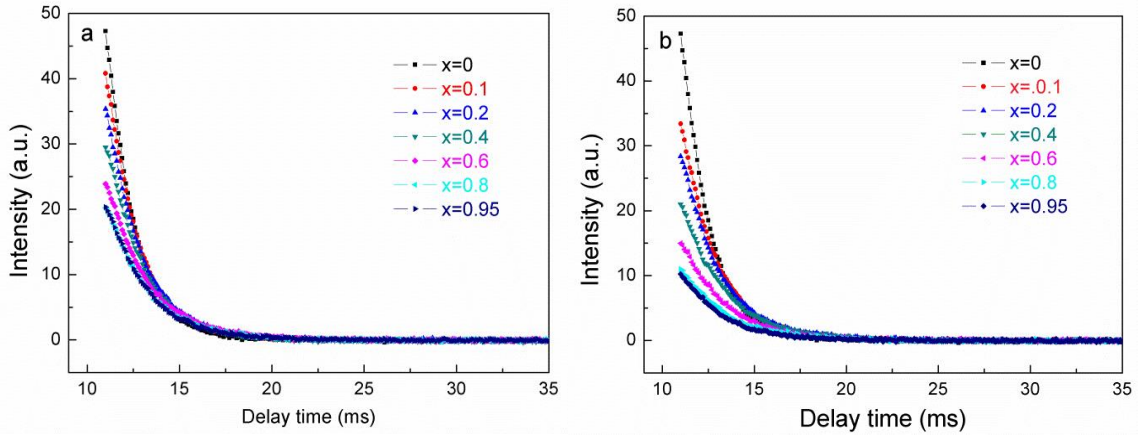

Fig 2.13 Fluorescence decay behaviors of the $(Gd,Ln)_2O_3$:Eu phosphors for the 613 nm emission with the composition $(Gd_{0.95-x}Y_xEu_{0.05})_2O_3$ (a), and $(Gd_{0.95-x}Lu_xEu_{0.05})_2O_3$ (b).

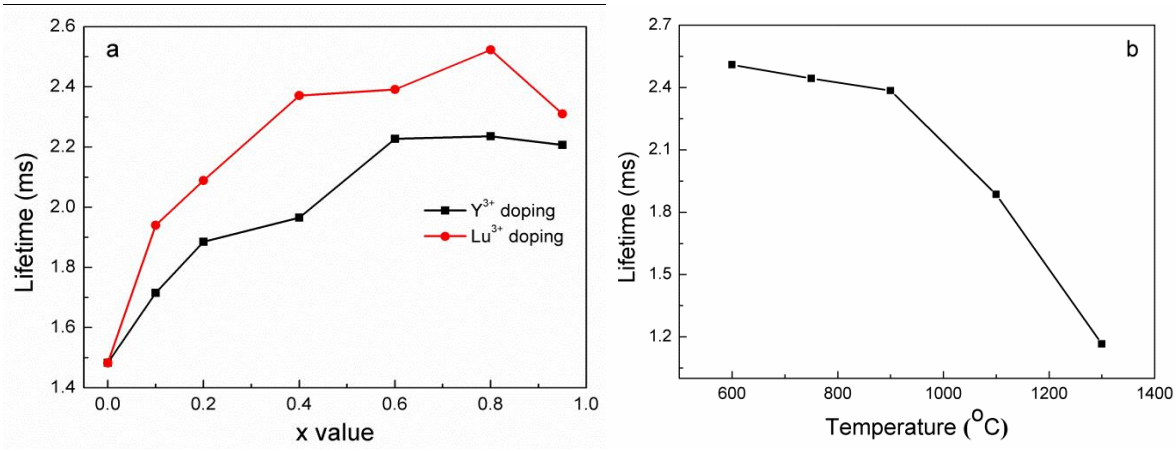

Fig. 2.14 Fluorescence lifetime of the $(Gd,Ln)_2O_3$:Eu phosphors (a) and calcination temperature effect on fluorescence lifetime by taking the $(Gd_{0.75}Y_{0.2}Eu_{0.05})_2O_3$ sample as an example (b).

The fluorescence lifetimes of the $(Gd,Ln)_2O_3$:Eu phosphors can be obtained by fitting the decay curves (Fig. 2.13) with a single exponential equation $I=Aexp(-t/\tau)+B$ (Fig. 2.14a), where t is the decay time, τ is the lifetime, t is the emission intensity, and A and B are constants.

The fluorescence lifetimes of Eu^{3+} doped Y_2O_3, Gd_2O_3 and Lu_2O_3 phosphors vary in the range 1.1-2.6 ms.[6,32,40-44] In this work, the fluorescence lifetimes are 1.48-2.23±0.01 ms for the $(Gd,Y)_2O_3$:Eu and 1.48-2.52±0.01 ms for the $(Gd,Lu)_2O_3$:Eu phosphors, which are close to each other and are in general agreement with the reported values. The lifetimes of $(Gd_{0.75}Y_{0.2}Eu_{0.05})_2O_3$ sample decrease at a higher calcination temperature, which can be attributable to the smaller specific surface area (larger particle size) and improved crystallinity (Fig. 2.14b).[45,46]

The external quantum efficiency (ε_{ex}, the total number of emitted photons divided by the total number of excitation photons) of the phosphor can be deduced from Eq. 2.8.

$$\varepsilon_{ex} = \frac{\int \lambda P(\lambda) d\lambda}{\int \lambda E(\lambda) d\lambda} \qquad (2.8)$$

where $P(\lambda)/hv$ and $E(\lambda)/hv$ are the number of photons in the emission and excitation spectra of the samples, respectively.

The external quantum efficiency is found in this work to be 63-100% for $(Gd,Y)_2O_3$:Eu and 46-100% for $(Gd,Lu)_2O_3$:Eu (Fig. 2.15a), and depends on the Gd^{3+} concentration, which may be attributed to the sensitization effect of Gd^{3+}.[33] The ε_{ex} dramatically increases with raising calcination temperature for the $(Gd_{0.75}Y_{0.2}Eu_{0.05})_2O_3$ sample (Fig. 2.15b). A 700 °C increase from 600 to 1300 °C improves the external quantum efficiency by ~83.3%, mainly owing to the crystal perfection. The external quantum efficiency was reported in the wide range of ~8-92% for Y_2O_3:Eu[47-49], 5-24% for Gd_2O_3:Eu[50,51] and 30-90% for Lu_2O_3:Eu phosphors.[44,52,53] Such significant deviation can be ascribed to varied particle sizes, particle morphologies and crystal defects, etc.

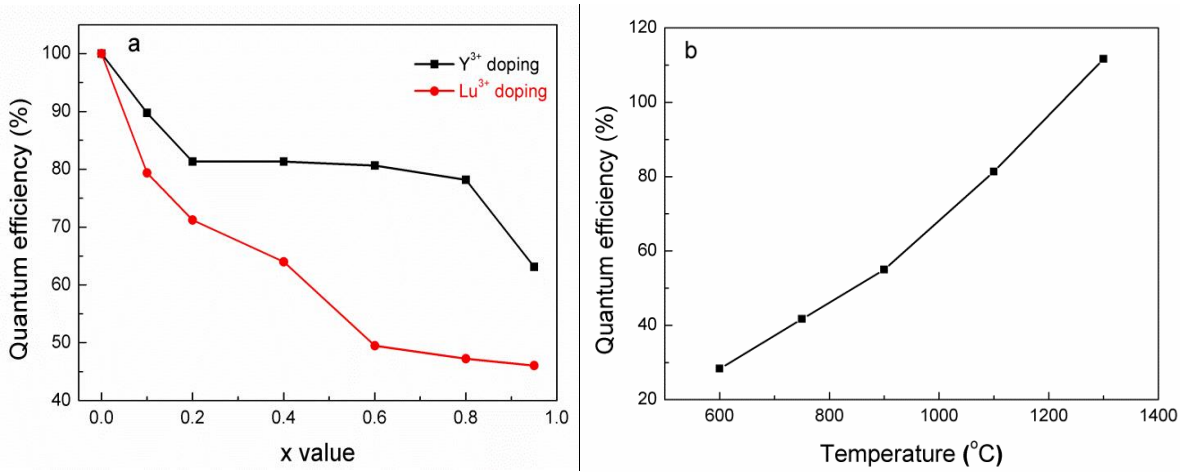

Fig. 2.15 External quantum efficiency of the $(Gd,Ln)_2O_3$:Eu phosphors and calcination temperature impact on quantum efficiency of the $(Gd_{0.75}Y_{0.2}Eu_{0.05})_2O_3$ phosphor.

2.3.4 Fabrication of Y_2O_3:Eu ceramics

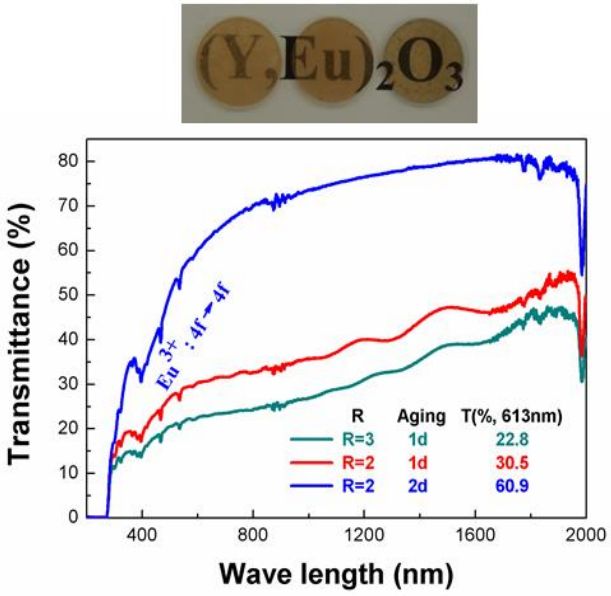

Fig. 2.14 Appearances and in-line transmittances of the vacuum sintered $(Y_{0.95}Eu_{0.05})_2O_3$ transparent ceramics. All the samples were vacuum sintered at 1700 °C for 4 h. The denotation keys in the lower part of the panel correspond to the three ceramics (from left to right) exhibited in the upper panel. The three samples all have a thickness of 1 mm.

After compaction and vacuum sintering, the resultant oxide powders made from the carbonate precursors at *R*=4.5 for 3 h have not been successfully densified into transparent ceramics. Therefore, further optimized particle processing for fabricating transparent $(Y_{0.95}Eu_{0.05})_2O_3$ ceramics has been studied.

Transparent $(Y_{0.95}Eu_{0.05})_2O_3$ ceramics can be fabricated via further optimized particle synthesis at a low *R* of 2-3 and a long aging time of 1-2 d (Fig. 2.14). Under identical sintering, these ceramics have in-line transmittances of 22.8%, 30.5% and 60.9% at the Eu^{3+} emission wavelength of 613 nm for *R*=3 with 1 d, *R*=2 with 1 d and *R*=2 with 2 d, respectively. Apparently, lower AHC content of *R*=2 and longer aging time of 2 d have yield a binary Y/Eu ceramic with a higher transparency. However, the results of elemental analysis (Table 2.4) reveals that cationic component deviation was induced at *R*Ò2, and hence AHC precipitation may be not a good way for fabricating transparent ceramics with multi-system and we report a new particle synthesis route for yielding highly transparent ceramics in the following chapters.

Table 2.4 Elemental content (wt%) of precursor powders prepared at *R*=2-3 with 1-2 d.

R	Aging (d)	Y	Eu	C	N	Approx. formula
3	1	40.0	3.7	8.21	-	$(Y_{0.95}Eu_{0.05})_2(CO_3)_3 \cdot 3.2H_2O$
2	2	39.2	5.1	8.42	-	$(Y_{0.66}Eu_{0.05})_2(CO_3)_{2.13} \cdot 2.2H_2O$

2.4 Conclusions

AHC precipitation has been demonstrated to be a good way for synthesis of phosphors, but not for fabrication of transparent ceramics with multi-system. The main conclusions are summarized as follows:

Well-dispersed $(Gd_{0.95-x}Ln_xEu_{0.05})_2O_3$ (Ln=Y and Lu, *x*=0-0.95) powders have been synthesized via AHC precipitation at *R*=4.5 and an aging time of 3 h. The nucleation kinetics between Gd-Y-Eu and Gd-Lu-Eu systems are different. For Gd-Y-Eu ternary system, the nucleation order is found to be $Y^{3+} < Gd^{3+} < Eu^{3+}$. In Gd-Lu-Eu system, however, the nucleation density increases in the order of cationic proportion $Gd^{3+} < Eu^{3+} < Lu^{3+}$. The grain sizes of the resultant oxides generally decrease along at a higher Y^{3+}/Lu^{3+} concentration. The lattice parameters of the two kinds of oxide solid solutions linearly shrink with more Y^{3+}/Lu^{3+} incorporation. The theoretical densities of the $(Gd,Ln)_2O_3$:Eu linearly decrease with increasing Y^{3+} addition, but increase at a higher Lu^{3+} content. The $(Gd,Ln)_2O_3$:Eu phosphor particles exhibit characteristic red emissions at 613 nm upon UV excitation into the CT band at 248-258 nm. The center of the CT bands red shifts increasing Y^{3+} or Lu^{3+} addition. The PL/ PLE intensities and ε_{ex} of $(Gd,Ln)_2O_3$:Eu phosphors improve with increasing *x*. Elevated calcination temperature enhances the PL intensity and the ε_{ex}, however, lowers the lifetimes of $(Gd,Ln)_2O_3$:Eu phosphors.

Transparent $(Y_{0.95}Eu_{0.05})_2O_3$ ceramics with the transmittances of 22.8-60.9% at the wavelength of 613 nm Eu^{3+} emission were fabricated by further optimized particle-synthesis parameter. However, low AHC content induced a cationic component deviation for Y/Eu binary system albeit achieved a higher transparency.

2.5 References

[1]C.-S. Park, M.-G. Kwak, S.-S. Choi, Y.-S. Song, S.-J. Hong, J.-I. Han, and D. Y. Lee, ñInfluence of Eu^{3+} Doping Content on Photoluminescence of $Gd_2O_3:Eu^{3+}$ Phosphors Prepared by Liquid-Phase Reaction Method,ò *J. Lumin.*, **118** [2] 199-204 (2006).

[2]D. K. Williams, H. Yuan, and B. M. Tissue, ñSize Dependence of the Luminescence Spectra and Dynamics of Eu^{3+} : Y_2O_3 Nanocrystals,ò *J. Lumin.*, **83-84** 297-300 (1999).

[3]J. W. Chung, H. K. Yang, B. K. Moon, B. C. Choi, and J. H. Jeong, ñLuminescence Properties of Eu^{3+}:RE_2O_3 [RE=Gd, Y, La] Nanocrystallines Prepared by Solvothermal Reaction Method,ò *J. Ceram. Process. Res.*, **13** s6-9 (2012).

[4]Y. Gao, J. Gong, M. Fan, Q. Fang, Q. Wang, N. Wang, W. Han, and Z. Xu, ñLarge-Scale Synthesis of $Lu_2O_3:Ln^{3+}$ (Ln^{3+} = Eu^{3+}, Tb^{3+}, Yb^{3+}/Er^{3+}, Yb^{3+}/Tm^{3+}, and Yb^{3+}/Ho^{3+}) Microspheres and their Photoluminescence Properties,ò *Mater. Res. Bull*, **47** [12] 4137-45 (2012).

[5]H. Rétot, S. Blahuta, A. Bessière, B. Viana, B. LaCourse, and E. Mattmann, ñImproved Scintillation Time Response in $(Lu_{0.5}Gd_{0.5})_2O_3$زEu^{3+} Compared with Lu_2O_3زEu^{3+} Transparent Ceramics,ò *J. Phys. D: Appl. Phys.*, **44** [23] 235101 (2011).

[6]Y. H. Li and G. Y. Hong, ñSynthesis and Luminescence Properties of Nanocrystalline $Gd_2O_3:Eu^{3+}$ by Combustion Process,ò *J. Lumin.*, **124** [2] 297-301 (2007).

[7]T. Igarashi, M. Ihara, T. Kusunoki, K. Ohno, and T. Isobe, ñRelationship between Optical Properties and Crystallinity of Nanometer Y_2O_3:Eu Phosphor,ò *Appl. Phys. Lett.*, **76** [12] 1549-51 (2000).

[8]J. L. Ferrari, M. A. Cebim, A. M. Pires, M. A. Couto dos Santos, and M. R. Davolos, ñ$Y_2O_3:Eu^{3+}$ (5 mol%) with Ag Nanoparticles Prepared by Citrate Precursor,ò *J. Solid State Chem.*, **183** [9] 2110-5 (2010).

[9]T. Hirai, T. Hirano, and I. Komasawa,ñPreparation of $Y_2O_3:Eu^{3+}$ Phosphor Fine Particles using an Emulsion Liquid Membrane System,ò *J. Mater. Chem.*, **10** [10] 2306-10 (2000).

[10]H. S. Yoo, H. S. Jang, W. B. Im, J. H. Kang, and D. Y. Jeon, ñParticle Size Control of a Monodisperse Spherical $Y_2O_3:Eu^{3+}$ Phosphor and its Photoluminescence Properties,ò *J. Mater. Res.*, **22** [7] 2017-24 (2007).

[11]M. K. Jung, W. J. Park, J. W. Moon, T. Masaki, A. Dulda, and D. H. Yoon, ñPhotoluminescence Characteristics of the Nano-Sized Red Phosphor $(Y_x,Gd_y)O_3:Eu_{1-x-y}^{3+}$ by Using Liquid Phase Precursor Methods,ò *J. Korean Phys. Soc.*, **53** [5] 2382-5 (2008).

[12]J.-G. Li, X. D. Li, X. D. Sun, and T. Ishigaki, ñMonodispersed Colloidal Spheres for Uniform $Y_2O_3:Eu^{3+}$ Red-Phosphor Particles and Greatly Enhanced Luminescence by Simultaneous Gd^{3+} Doping,ò *J. Phys. Chem. C*, **112** [31] 11707-16 (2008).

[13]C. Adrian, S. Reto, and E. P. Sotiris, ñCubic or Monoclinic $Y_2O_3:Eu^{3+}$ Nanoparticles by One Step Flame Spray Pyrolysis,ò *Chem. Phys. Lett.*, **415** [4-6] 193-7 (2005).

[14]J.-G. Li, Q. Zhu, X. D. Li, X. D. Sun, and Y. Sakka, ñColloidal Processing of $Gd_2O_3:Eu^{3+}$ Red Phosphor Monospheres of Tunable Sizes: Solvent Effects on Precipitation Kinetics and Photoluminescence Properties of the Oxides,ò *Acta Mater.*, **59** [9] 3688-96 (2011).

[15]X. L. Wu, J.-G. Li, J. K. Li, Q. Zhu, X. D. Li, X. D. Sun, and Y. Sakka, ñLayered Rare-Earth Hydroxide and Oxide Nanoplates of the Y/Tb/Eu System: Phase-Controlled Processing, Structure Characterization and Color-Tunable Photoluminescence via Selective Excitation and Efficient Energy Transfer,ò *Sci. Technol. Adv. Mater.*, **14** [1] 015006 (2013).

[16]R. D. Shannon, ñRevised Effective Ionic Radii and Systematic Studies of Interatomic Distances in Halides and Chalcogenides,ò *Acta Crystallogr.*, **A32** 751-67 (1976).

[17]Y. K. Kim, H. K. Kim, G. Cho, and D. K. Kim, ñEffect of Yttria Substitution on the Light Output of $(Gd,Y)_2O_3$:Eu Ceramic Scintillator,ò *Nucl. Instr. Meth. Phys. Res. B*, **225** [3] 392-6 (2004).

[18]R. M. Krsmanoví´, Ç. Anti´, B. Bártová, and M. G. Brik, ñFabrication of Polycrystalline $(Y_{0.7}Gd_{0.3})_2O_3:Eu^{3+}$ Ceramics: the Influence of Initial Pressure and Sintering Temperature on its Morphology and Photoluminescence Activity,ò *Ceram. Int.*, **38** [2] 1303-13 (2012).

[19]B. K. Cha, S.-M. Yong, S. J. Lee, D. K. Kim, J. H. Bae, G. Cho, C.-W. Seo, S. Jeon, and Y. Huh, ñSynthesis and Scintillation Characterization of Nanocrystalline Lu_2O_3(Eu) Powder for High-Resolution X-Ray Imaging Detectors,ò *J. Instrum.*, **7** C03048 (2012).

[20]J. K. Li, J.-G. Li, Z. J. Zhang, X. L. Wu, S. H. Liu, X. D. Li, X. D. Sun, and Y. Sakka, ñGadolinium Aluminate Garnet ($Gd_3Al_5O_{12}$): Crystal Structure Stabilization via Lutetium Doping and Properties of the $(Gd_{1-x}Lu_x)_3Al_5O_{12}$ Solid Solutions (x = 0ï 0.5),ò *J. Am. Ceram. Soc.*, **95** [3] 931-6 (2012).

[21]C. Greskovich and S. Duclos, ñCeramic Scintillators,ò *Annu. Rev. Mater. Sci.*, **27** 69-88 (1997).

[22]Q. Zhu, J.-G. Li, X. D. Li, and X. D. Sun, ñEffects of Y^{3+} Doping on Phase Structure and Photoluminescence Properties of $(Gd_{0.95-x}Y_xEu_{0.05})_2O_3$ Red Phosphors,ò *Mater. Technol.*, **27** [1] 116-8 (2012).

[23]J.-G. Li, X. D. Li, X. D. Sun, T. Ikegami, and T. Ishigaki, ñUniform Colloidal Spheres for $(Y_{1-x}Gd_x)_2O_3$ (x=0ï 1): Formation Mechanism, Compositional Impacts, and Physicochemical Properties of the Oxides,ò *Chem. Mater.*, **20** [6] 2274-81 (2008)

[24]Q. Zhu, J.-G. Li, X. D. Li, X. D. Sun, and Y. Sakka, ñMonodisperse Colloidal Spheres for $(Y,Eu)_2O_3$ Red-Emitting Phosphors: Establishment of Processing Window and Size-Dependent Luminescence Behaviour,ò *Sci. Technol. Adv. Mater.*, **12** [5] 055001 (2011).

[25]A. M. Pires, M. F. Santos, M. R. Davolos, and E. B. Stucchi, ñThe Effect of Eu^{3+} Ion Doping Concentration in Gd_2O_3 Fine Spherical Particles,ò *J. Alloy. Compd.*, **344** [1-2] 276-9 (2002).

[26]A. M. Pires, M. R. Davolos, and E. B. Stucchi, ñEu^{3+} as a Spectroscopic Probe in Phosphors Based on Spherical Fine Particle Gadolinium Compounds,ò *Int. J. Inorg. Mater.*, **3** [7] 785-90 (2001).

[27]B. Aiken, W. P. Hsu, and E. Matijevi´, ñPreparation and Properties of Monodispersed Colloidal Particles of Lanthanide Compounds: III, Yttrium(III) and Mixed Yttrium(III)/Cerium(III) Systems,*" J. Am. Ceram. Soc.*, **71** [10] 845-53 (1988).

[28]Y. Wang, B. Lu, X. D. Sun, T. Sun, and H. Xu, ñSynthesis of Nanocrystalline Sc_2O_3 Powder and Fabrication of Transparent Sc_2O_3 Ceramics,ò *Adv. Appl. Ceram.*, **110** [2] 95-8 (2011).

[29]B. Lu, Y. Wang, X. D. Sun, and T. Sun, ñSynthesis of Sc_2O_3 Nanopowders and Fabrication of Transparent, Two-Step Sintered Sc_2O_3 Ceramics,ò *Adv. Appl. Ceram.*, **111** [7] 389-92 (2012).

[30]T. Sugimoto, ñPreparation of Monodispersed Colloidal Particles,ò *Adv. Colloid Interface Sci.*, **28** 65-108 (1987).

[31]Y. Ganjkhanlou, M. Kazemzad, and F. A. Hessari, ñChromaticity Dependence on Eu Concentration in Y_2O_3:Eu Nanopowders,ò *Nano*, **5** [2] 111-6 (2010).

[32]S.-Y. Kim, S.-H. Cho, and J.-W. Shin, ñSynthesis and Characterization of Gd_2O_3:Eu Nano Phosphors for Application as X-ray Image Detectors,ò *J. Korean Phys. Soc.*, **50** [6] 1774-8 (2007)

[33]X. L. Wu, J.-G. Li, Q. Zhu, J. K. Li, R. Z. Ma, T. Sasaki, X. D. Li, X. D. Sun, and Y. Sakka, ñThe Effects of Gd^{3+} Substitution on the Crystal Structure, Site symmetry, and Photoluminescence of Y/Eu Layered Rare-Earth Hydroxide (LRH) Nanoplates,ò *Dalton Trans.*, **41** [6] 1854-61 (2012).

[34]L. F. Hu, R. Z. Ma, T. C. Ozawa, and T. Sasaki, ñOriented Monolayer Film of Gd_2O_3:0.05Eu Crystallites: Quasi-Topotactic Transformation of the Hydroxide Film and Drastic Enhabcement of Photoluminescence Properties,ò *Angew. Chem. Int. Ed.*, **48** [21] 3846-9 (2009).

[35]M. L. Panchula and M. Akinc, ñMorphology of Lanthanum Carbonate Particles Prepared by Homogeneous Precipitation,ò *J. Eur. Ceram. Soc.*, **16** [8] 833-41 (1996).

[36]B. L. Cushing, V. L. Kolesnichenko, and C. J. ч Connor, ñRecent Advances in the Liquid-Phase Synthese of Inorganic Nanoparticles,ò *Chem. Rev.*, **104** [9] 3893-946 (2004).

[37]J.-G. Li, T. Ikegami, and T. Mori, ñFabrication of Transparent, Sintered Sc_2O_3 Ceramics,ò *J. Am. Ceram. Soc.*, **88** [4] 817ï 21 (2005).

[38]B. Lu, X. D. Sun, T. Sun, and Y. Wang, ñSynthesis of Nanocrystalline Sc_2O_3 Powder Using a Microwave Homogenous Precipitation Approach,ò *Chin. J. Mater. Res.*, **25** [3] 255-8 (2011).

[39]X. D. Li, X. D. Sun, J.-G. Li, Z. M. Xiu, T. Gao, Y. N. Liu, and X. Z. Hu, ñCharacterization of High-Gadolinium $Y_{0.6}Gd_{1.34}Eu_{0.06}O_3$ Powder and Fabrication of Transparent Ceramic Scintillator Using Pressureless Sintering,ò *Int. J. Appl. Ceram. Technol.*, **7** [S1] E1-8 (2010).

[40]Q. Zhu, J.-G. Li, C. Y. Zhi, R. Z. Ma, T. Sasaki, J. X. Xu, C. H. Liu, X. D. Li, X. D. Sun, and Y. Sakka, ñNanometer-Thin Layered Hydroxide Platelets of $(Y_{0.95}Eu_{0.05})_2(OH)_5NO_3{\cdot}xH_2O$: Exfoliation-Free Synthesis, Self-Assembly, and the Derivation of Dense Oriented Oxide Films of High Transparency and Greatly Enhanced Luminescence,ò *J. Mater. Chem.*, **21** [19] 6903-8 (2011).

[41]Q. Zhu, J.-G. Li, X. D. Li, and X. D. Sun, ñMorphology-Dependent Crystallization and Luminescence Behaviour of $(Y,Eu)_2O_3$ Red Phosphors,ò *Acta Mater.*, **57** [20] 5975-85 (2009).

[42]G. Kaur, S. K. Singh, and S. B. Rai, ñEu^{3+} and Yb^{3+} Codoped Gd_2O_3 Single Phase Nanophosphor: An Enhanced Monochromatic Red Emission through Cooperative Upconversion and Downconversion,ò *J. Appl. Phys.*, **107** [7] 073514 (2010).

[43]G. X. Liu, G. Y. Hong, J. X. Wang, and X. T. Dong, ñHydrothermal synthesis of spherical and hollow Gd_2O_3:Eu^{3+} phosphors,ò *J. Alloy. Compd.*, **432** [1-2] 200-4 (2007).

[44]H. Y. Wei, Z. Cleary, S. Park, K. Senevirathne, and H. Eilers, ñFluorescence Lifetime Modification in Eu:Lu_2O_3 Nanoparticles in the Presence of Silver Nanoparticles,ò *J. Alloy. Compd.*, **500** [1] 96-101 (2010).

[45]H. P. Christensen, D. R. Gabbe, and H. P. Jenssen, ñFluorescence Lifetimes for Neodymium-Doped Yttrium Aluminum Garret and Yttrium Oxide Powders,ò *Phys. Rev. B*, **25** [3] 1467-73 (1982).

[46]J. K. Li, J.-G. Li, Z. J. Zhang, X. L. Wu, S. H. Liu, X. D. Li, X. D. Sun, and Y. Sakka, ñEffective Lattice Stabilization of Gadolinium Aluminate Garnet (GdAG) via Lu^{3+} Doping and Development of Highly Efficient (Gd,Lu)AG:Eu^{3+} Red Phosphors,ò *Sci. Technol. Adv. Mater.*, **13** [3] 035007 (2012).

[47]J. A. Nelson, E. L. Brant, and M. J. Wagner, ñNanocrystalline Y_2O_3:Eu Phosphors Prepared by Alkalide Reduction,ò *Chem. Mater.*, **15** [3] 688-93 (2003).

[48]Q. L. Dai, M. E. Foley, C. J. Breshike, A. Lita, and G. F. Strouse, ñLigand-Passivated Eu:Y_2O_3 Nanocrystals as a Phosphor for White Light Emitting Diodes,ò *J. Am. Chem. Soc.*, **133** [39] 15475-86 (2011).

[49]Ç. AntiÍ, R. Krsmanoviĺ, V. ĐorĽeviĺ, T. DramiĺanIn, and M. D. DramiĺanIn, ñOptical Properties of Y_2O_3:Eu^{3+} Red Emitting Phosphor Obtained via Spray Pyrolysis,ò *Acta Phys. Pol. A*, **116** [4] 622-4 (2009).

[50]C. Liu, J. Liu, and K. Dou, ñJuddī Ofelt Intensity Parameters and Spectral Properties of Gd_2O_3:Eu^{3+} Nanocrystals,ò *J. Phys. Chem. B*, **110** [41] 20277-81 (2006).

[51]C. X. Liu, J. H. Zhang, S. Z. Lu, and J. Y. Liu, ñJudd-Ofelt Parameters Determined Experimentally for Nanoparticles Gd_2O_3:Eu^{3+},ò *Acta Phys. Sin.*, **53** [11] 3945-9 (2004).

[52]A. N. Gruzintsev, G. A. Emelôchenko, Y. V. Yermolayeva, and V. M. Masalov, ñSpontaneous and Stimulated Red Luminescence of Lu_2O_3:Eu Nanocrystals,ò *Phys. Solid State*, **53** [6] 1263-8 (2011).

[53]E. Zych, A. Meijerink, and C. M. Donegá, ñQuantum Efficiency of Europium Emission from Nanocrystalline Powders of Lu_2O_3:Eu,ò *J. Phys.: Condens. Matter*, **15** [29] 5145-55 (2003).

Chapter Ⅲ

Synthesis of layered rare-earth hydroxide nanosheets leading to highly transparent Y_2O_3:Eu ceramics

- **Effects of SO_4^{2-} exchange on LRHs, oxides and ceramics**
  - **Significant reduction of hard agglomeration**
  - **Advantages of the freezing-temperature technique**
  - **Optimal particle processing and ceramic sintering**
- **Photoluminescence behaviors of the phosphors and ceramics**

3.1 Introduction

Eu^{3+} activated Y_2O_3 as a well-known red phosphor powder is extensively applied in areas such as fluorescent lamp, white LED, high-resolution x-ray imaging detector, field emission display, flat-panel display, plasma display panel and cathode-ray tube, and also in the fabrication of ceramic scintillator.[1-5] A scintillator may absorb and convert x-ray into visible photons to be applied in the medical systems of x-ray computed tomography and stationary digital imaging.[6,7] In order to achieve high-quality imaging, the scintillator should have some desired performances, that is, high transparency, high light output, short decay time, high absorption coefficient and low radiation damage.[8] Compared with single crystals, ceramic scintillators have the advantages of low cost, large size, high dopant concentration, mass production and near-neat shaping. Therefore, polycrystalline ceramic scintillator is being widely developed to replace the single crystal one.

Pressure-assisted sintering techniques are frequently utilized for producing transparent ceramics, such as hot pressing (HP) and hot isostatic pressing (HIP). Compared with HP and HIP, pressureless sintering techniques (vacuum and atmosphere-controlled sintering) are cost effective and time efficient but requires starting powder with good sinterability.[9-15] Other sintering methods have been developed to fabricate transparent ceramics and have their respective advantages,[16] including spark plasma sintering,[17,18] laser sintering,[19] microwave sintering[20] and millimetre-wave sintering,[21] but may find difficulties in fabricating thick bulk with high transparency in the visible region.

It is well known that hard aggregation is harmful for sintering and frequently creates serious defects in the sintered body, such as crack-like voids, large pores, white dots, etc., but great reduction of hard aggregation is still a challenge in powder synthesis. Ball-milling is a good tool for diminishing the volume of hard agglomerates, but tends to give rise to undesired contamination.

Wet chemical synthesis is often used for processing sinterable powders for ceramic production, and properties of the final powders mainly depend on their precursors.[9-12] As described in Chapter Ⅰ, layered rare-earth hydroxides (LRHs), with the general composition of $Ln_8(OH)_{20}(A^{m-})_{4/m}\cdot nH_2O$ or $Ln_2(OH)_5A\cdot nH_2O$, have attracted considerable attention[22-25] since its first finding in 2006.[26] The compounds consist of positively charged hydroxide layers of Ln^{3+} and exchangeable A^- anions located in the interlayer for charge balance, where A^- may include NO_3^- or halogen anion[24,25] and Ln^{3+} may be selected from a wide range of the lanthanide family (including Y).[27-29] Its crystal structure can be viewed as an alternative stacking along the *c*-axis of the hydroxide main layer and interlayer anions.[27] The synthesis routes for LRHs are reported to include hydrothermal synthesis,[22-24,26,30-32] solvothermal reaction[25] and homogenous precipitation,[27-29,33] by which thick plate-like crystallites with good crystallinity can be obtained. Thick plates, however, are difficult to collapse upon calcination and the resultant oxides generally retain the plate-like morphology.[34-36] The host layer of LRH is a close-packed low-energy plane and the thickness growth along the [001] direction needs much higher activation energy.[37,38] Lowering the synthesis temperature may thus be an effective method to suppress the LRH thickness growth.[37,38] In this work, we directly obtained ultrathin nanosheets (up to 7 nm thick) of the nitrate-type LRH for the Y/Eu binary system ($Ln_2(OH)_5NO_3\cdot nH_2O$, $Ln=Y_{0.95}Eu_{0.05}$) at freezing temperature of ~4 °C and attained anion exchange of the interlayer nitrate with sulfate anions. Calcining the sulfate derivative yielded well dispersed oxide powders that successfully densified into highly transparent $(Y_{0.95}Eu_{0.05})_2O_3$ ceramics via optimized vacuum sintering. In the following, the powder processing with LRH nanosheets as the precursor and fabrication of transparent ceramics were studied as well as optical properties of both the oxide powders and transparent bodies.

3.2 Experimental procedures

3.2.1 Powder synthesis and characterization

In our synthetic procedure, proper amounts of $Y(NO_3)_3 \cdot 6H_2O$ (>99.99% pure, Kanto Chemical Co., Inc., Tokyo, Japan) and $Eu(NO_3)_3 \cdot 6H_2O$ (>99.95% pure, Kanto Chemical) were dissolved in distilled water (~18 Mq) and well mixed under magnetic stirring, and the molar ratio of Eu^{3+} to total cations was fixed at 5 at%, since above which luminescence quenching would occur for Y_2O_3:Eu.[39,40] A $(Y_{0.95}Eu_{0.05})_2O_3$ precursor was produced at a freezing temperature of ~4 °C (also at room temperature for comparison) by the dropwise addition of ammonia solution (1 M, ultrahigh purity, Kanto Chemical) at ~3 mL/min into the prepared nitrate solution (0.01-0.20 M) under mild stirring till pH=8.7. After aging for 1.5 h, the resultant suspension was filtered and repeatedly washed with distilled water to remove byproduct. The precipitate cake was then dispersed in an ammonium sulfate solution under the selected synthesis temperature, and the SO_4^{2-} to total cation molar ratio (*R*) was selected from 0 to 2. After reaction for 2 h, the product was rinsed with distilled water and anhydrous alcohol, followed by drying at 80 °C. The dried precipitation precursor was lightly crushed with an alumina mortar and pestle, and then converted to an oxide powder by thermal decomposition in a tube furnace under flowing oxygen gas (300 mL/min) at 1000-1200 °C for 4 h with a heating rate of 5 °C/min in the ramp stage.

Composition of the precursor was determined for Y and Eu by the inductively coupled plasma (ICP) spectroscopic approach with an accuracy of 0.01 wt% (Model SPS3520, SII Nanotechnology Inc., Tokyo, Japan), for N on an oxygen/nitrogen analyser with a detection limit of 0.01 wt% (Model TC-436, LECO Co., St. Joseph, Michigan, USA), and for C/S on a carbon/sulfur determinator with a detection limit of 0.01 wt% (Model CS-444LS, LECO Co.). The precursors and their oxides were characterized using x-ray diffractometry (XRD; Model RINT2200, Rigaku), thermogravimetry (TG; Model 8120, Rigaku, Tokyo, Japan), Fourier transform infrared spectroscopy (FTIR; Model FT/IR-4200, JASCO, Tokyo), Brunauerï Emmettï Teller analysis (BET; Model Autosorb-iQ, Quantachrome Instruments, Boynton Beach, Florida, USA), laser diffraction particle size analysis (LDPSA; Model Horiba LA-920, Kyoto, Japan), transmission electron microscopy (TEM; Model JEM-2000FX, JEOL, Tokyo), field-emission scanning electron microscopy (FE-SEM; Model S-5000, Hitachi, Tokyo) and fluorescence spectroscopy (Model FP-6500, JASCO).

3.2.2 Compaction, sintering, and characterization of transparent ceramics

The oxide powders for sintering were cold isostatically pressed under a pressure of ~400 MPa. Densification kinetics was studied by dilatometry (Model 402 E/7, Netzsch, Germany) under flowing argon gas protection (250 mL/min) with constant heating and cooling rates of 10 and 20 °C/min, respectively.

Vacuum sintering was performed in a tungsten-heater furnace at various temperatures for 4 h under a pressure of less than 10^{-3} Pa. The densities of the sintered bodies were detected by the Archimedes method.

The sintered ceramics were polished on both sides to a thickness of ~1 mm to measure in-line transmittance on a UV/VIS/NIR spectrophotometer (Model SolidSpec-3700DUV, Shimadzu, Kyoto) over the wavelength region of 200-2000 nm.

The microstructures of the thermally etched specimens were observed by FE-SEM (Model JSM-6500F, JEOL). Average grain sizes of the ceramics were obtained from ~100 grains using WinRoof image analysis software.

Field-emission transmission electron microscopy (FE-TEM, Model JEM 2100F, JEOL) was applied for microstructure analysis of the sintered body, in both the FE-TEM and high angle annular dark field-scanning TEM (HAADF-STEM) modes, and for elemental mapping in the STEM mode. Samples were first polished to a thickness of ~100 εm, followed by Ar^+ thinning.

3.3 Results and discussion

3.3.1 Effects of SO_4^{2-} exchange on structure and thermal decomposition of LRHs

Table 3.1 Elemental contents (wt%) of the LRH precursor prepared at different *R*.

R	Y	Eu	N	C	S	Approx. formula
0	45.6	4.0	3.9	1.06	-	$(Y_{0.95}Eu_{0.05})_2(OH)_{4.4}(CO_3)_{0.3}NO_3\cdot 1.8H_2O$
0.05	45.7	4.1	2.7	1.53	0.77	$(Y_{0.95}Eu_{0.05})_2(OH)_{4.1}(CO_3)_{0.5}(NO_3)_{0.7}(SO_4)_{0.1}\cdot 1.9H_2O$
0.25	44.8	3.9	0.05	1.36	3.98	$(Y_{0.95}Eu_{0.05})_2(OH)_{4.19}(CO_3)_{0.4}(NO_3)_{0.01}(SO_4)_{0.5}\cdot 2.8H_2O$
0.5	44.9	3.9	0.06	1.09	4.07	$(Y_{0.95}Eu_{0.05})_2(OH)_{4.39}(CO_3)_{0.3}(NO_3)_{0.01}(SO_4)_{0.5}\cdot 2.8H_2O$
2	44.3	3.9	0.06	2.61	4.94	$(Y_{0.95}Eu_{0.05})_2(OH)_{3.19}(CO_3)_{0.8}(NO_3)_{0.01}(SO_4)_{0.6}\cdot 2.1H_2O$

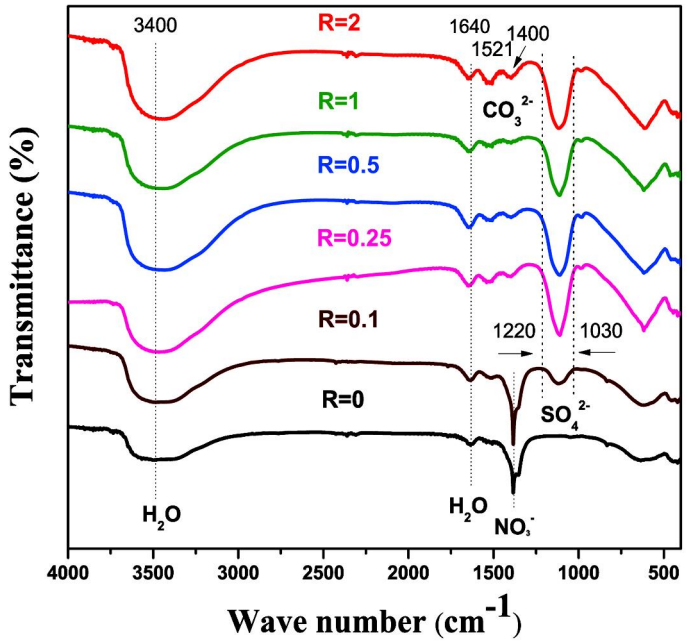

Fig. 3.1 FTIR spectra of the original LRH (*R*=0) and those exchanged by sulfate anions (*R*=0.1-2).

The sulfate/total cation molar ratio (*R*) has significant effects on the extent of ion exchange and the nature of the precipitated precursor. Elemental analysis (Table 3.1) reveals that the precursor obtained at *R*=0 has an approximate composition of $(Y_{0.95}Eu_{0.05})_2(OH)_{4.4}(CO_3)_{0.3}NO_3\cdot 1.8H_2O$, where the tiny amount of CO_3^{2-} may be derived from atmospheric CO_2. At *R*=0.25, almost a complete anion exchange is achievable to form the sulfate derivative of $(Y_{0.95}Eu_{0.05})_2(OH)_{4.19}(CO_3)_{0.4}(NO_3)_{0.01}(SO_4)_{0.5}\cdot 2.8H_2O$, as expected from the chemical formula, namely one SO_4^{2-} would replace two NO_3^- for charge balance. The trace nitrate may be caused by surface adsorption of nitrate anion in the solution or atmospheric nitrogen.

Figure 3.1 shows the FTIR spectra of the original LRH (R=0) and those exchanged by sulfate anions (R=0.1-2). The absorption band at ~1640 cm^{-1} is the characteristic bending mode (ν2) of molecular water. The broad band at ~3400 cm^{-1} is arising from molecular water (symmetric ν1 and antisymmetric ν3, ~3200-3500 cm^{-1}) and free hydroxyl groups (~3000-3700 cm^{-1}). The presence of absorption doublets in the region of ~1350-1600 cm^{-1} is diagnostic of carbonate anion (ν3, ~1400 and 1521 cm^{-1}). The absorption band at ~1378 cm^{-1} is the vibration of nitrate anion and that in the ~1030-1220 cm^{-1} range is characteristic of sulfate anion. The result of FTIR is consistent with that of elemental analysis (Table 3.1).

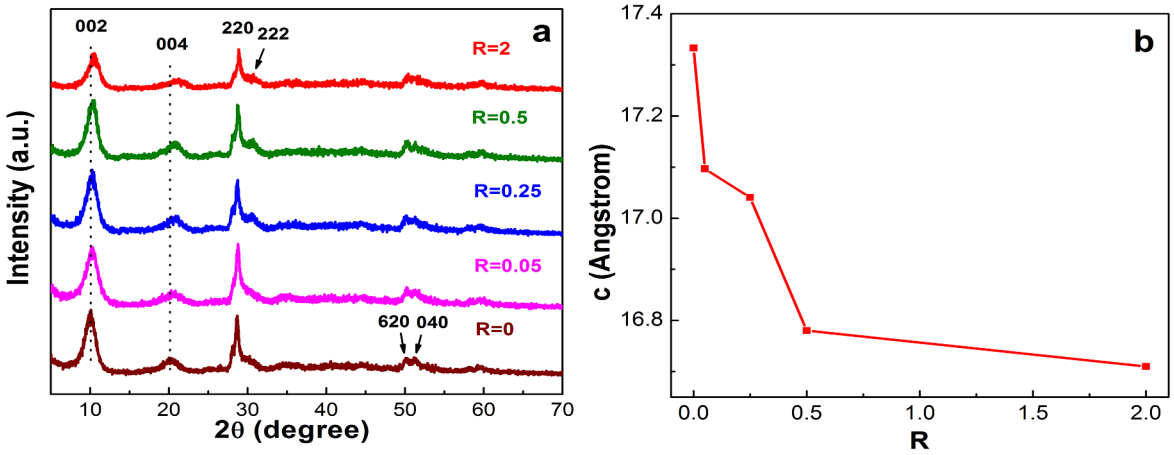

Fig. 3.2 XRD patterns (a) and *c*-constants (b) of the original (R=0) and sulfate-exchanged (R=0.05-2) LRHs.

Figure 3.2a exhibits XRD patterns of the original LRH and the sulfate-exchanged productions (R=0-2). A series of 00*l* and sharp 220 diffractions were observed to be characteristic of the LRH compounds,[29] and the 002 and 004 reflections clearly shift towards the high angle side with increasing R, implying contracted dimension of the unit cell in the *c*-direction. The interlayer distance (c/2) shrank from ~0.867 to 0.835 nm with increasing sulfate substitution from R=0 to 2 (Fig. 3.2b), since the sulfate radicals not only exchange the nitrate anions in the interlayer of LRH but also form hydrogen bonding with the water molecules and hydroxyls in the hydroxide main layers,[37,38] causing the gradually contracted interlayer distance.

TG analysis (Fig. 3.3) reveals that the nitrate- and sulfate-type LRHs decompose into oxides via two different procedures as follows:

$$Ln_2(OH)_{4.4}(CO_3)_{0.3}NO_3\cdot 1.8H_2O \xrightarrow[<150^\circ C]{dehydration} Ln_2(OH)_{4.4}(CO_3)_{0.3}NO_3$$

$$\xrightarrow[150\text{-}310^\circ C]{dehydroxylization} Ln_2O_2(OH)_{0.4}(CO_3)_{0.3}NO_3 \xrightarrow[decarbonation,\,310\text{-}570^\circ C]{denitration,dehydroxylization} Ln_2O_3$$

$$Ln_2(OH)_{4.19}(CO_3)_{0.4}(NO_3)_{0.01}(SO_4)_{0.5}\cdot 2.8H_2O \xrightarrow[<170^\circ C]{dehydration} Ln_2(OH)_{4.19}(CO_3)_{0.4}(NO_3)_{0.01}(SO_4)_{0.5}$$

$$\xrightarrow[170\text{-}300^\circ C]{dehydroxylization} Ln_2O(OH)_{2.19}(CO_3)_{0.4}(NO_3)_{0.01}(SO_4)_{0.5}$$

$$\xrightarrow[decarbonation,\,300\text{-}970^\circ C]{dehydroxylization,denitration} \begin{cases} Ln_2O_2SO_4 \xrightarrow[970\text{-}1100^\circ C]{desulfuration} Ln_2O_3 \\ Ln_2O_3 \xrightarrow[>970^\circ C]{particle\ growth} Ln_2O_3 \end{cases}$$

That is, the nitrate-type LRH converts to oxide up to ~600 °C by three major steps while the sulfate-type (R=0.25) up to a much higher temperature of ~1100 °C by four steps, with an additional desulfuration

stage for $Ln_2O_2SO_4$ decomposition.[30,37] For the sulfate-type LRH, the weight losses of ~11.1, 18.5, and 27.6 and -37.8% for 1-4 steps are close to the values of 13.3, 18.1, 28.1 and 38.7% calculated from the chemical reactions, respectively. The XRD analysis for phase evolution (Fig. 3.4) further supports our interpretation of the TG results. Furthermore, dehydration and dehydroxylization of the sulfate-type LRH substantially lag behind those of the nitrate-type, which can be attributed to the effects of hydrogen bonding between SO_4^{2-} and water molecules/OH^- groups.

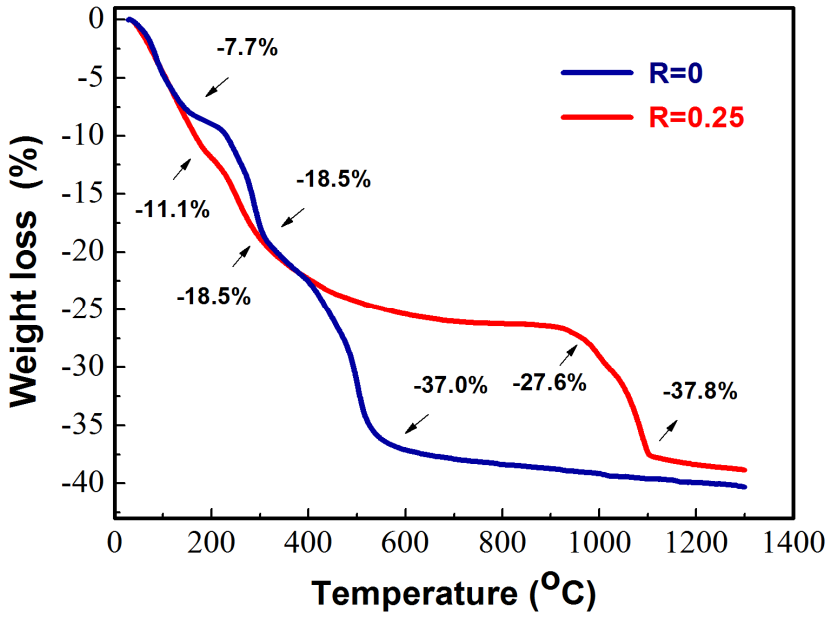

Fig. 3.3 TG traces for the two kinds of LRHs prepared at *R*=0 and *R*=0.25.

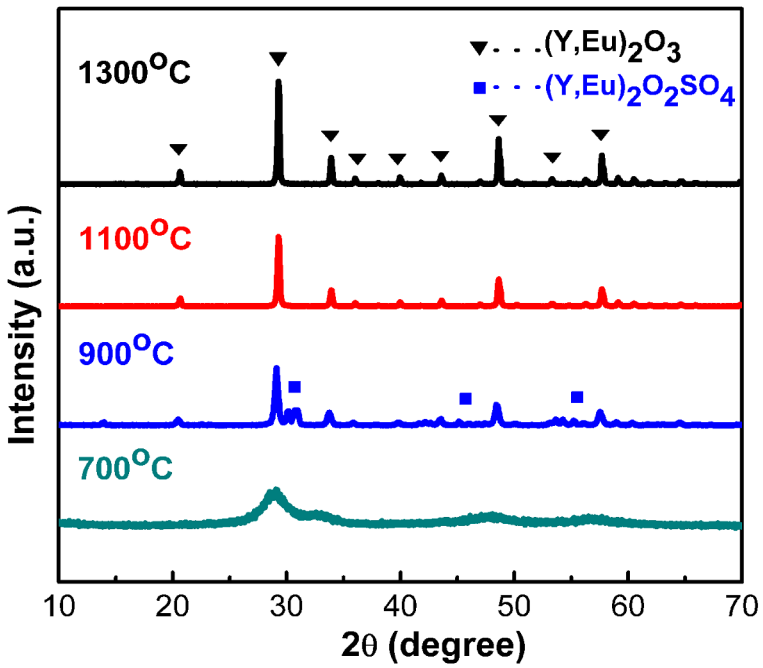

Fig. 3.4 XRD patterns of the products calcined from the sulfate-type LRH (*R*=0.25) at various temperatures.

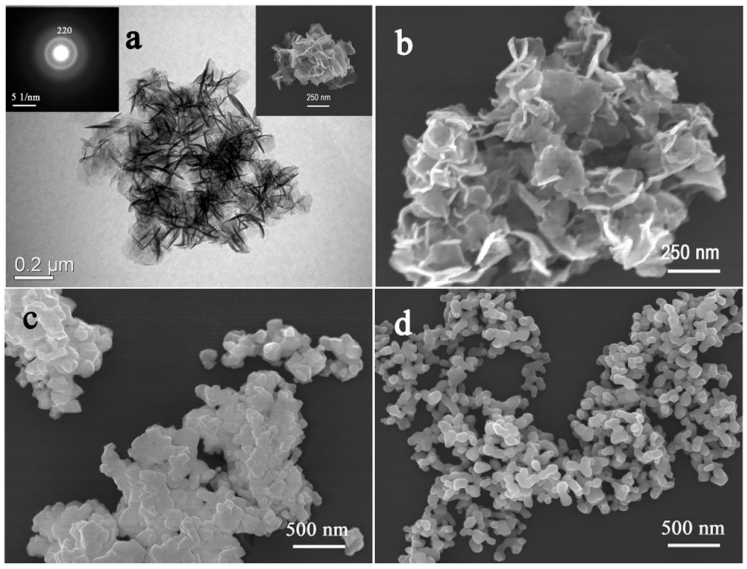

Fig. 3.5 TEM (a) and FE-SEM (b-d) micrographs showing morphologies of the nitrate-type LRH (a), the sulfate-type LRH (b), and the oxide powders calcined from the nitrate-type LRH (c) and sulfate-type LRH (d). The insets in panel (a) are the SAED pattern (left) and FE-SEM image (right).

Figure 3.5 shows morphologies of the two kinds of LRHs and their oxides calcined at 1100 °C for 4 h. The NO_3^--LRH exhibits a typical 2*D* nanosheet shape with a relatively uniform thickness of up to 7 nm (Fig. 3.5a). Selected area electron diffraction (SAED) proves that the product is crystalline, in accordance with the result of XRD, and the 220 diffraction ring corresponds to the *ab* plane (hydroxide main layer) of the LRH crystal (Fig. 3.5a inset). Its calcination particles agglomerate together (Fig. 3.5c). The SO_4^{2-}-LRH retain the nanosheet morphology and anion-exchange does not bring about appreciable morphology change (Fig. 3.5b, R=2), but induces oxide powders of finer particles and much better dispersion (Fig. 3.5d). Such a large difference could be ascribed to the effects of SO_4^{2-} in the interlayer. That is, it significantly alters the thermal decomposition pathway of LRH by introducing an additional $Ln_2O_2SO_4$ phase in the ~700-1000 °C range (Fig. 3.3). The resultant $Ln_2O_2SO_4$ is finely distributed in the already formed oxide matrix, inhibiting surface diffusion and inter-particle sintering, and hence well-dispersed and finer oxide particles are formed. It should be noted that the both types of LRHs partially keep their nanosheet morphologies up to ~900 °C,[37] and thus a reasonably high calcination temperature is preferred to produce rounded oxide particles.

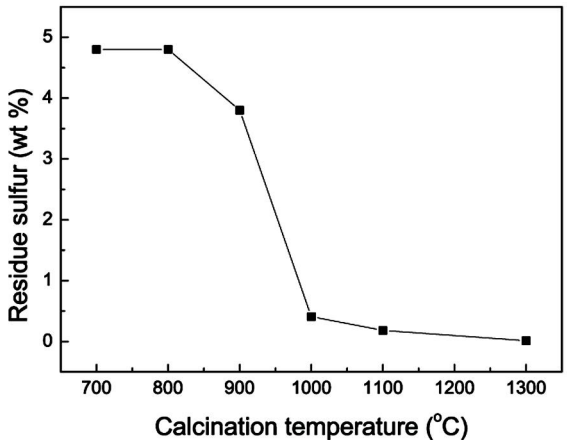

Fig. 3.6 Sulfur contents of the sulfate-type LRH (R=0.25) calcined at various temperatures for 4 h.

Figure 3.6 shows the result of elemental analysis for the sulfur contents of the sulfate-type LRH (R=0.25) calcined at various temperatures for 4 h. The sulfur content is almost constant up to ~800 °C, followed by rapid decreases due to the thermal decomposition of $Ln_2O_2SO_4$ phase. Only ~0.18 wt% of S was detected at 1100 °C, possibly arising from surface adsorbed SOx. The sulfur is no more unambiguously detectable by the analysis method (detection limit: 0.01 wt%) at a higher temperature of 1300 °C.

3.3.2 Significant reduction of hard agglomeration

Hard agglomerates are difficult to break down via compaction,[41,42] leading to heterogeneous microstructures in the green body and differential sintering. We found that the Ln^{3+} concentration for LRH synthesis significantly affect the extent of dispersion of the resultant oxides. For example, the powder obtained with [Ln^{3+}]=0.2 M shows good local dispersion (Fig. 3.7a), but many hard agglomerates can be found under low magnification FE-SEM observation (Fig. 3.7b). For this powder, LDPSA shows a narrow particle-size distribution in cumulative number (Fig. 3.7c) but a bimodal distribution in cumulative volume due to the presence of large agglomerates (Fig. 3.7d). Volume distribution is thus more valid for detecting hard agglomerates. We experimentally found that [Ln^{3+}]=0.1 M might be the boundary concentration for oxide powders of desired properties and the results are poorly repeatable. That is, it sometimes yielded powders of unimodal size distribution in volume (Fig. 3.8a and c) and sometimes produced powders with hard agglomerates (Fig. 3.8b and d). Hard agglomeration can be significantly reduced by further lowering the Ln^{3+} concentration to 0.05-0.075 M without any other treatment (Fig. 3.9c), and the results are highly repeatable. Under too low Ln^{3+} concentration (e.g. 0.01 M), the as-synthesized LRHs are better separated from each other in the slurry but undergo dense packing upon collection via suction filtration and subsequent drying, resulting in a hard mass difficult to collapse by calcination. The best concentration is thus 0.05-0.075 M for the Y/Eu binary system, and 0.075 M is preferred for its higher batch yield.

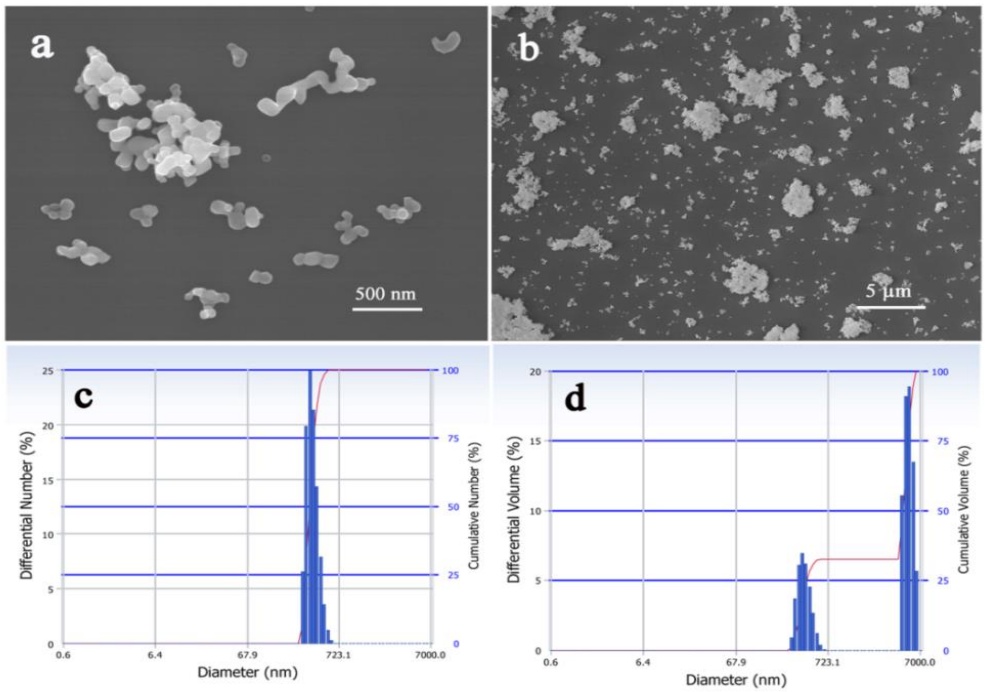

Fig. 3.7 FE-SEM micrographs (a, b) of the oxide powder calcined from the LRH synthesized at [Ln^{3+}]=0.2 M, and the LDPSA in cumulative number (c) and volume (d).

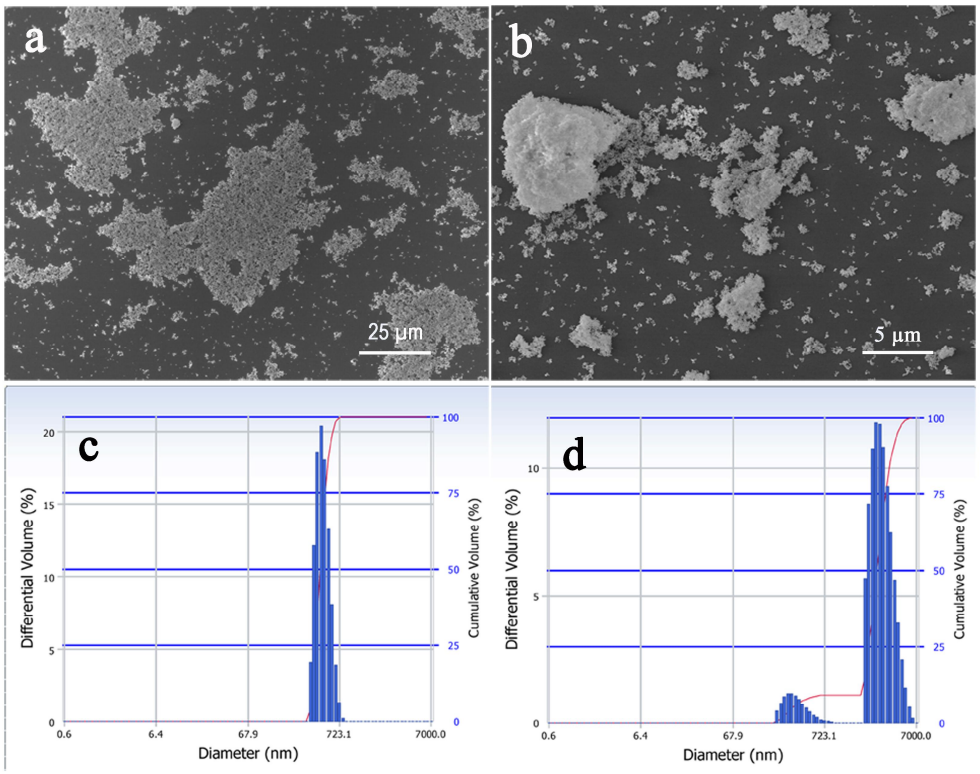

Fig. 3.8 FE-SEM micrographs (a, b) of the oxide particles calcined from the LRH synthesized at $[Ln^{3+}]$=0.1 M of and the LDPSA in cumulative volume (c, d).

3.3.3 Impacts of R on properties of the resultant oxides and ceramic transmittances

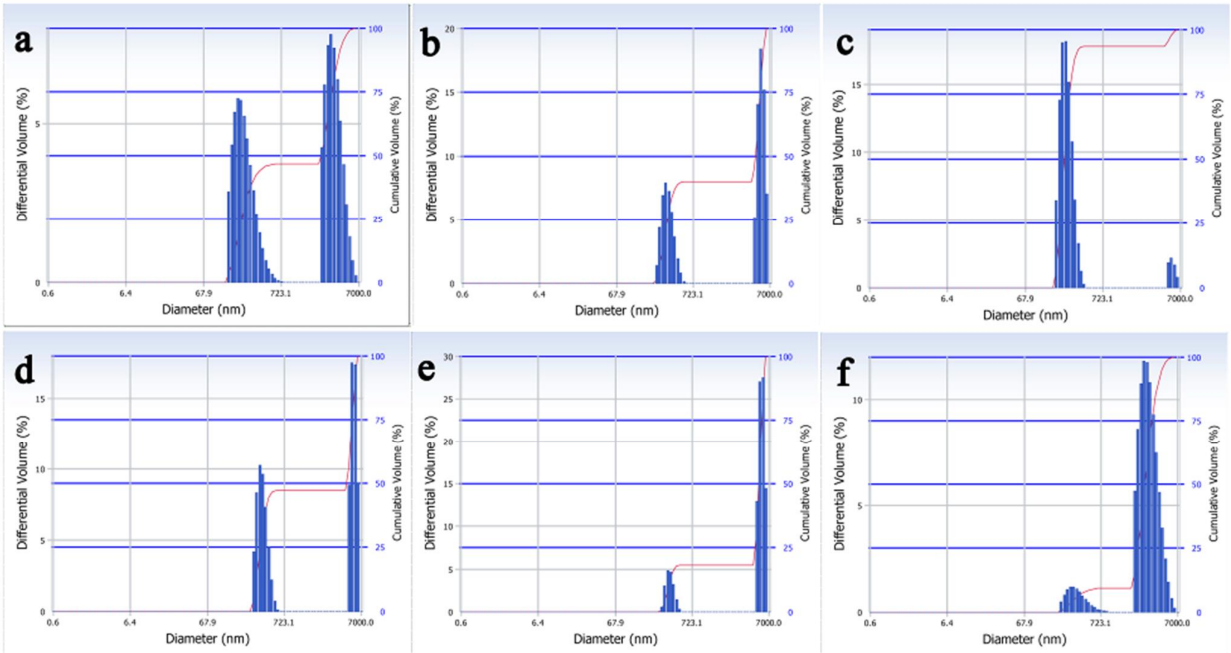

Fig. 3.9 LDPSA in cumulative volume for the oxides calcined at 1100 °C for 4 h, with (a)-(f) corresponding to the LRH precursors made at *R*=0 (a), 0.005 (b), 0.03 (c), 0.1 (d), 0.25 (e), and 1.0 (f).

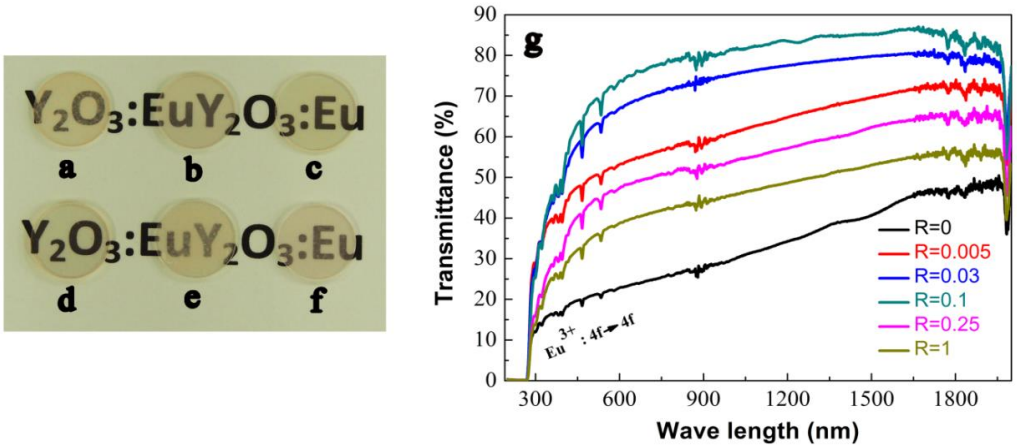

Fig. 3.10 Appearances of the transparent $(Y_{0.95}Eu_{0.05})_2O_3$ ceramics fabricated from the LRHs sulfate-exchanged at *R*=0 (a), *R*=0.005 (b), *R*=0.03 (c), *R*=0.1 (d), *R*=0.25 (e), *R*=1 (f), and their in-line transmittances (g). All the powders were calcined at 1100 °C for 4 h. Samples were fabricated via vacuum sintering at 1700 °C for 4 h, with a heating rate of 8 °C/min in the ramp stage.

Figure 3.9 exhibits the LDPSA results in cumulative volume for the oxide powders calcined from the LRH nanosheets synthesized at *R*=0-1.0. It can be seen that the amount of sulfate (*R* value) affects the extent of particle dispersion. The particles have specific surface areas of ~12.8, 10.3, 14.8, 13.2, 14.6, and 15.0 m^2/g at increasing *R* from 0 to 1.0. The *R*=0.03 and 0.1 samples have sharper size distribution with fewer agglomerates, and thus their ceramics vacuum sintered at 1700 °C for 4 h with a heating rate of 8 °C/min show higher transmittances of ~67.3 and 73.6% at the wavelength of 613 nm Eu^{3+} emission (Fig. 3.10). Under identical sintering, the other ceramics have transmittances of only ~23, 53, 48 and 40% at 613 nm for *R*=0, 0.005, 0.25 and 1.0, respectively. Better dispersion/sharper size distribution may induce a concentrated pore size distribution in the green body and also decreased coordination number of the pores,[43] through which uniform sintering/pore removal was significantly promoted for yielding better transparent ceramics. In the following, the molar ratio of *R*=0.03 was selected to synthesize the oxide powders for transparent $(Y_{0.95}Eu_{0.05})_2O_3$ ceramics because of its lower yet effective amount of SO_4^{2-} in the LRH precursor.

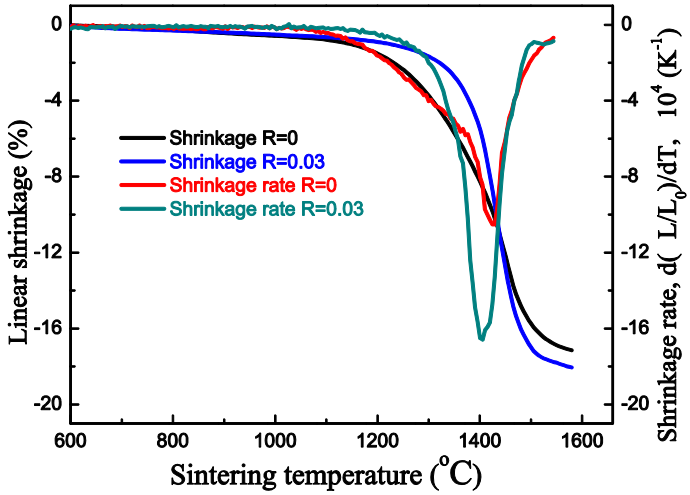

Fig. 3.11 Linear shrinkage and shrinkage rate for the green bodies compacted with the powders synthesized with *R*=0 and 0.03, under a constant heating rate of 10 °C/min.

Figure 3.11 compares linear shrinkage and linear shrinkage rate for the compacts of two different powders. Differential sintering in the wide temperature range of 1100-1500 °C was clearly observed for the R=0 sample, as evidenced by the appearance of a slow shoulder (~1100-1390 °C) on the shrinkage rate curve. The maximum rate was found to be ~10.5×10^4/K at 1460 °C. The sequential sintering can be ascribed to structure heterogeneity in the green body arising from the significant bimodal particle size distribution of the powder (Fig. 3.9a). Whereas, the R=0.03 specimen exhibits a unimodal densification with a sharp rate peak in the narrower temperature range of ~1300-1500 °C. The maximum shrinkage rate was ~16.6×10^4/K at the lower temperature of ~1430 °C, which is roughly 1.6 times that of the R=0 specimen. Such a difference can be attributed to the better dispersion and fewer aggregates of the R=0.03 powder. For the same reason, the R=0.03 sample has a higher green density (~57.2%) than the R=0 one (~53.5%) under identical compaction (~400 MPa).

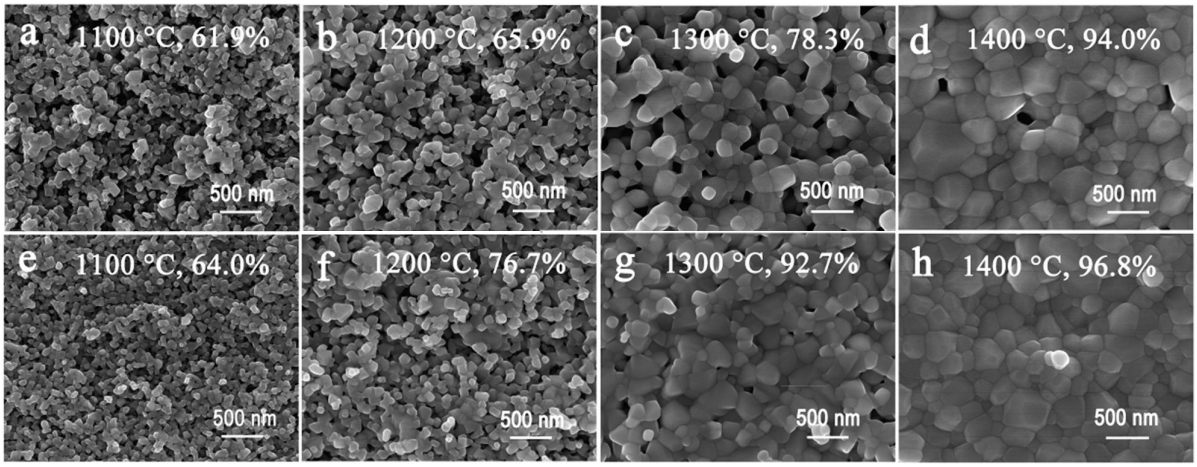

Fig. 3.12 FE-SEM micrographs showing surface morphologies of the vacuum-sintered $(Y_{0.95}Eu_{0.05})_2O_3$ ceramics. The oxide powders were calcined from the LRH precursors synthesized at R=0 for (a)-(d) and at R=0.03 for (e)-(h). The sintering temperature and relative density are indicated in each figure, and the heating rate for sintering is 8 °C/min.

Figure 3.12 displays surface morphologies of the ceramic bodies vacuum-sintered at 1100-1400 °C for 4 h, with the relative density indicated in the picture. The R=0.03 sample generally shows a more homogeneous microstructure and a higher density than the R=0 one at each temperature. The difference in sintered density between the two samples enlarges with increasing temperature, and at 1300 °C it reached ~14.4%. The R=0.03 sample attained a relative density of ~96.8% at the quite low temperature of 1400 °C, and open pores have largely been removed. In addition, the untreated surface appeared more dense than the polished surface (Fig. 3.13a and b), owing to the prior to sintering on the ceramic surface.

Figure 3.13 shows microstructures of the thermally etched ceramics, along with statistical frequency plots of the dihedral angle (θ) analyzed from at least 100 grains with the WinRoof image analysis software. The relation between θ, grain-boundary energy (γ_b) and surface energy (γ_s) can be expressed as $\gamma_b=2\gamma_s\cos\theta$,[44] and thus the θ dispersion can be a direct reflection of the driving force for densification.[45] At the sintering temperature of 1400 °C, the R=0.03 sintered body shows a narrower θ dispersion than the R=0 one, elucidating a more uniform microstructure arising from uniform densification. The average grain size was analyzed to be ~411 and ~369 nm for the R=0 and 0.03 specimens, respectively. Narrow θ dispersion was found for both the ceramics sintered at 1700 °C, owing to grain boundary straightening and the preferential

disappearance of smaller grains via growth. Again, the R=0.03 specimen has a much narrower θ dispersion. Residual pores are only occasionally observable inside the ceramics sintered at 1700 °C, and the R=0 and 0.03 samples have respective average grain sizes of ~19 and 14 μm with relative densities of ~100%.

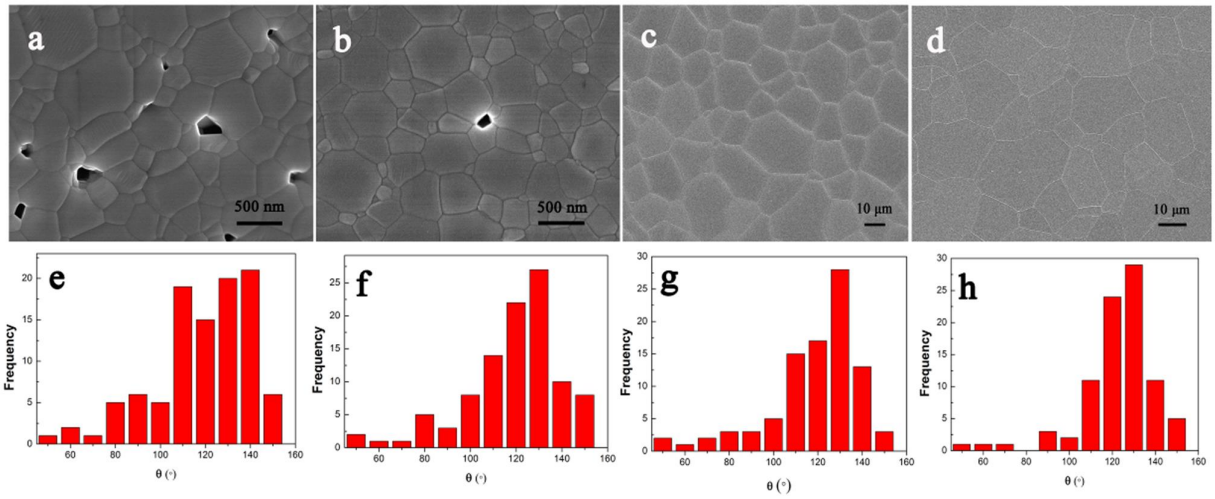

Fig. 3.13 FE-SEM micrographs showing microstructures of the $(Y_{0.95}Eu_{0.05})_2O_3$ ceramics vacuum sintered at 1400 °C (a, b) and 1700 °C (c, d). The R value used for powder synthesis is 0 for Figs. 6a,c and 0.03 for Figs. 6b,d. Frequency plots of dihedral angle are shown in (e)-(h) for the four samples, respectively. The heating rate for sintering is 8 °C/min.

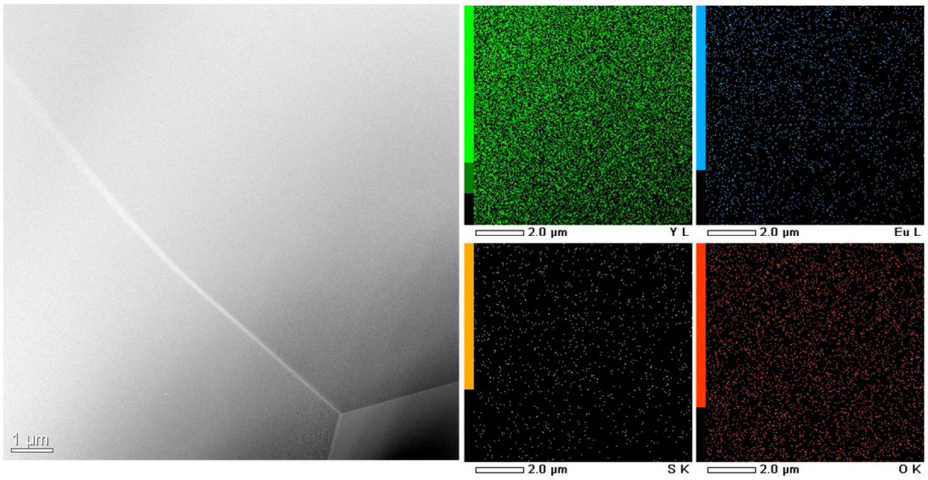

Fig. 3.14 TEM micrograph of a triple junction area for the R=0.03 ceramic vacuum-sintered at 1700 °C for 4 h (left panel) and the results of elemental mapping for Y, Eu, S and O distributions (right panel).

Elemental mapping of Y, Eu, S, and O for the R=0.03 ceramic vacuum-sintered at 1700 °C indicated that the four elements are evenly distributed without amorphous phase and any appreciable segregation either along grain boundary or at the triple junction (Fig. 3.14). Chemical analysis confirmed that the amount of sulfur, if there is any, is below the detection limit (0.01%) of the analyzer.

3.3.4 Advantages of the freezing-temperature technique for LRH synthesis and effects of heating rate on optical properties of the ceramics

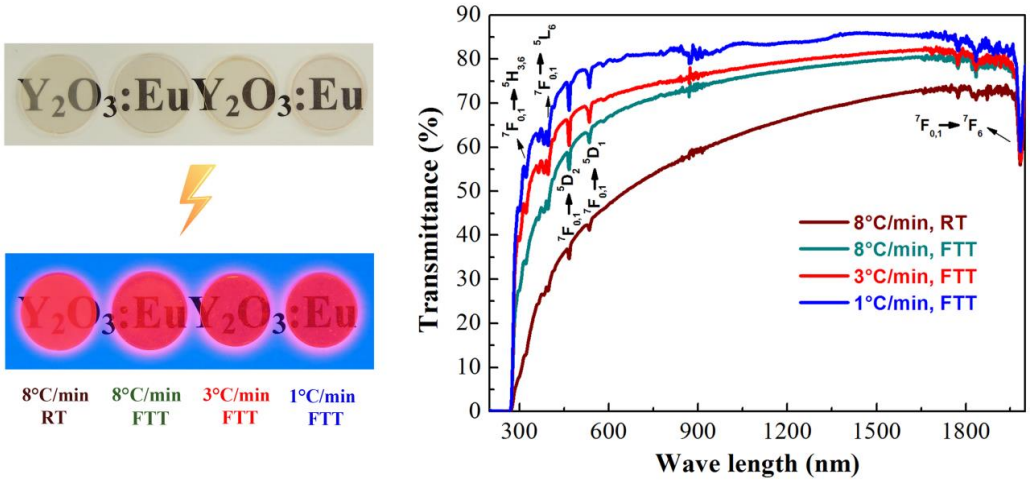

Fig. 3.15 Appearances (left panel, digital pictures) and in-line transmittances (right panel) of the transparent $(Y_{0.95}Eu_{0.05})_2O_3$ ceramics prepared under different conditions. The heating rate for vacuum sintering is included in the right panel, where ñRTò and ñFTTò denote LRHs synthesis at room temperature and ~4 °C, respectively. All the samples are vacuum sintered at 1700 °C for 4 h. The lower part of the left panel is the observed red Eu^{3+}emission under excitation from a 254 nm UV lamp.

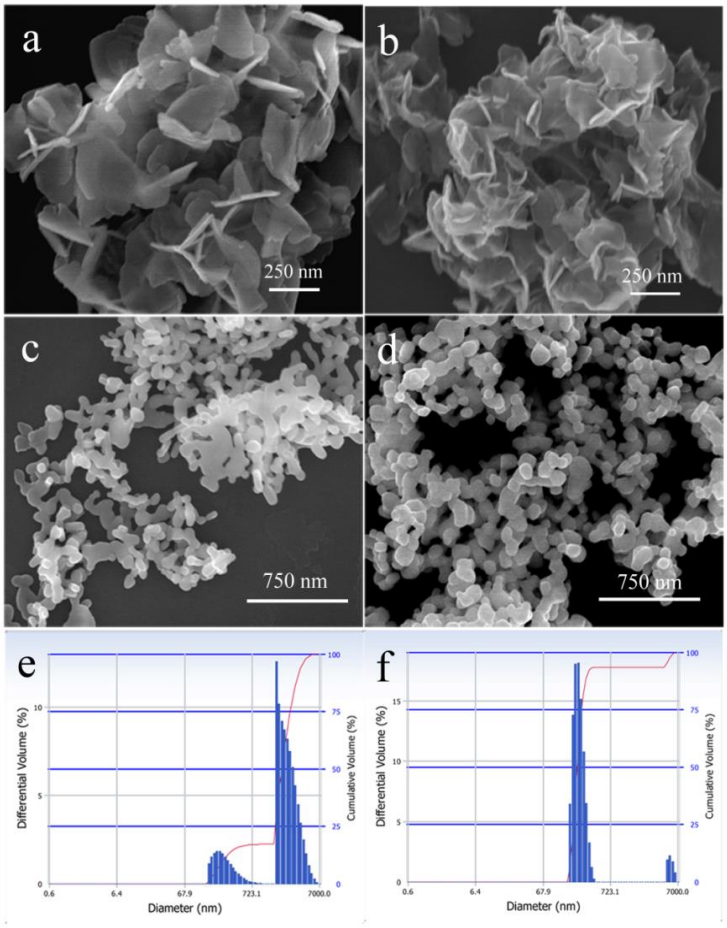

Fig. 3.16 FE-SEM micrographs of the LRHs synthesized at room temperature (a) and freezing temperature (b), and their calcination products (c) and (d), respectively. (e) and (f) are the LDPSA of the oxides.

Figure 3.15 shows optical transmittances and appearances of the ceramics fabricated under different conditions for comparison. It is seen that, under identical sintering, the ceramic fabricated from the LRH synthesized by the freezing temperature technique (FTT) has an inline transmittance ~20% higher than that made from room-temperature (RT) LRH over the visible region, and exhibits better transparency to the naked eyes. This is because the nanosheets synthesized via FTT are much thinner and the resultant oxide powder exhibits a narrower size distribution (Fig. 3.16). Therefore, it is demonstrated that FTT is an excellent way for yielding highly sinterable $(Y_{0.95}Eu_{0.05})_2O_3$ powders via preventing the LRH growth in thickness.

Heating rate in the ramp stage of vacuum sintering significantly influences optical performances of the final ceramics. That is, slower heating rate leads to better optical-quality ceramics ascribed to much more uniform densification in the whole ceramic body (Fig. 3.15). The absorption bands indicated on the transmittance curve correspond to the intra-$4f^6$ transitions of Eu^{3+}, and the starting wavelength of transmittance is located at ~270 nm for all the samples. Upon UV irradiation at 254 nm, the $(Y_{0.95}Eu_{0.05})_2O_3$ ceramics all emit strong red emissions that correspond to the $^5D_0$Ÿ $^7F_{1,2}$ transitions of Eu^{3+} (Fig. 3.15, the lower part of the left panel).

3.3.5 Effects of sintering temperature and powder calcination on transmittance

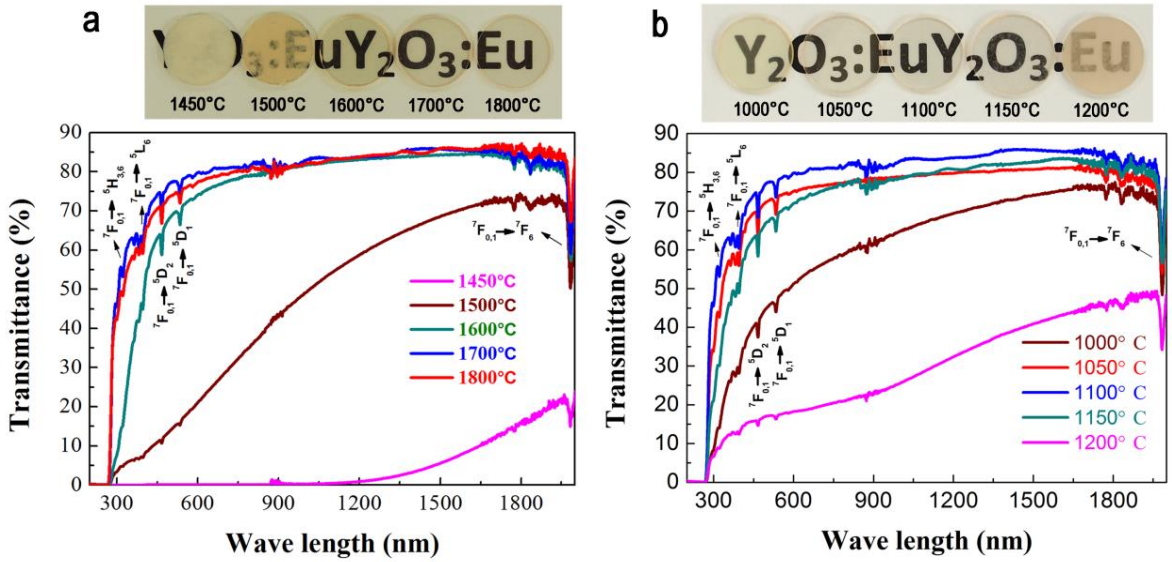

Fig. 3.17 Appearances (upper part, digital pictures) and in-line transmittances (lower part) of the vacuum sintered $(Y_{0.95}Eu_{0.05})_2O_3$ transparent ceramics. Parts a and b reveal the effects of sintering temperature and power calcination, respectively. The heating rate for vacuum sintering is 1 °C/min in each case and the samples are all 1 mm in thickness.

Figure 3.17a reveals the effects of sintering temperature on transparency. The ceramic sintered at 1450 °C is nearly opaque in the visible region and exhibits translucency up to 24% in the near infrared region of 1200-2000 nm. An only 50 °C increment to 1500 °C substantially improved the ceramic optical quality to become translucence in the visible region. Sintering at 1600 °C drastically enhanced the transparency in the visible wavelength via greatly eliminating small pores in diffusion process. The ceramic has an inline transparency over 80% in the region of 1000-2000 nm, already being sufficient for near-infrared applications. Such a low sintering temperature further proves the superiority of our powder processing and sintering

techniques. The ceramic made at 1700 °C has the best overall transmittance in the measured wavelength region, while the higher temperature of 1800 °C led to no optical improvement and larger grain sizes of ~70 εm.

Figure 3.17b shows appearances and in-line transmittances of the ceramics fabricated by vacuum sintering at 1700 °C, with oxide powders calcined at 1000-1200 °C. Powder calcination significantly influences particle size and size distribution of the powder (Fig. 3.18), as a result to affect optical quality of the final ceramics. Calcining at 1000 °C, the powder has a very fine particle size, resulting in the relatively low green density of ~55.0% and possibly also a less uniform microstructure in the green body. The powders calcined at 1050-1200 °C can all be compacted to the similar green densities of ~57.2%, but the 1100 °C one has the narrowest size distribution and thus yields the most transparent ceramic.

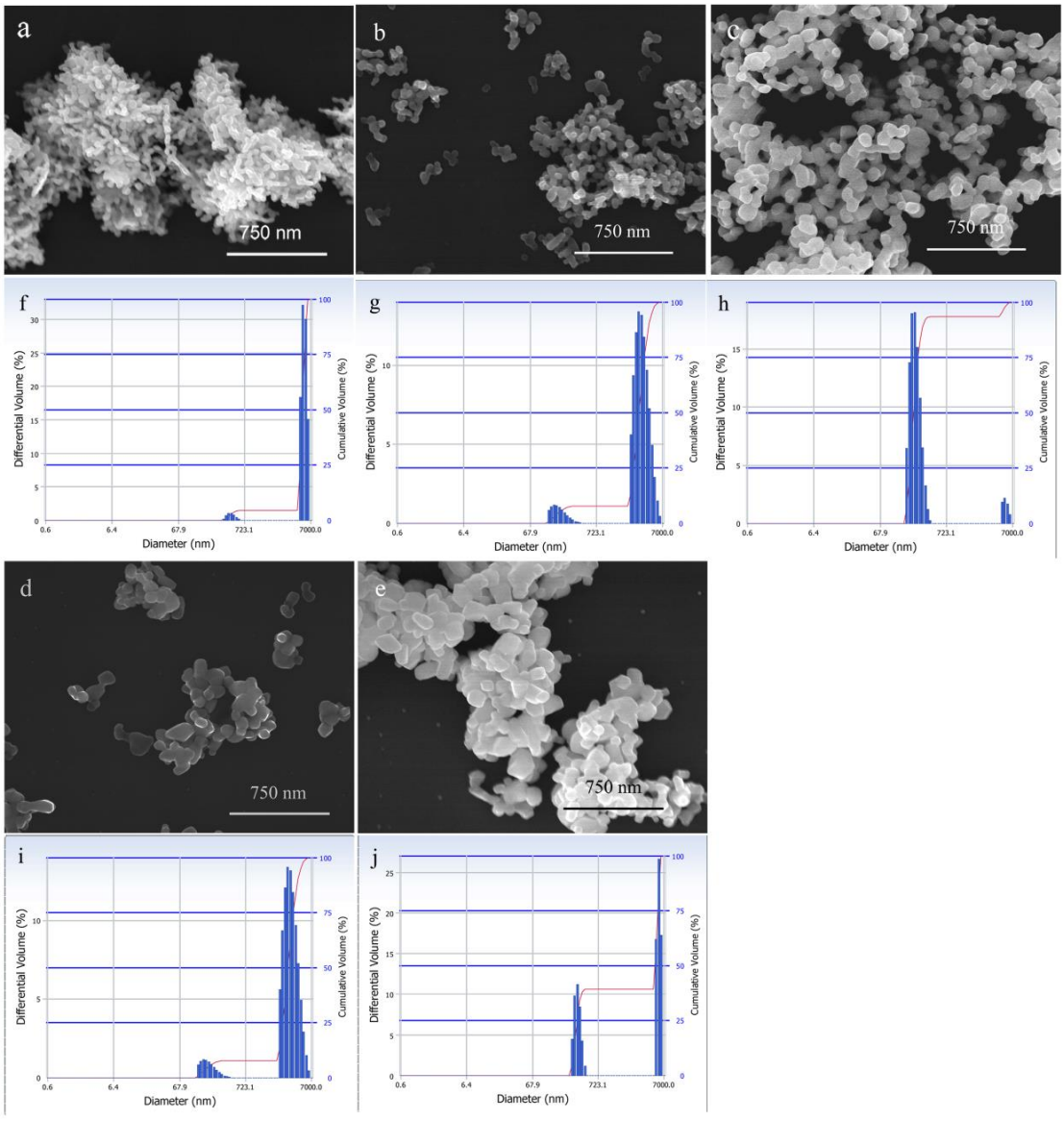

Fig. 3.18 FE-SEM micrographs of the $(Y_{0.95}Eu_{0.05})_2O_3$ oxide phosphors calcined at 1000 (a), 1050 (b), 1100 (c), 1150 (d), and 1200 °C (e). (f)-(j) are the corresponding LDPSA in cumulative volume, respectively.

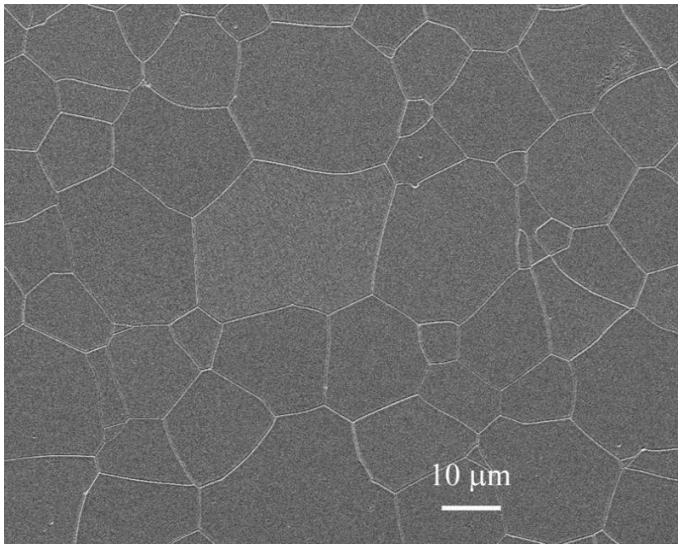

Fig. 3.19 FE-SEM micrograph showing microstructure of the transparent $(Y_{0.95}Eu_{0.05})_2O_3$ ceramic fabricated under the optimized conditions stated in the main text.

The best $(Y_{0.95}Eu_{0.05})_2O_3$ ceramic obtained in this work has an in-line transmittance of ~80% at 613 nm (Fig. 3.17) and a fine average grain size of ~14 μm without any abnormal grain growth (Fig. 3.19).

The theoretical transmittance of a defect-free single crystal can be calculated from the following two equations:

$$T = (1-R)^2 \exp(-\alpha t) \qquad (3.1)$$

$$R = \frac{(n-1)^2}{(n+1)^2} \qquad (3.2)$$

where α is the loss factor, t is the sample thickness, and n is the refractive index.

For a defect-free Y_2O_3 single crystal, the relationship between refractive index and wavelength (λ) can be expressed as equation (3.3):[46]

$$n^2 = 1 + \frac{2.578\lambda^2}{\lambda^2 - 0.1387^2} + \frac{3.935\lambda^2}{\lambda^2 - 22.936^2} \qquad (3.3)$$

from which the n value was calculated to be ~1.93 for the wavelength of 613 nm. Applying equations (3.1) and (3.2) yielded a theoretical transmittance of ~81% at 613 nm (assuming α=0). The highest transparency (~80%) of $(Y_{0.95}Eu_{0.05})_2O_3$ ceramic attained in this study is thus ~99% of the theoretical value.

3.3.6 Photoluminescence behaviors of the phosphor powder and transparent ceramic

Photoluminescence (PL) and photoluminescence excitation (PLE) spectra of the $(Y_{0.95}Eu_{0.05})_2O_3$ phosphor powder and transparent ceramic are shown in Fig. 3.20. Both the material forms exhibit the typical Eu^{3+} emissions driven from the $^5D_0$ → ^7F_J (J=0-4) transitions as indicated in the figure.[47,48] The strongest emission peaks are located at ~613 nm upon UV excitation into the charge-transfer (CT) band arising from electron transition from the 2*p* orbital of O^{2-} to the 4*f* orbital of Eu^{3+}. The three groups of excitation peaks beyond 290 nm are ascribed to the intra-4f^6 electronic transitions of Eu^{3+}. Red-shift CT band center of the

ceramic was clearly observed from 250 nm of the powder to 267 nm since the ceramic has a smaller surface/grain-boundary area and larger grain size. The bulk material possesses much stronger PL and PLE intensities (~150%) than the powder form owing to significantly reduced nonradiative relaxation after high-temperature sintering. Fluorescence decay behaviors of the 613 nm emission under excitation with the peak wavelength of the CT band are shown as inset in the figure. Fluorescence lifetime can be calculated by fitting the decay curve with the single exponential equation $I=Aexp(-t/\tau)+B$, where I is the emission intensity, τ is the fluorescence lifetime, t is the decay time, and A and B are constants. The fittings yielded a much shorter lifetime of the bulk (1.22±0.01 ms) than that of powder (2.83±0.01 ms). For C-type cubic RE_2O_3, there are two crystallographic positions for Eu^{3+} occupancy, that is, the non-centrosymmetric C_2 and centrosymmetric S_6 (C_{3i}) sites. Concas et al.[49] indicated that Eu^{3+} is almost randomly trapped at the two sites in nanocrystalline particles, while it is preferentially trapped at the C_2 site in the bulk material owing to its state being close to equilibrium. Additionally, the Eu^{3+} located at the C_2 site will cause a much shorter lifetime than that at the S_6 site.[50,51] Therefore, the ceramic has a much shorter lifetime than the phosphor powder. The fluorescence lifetimes determined in the present study all fall within the reported values of 1.8-3.1 ms for Y_2O_3:Eu phosphors[35,52-54] and 1.0-1.6 ms for $(Y,La)_2O_3$:Eu and Lu_2O_3:Eu ceramics.[15,55]

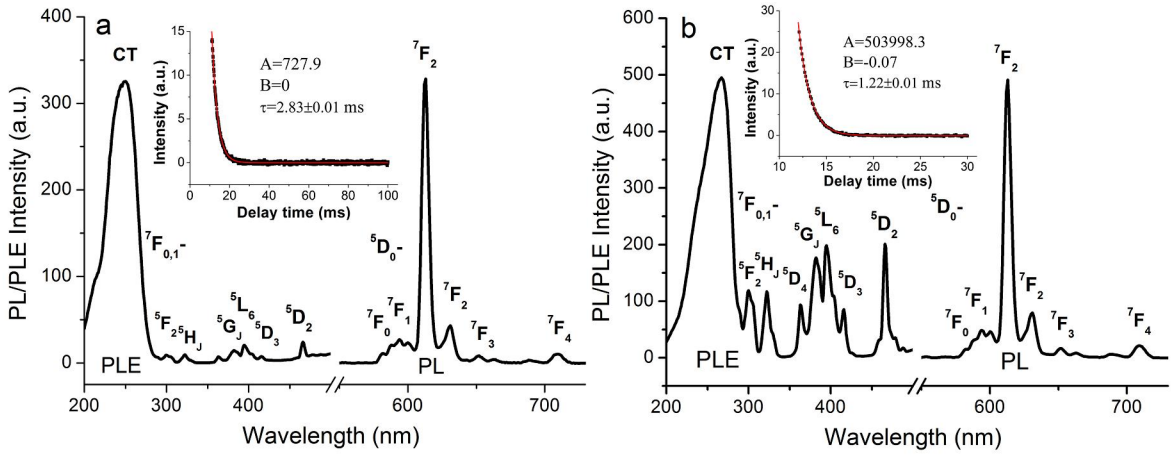

Fig. 3.20 PL and PLE spectra of the $(Y_{0.95}Eu_{0.05})_2O_3$:Eu phosphor powder calcined at 1100 °C (a) and the best transparent ceramic shown in Fig. 3.15. The insets are fluorescence decay behaviors of the 613 nm emission.

3.4 Conclusions

Two-dimensional layered rare-earth hydroxide (LRH) nanosheets, after properly anion-exchanged with SO_4^{2-}, was demonstrated to be an excellent precursor for yielding well-dispersed oxide powders and highly transparent Ln_2O_3 ceramics ($Ln=Y_{0.95}Eu_{0.05}$). Our detailed investigation on powder processing and sintering have led to the following main conclusions:

(1) the optimal combination of processing parameters to synthesize the best sinterable oxide powders may include freezing temperature synthesis of LRH at $[Ln^{3+}]$=0.05-0.075 M, anion exchange of the interlayer NO_3^- at the SO_4^{2-}/Ln^{3+} molar ratio of 0.03, and particle calcination temperature of 1100 °C;

(2) Sulfate exchange appreciably shortens the interlayer distance and significantly alters the thermal decomposition pathway of LRH. The occurrence of $Ln_2O_2SO_4$ intermediate upon precursor calcination was found beneficial to the generation of less hard agglomerated and readily sinterable oxide powders;

(3) Slower heating in the ramp stage of vacuum sintering benefits optical quality of the final ceramic and the optimal sintering temperature is 1700 °C. The best $(Y_{0.95}Eu_{0.05})_2O_3$ transparent ceramic has a fine average grain size of ~14 μm and a high in-line transmittance of ~80% at the Eu^{3+} emission wavelength of 613 nm;

(4) Both the oxide powders and transparent ceramics exhibit the strongest red emission of Eu^{3+} at ~613 nm under charge transfer excitation. Red-shifted CT band center, stronger excitation/emission, and shorter fluorescence lifetime were observed for the transparent ceramics.

3.5 References

[1]Y. C. Kang, H. S. Roh, and S. B. Park, ñPreparation of Y_2O_3:Eu Phosphor Particles of Filled Morphology at High Precursor Concentrations by Spray Pyrolysis,ò *Adv. Mater.*, **12** [6] 451-3 (2000).

[2]G. Wakefield, E. Holland, P. J. Dobson, and J. L. Hutchison, ñLuminescence Properties of Nanocrystalline Y_2O_3:Eu,ò *Adv. Mater.*, **13** [20] 1557-60 (2001).

[3]J.-G. Li, X. D. Li, X. D. Sun, T. Ikegami, and T. Ishigaki, ñUniform Colloidal Spheres for $(Y_{1-x}Gd_x)_2O_3$ (x = 0-1): Formation Mechanism, Compositional Impacts, and Physicochemical Properties of the Oxides,ò *Chem. Mater.*, **20** [6] 2274-81 (2008).

[4]L. E. Shea, J. McKittrick, and O. A. Lopez, ñSynthesis of Red-Emitting, Small Particle Size Luminescent Oxides Using an Optimized Combustion Process,ò *J. Am. Ceram. Soc.*, **79** [12] 3257-65 (1996).

[5]S.-H. Byeon, M.-G. Ko, J.-C. Park, and D.-K. Kim, ñLow-Temperature Crystallization and Highly Enhanced Photoluminescence of $Gd_{2-x}Y_xO_3$:Eu^{3+} by Li Doping,ò *Chem. Mater.*, **14** [2] 603-8 (2002).

[6]J. K. Li, J.-G. Li, Z. J. Zhang, X. L. Wu, S. H. Liu, X. D. Li, X. D. Sun, and Y. Sakka, ñGadolinium Aluminate Garnet ($Gd_3Al_5O_{12}$): Crystal Structure Stabilization via Lutetium Doping and Properties of the $(Gd_{1-x}Lu_x)_3Al_5O_{12}$ Solid Solutions (x = 0ï0.5),ò *J. Am. Ceram. Soc.*, **95** [3] 931-6 (2012).

[7]C. D. Greskovich, D. Cusano, D. Hoffman, and R. J. Riedner, ñCeramic Scintillators for Advanced, Medical X-ray Detectors,ò *Am. Ceram. Soc. Bull.*, **71** [7] 1120-30 (1992).

[8]C. Greskovich and S. Duclos, ñCeramic Scintillators,ò *Annu. Rev. Mater. Sci.*, **27** 69-88 (1997).

[9]J.-G. Li, T. Ikegami, and T. Mori, ñFabrication of Transparent, Sintered Sc_2O_3 Ceramics,ò *J. Am. Ceram. Soc.*, **88** [4] 817ï21 (2005).

[10]X. D. Li, X. D. Sun, J.-G. Li, Z. M. Xiu, T. Gao, Y. N. Liu, and X. Z. Hu, ñCharacterization of High-Gadolinium $Y_{0.6}Gd_{1.34}Eu_{0.06}O_3$ Powder and Fabrication of Transparent Ceramic Scintillator Using Pressureless Sintering,ò *Int. J. Appl. Ceram. Technol.*, **7** [S1] E1-8 (2010).

[11]Y. Wang, B. Lu, X. D. Sun, T. Sun, and H. Xu, ñSynthesis of Nanocrystalline Sc_2O_3 Powder and Fabrication of Transparent Sc_2O_3 Ceramics,ò *Adv. Appl. Ceram.*, **110** [2] 95-8 (2011).

[12]B. Lu, Y. Wang, X. D. Sun, and T. Sun, ñSynthesis of Sc_2O_3 Nanopowders and Fabrication of Transparent, Two-Step Sintered Sc_2O_3 Ceramics,ò *Adv. Appl. Ceram.*, **111** [7] 389-92 (2012).

[13]Y. H. Huang, D. L. Jiang, J. X. Zhang, and Q. L. Lin, ñFabrication of Transparent Lanthanum-Doped Yttria Ceramics by Combination of Two-Step Sintering and Vacuum Sintering,ò *J. Am. Ceram. Soc.*, **92** [12] 2883-7 (2009).

[14]S. N. Bagayev, V. V. Osipov, V. A. Shitov, E. V. Pestryakov, V. S. Kijko, R. N. Maksimov, K. E. Lukyashin, A. N. Orlov, K. V. Polyakov, and V. V. Petrov, ñFabrication and Optical Properties of Y_2O_3-Based Ceramics with Broad Emission Bandwidth,ò *J. Eur. Ceram. Soc.*, **32** [16] 4257-62 (2012).

[15]S. Z. Lu, Q. H. Yang, Y. G. Wang, Y. H. Li, and D. D. Huang, ñLuminescent Properties of Eu:$Y_{1.8}La_{0.2}O_3$ Transparent Ceramics for Potential White LED Applications,ò *Opt. Mater.*, **35** [4] 718-21 (2013).

[16]G. L. Messing and A. J. Stevenson, ñToward Pore-Free Ceramics,ò *Science*, **322** [5900] 383-4 (2008).

[17]H. B. Zhang, B.-N. Kim, K. Morita, H. Yoshida, K. Hiraga, Y. Sakka, and J. Ballato, ñFabrication of Transparent Yttria by High-Pressure Spark Plasma Sintering,ò *J. Am. Ceram. Soc.*, **94** [10] 3206-10 (2011).

[18]S. Grasso, C. Hu, G. Maizza, B. Kim, and Y. Sakka, ñEffects of Pressure Application Method on Transparency of Spark Plasma Sintered Alumina,ò *J. Am. Ceram. Soc.*, **94** [5] 1405-9 (2011).

[19]L. Ji and Y. Jiang, ñLaser Sintering of Transparent Ta_2O_5 Dielectric Ceramics,ò *Mater. Lett.*, **60** [12] 1502-4 (2006).

[20]J. P. Cheng, D. Agrawal, Y. J. Zhang, B. Drawl, and R. Roy, ñFabricating Transparent Ceramics by Microwave Sintering,ò *Am. Ceram. Soc. Bull.*, **79** [9] 71-4 (2000).

[21]S. V. Egorov, Y. V. Bykov, A. G. Eremeev, and A. A. Sorokin, ñLaser Ceramics Sintering by Millimeter-Wave Heating,ò *Radiophys. Quantum Electron.*, **56** [8-9] 574-81 (2014) .

[22]L. J. McIntyre, L. K. Jackson, and A. M. Fogg, ñ$Ln_2(OH)_5NO_3{\cdot}xH_2O$ (Ln=Y, Gd-Lu): A Novel Family of Anion Exchange Intercalation Hosts,ò *Chem. Mater.*, **20** [1] 335-40 (2008).

[23]K.-H. Lee and S.-H. Byeon, ñExtended Members of the Layered Rare-Earth Hydroxides Family, $RE_2(OH)_5NO_3{\cdot}nH_2O$ (RE = Sm, Eu, and Gd): Synthesis and Anion-Exchange Behaviour,ò *Eur. J. Inorg. Chem.*, **2009** [7] 929-36 (2009).

[24]L. Poudret, T. J. Prior, L. J. McIntyre, and A. M. Fogg, ñSynthesis and Crystal Structures of New Lanthanide Hydroxyhalide Anion Exchange Materials, $Ln_2(OH)_5X{\cdot}1.5H_2O$ (X = Cl, Br; Ln=Y, Dy, Er, Yb),ò *Chem. Mater.*, **20** [24] 7447-53 (2008).

[25]K.-H. Lee and S.-H. Byeon, ñSynthesis and Aqueous Colloidal Solutions of $RE_2(OH)_5NO_3{\cdot}nH_2O$ (RE = Nd and La),ò *Eur. J. Inorg. Chem.*, **2009** [31] 4727-32 (2009).

[26]F. Gándara, J. Perles, N. Snejko, M. Iglesias, B. Gómez-Lor, E. Gutiérrez-Puebla, and M. Á. Monge, ñLayered Rare-Earth Hydroxides: A Class of Pillared Crystalline Compounds for Intercalation Chemistry,ò *Angew. Chem. Int. Ed.*, **45** [47] 7998-8001 (2006).

[27]F. X. Geng, Y. Matsushita, R. Z. Ma, H. Xin, M. Tanaka, F. Izumi, N. Iyi, and T. Sasaki, ñGeneral Synthesis and Structural Evolution of a Layered Family of $Ln_8(OH)_{20}Cl_4{\cdot}nH_2O$ (Ln=Nd, Sm, Eu, Gd, Tb, Dy, Ho, Er, Tm, and Y),ò *J. Am. Chem. Soc.*, **130** [48] 16344-50 (2008).

[28]F. X. Geng, R. Z. Ma, and T. Sasaki, ñAnion-Exchangeable Layered Materials Based on Rare-Earth Phosphors: Unique Combination of Rare-Earth Host and Exchangeable Anions,ò *Acc. Chem. Res.*, **43** [9] 1177-85 (2010).

[29]F. X. Geng, Y. Matsushita, R. Z. Ma, H. Xin, M. Tanaka, N. Iyi, and T. Sasaki, ñSynthesis and Properties of Well-Crystallized Layered Rare-Earth Hydroxide Nitrates from Homogeneous Precipitation,ò *Inorg. Chem.*, **48** [14] 6724-30 (2009).

[30]Q. Zhu, J.-G. Li, C. Y. Zhi, X. D. Li, X. D. Sun, Y. Sakka, D. Golberg, and Y. Bando, ñLayered Rare-Earth Hydroxides (LRHs) of $(Y_{1-x}Eu_x)_2(OH)_5NO_3{\cdot}nH_2O$ (x = 0-1): Structural Variations by Eu^{3+} Doping, Phase Conversion to Oxides, and the Correlation of Photoluminescence Behaviors,ò *Chem. Mater.*, **22** [14] 4204-13 (2010).

[31]X. L. Wu, J.-G. Li, Q. Zhu, J. K. Li, R. Z. Ma, T. Sasaki, X. D. Li, X. D. Sun, and Y. Sakka, ñThe Effects of Gd^{3+} Substitution on the Crystal Structure, Site symmetry, and Photoluminescence of Y/Eu Layered Rare-Earth Hydroxide (LRH) Nanoplates,ò *Dalton Trans.*, **41** [6] 1854-61 (2012).

[32]X. J. Wang, J.-G. Li, Q. Zhu, X. D. Li, X. D. Sun, and Y. Sakka, ñFacile and Green Synthesis of $(La_{0.95}Eu_{0.05})_2O_2S$ Red Phosphors with Sulfate-Ion Pillared Layered Hydroxides as a New Type of Precursor: Controlled Hydrothermal Processing, Phase Evolution and Photoluminescence,ò *Sci. Technol. Adv. Mater.*, **15** [1] 014204 (2014).

[33]Y. S. Zhao, J.-G. Li, M. X. Guo, and X. J. Yang, ñStructure and Photoluminescent Investigation of LTbH/LEuH Nanosheets and their Color-Tunable Colloidal Hybrids,ò *J. Mater. Chem. C*, **1** [22] 3584-92 (2013).

[34]X. L. Wu, J.-G. Li, J. K. Li, Q. Zhu, X. D. Li, X. D. Sun, and Y. Sakka, ñLayered Rare-Earth Hydroxide and Oxide Nanoplates of the Y/Tb/Eu System: Phase-Controlled Processing, Structure Characterization and Color-Tunable Photoluminescence via Selective Excitation and Efficient Energy Transfer,ò *Sci. Technol. Adv. Mater.*, **14** [1] 015006 (2013).

[35]B. Lu, J.-G. Li, and Y. Sakka, ñControlled Processing of $(Gd,Ln)_2O_3$:Eu (Ln=Y, Lu) Red Phosphor Particles and Compositional Effects on Photoluminescence,ò *Sci. Technol. Adv. Mater.*, **14 [**6] 064202 (2013).

[36]L. F. Hu, R. Z. Ma, T. C. Ozawa, and T. Sasaki, ñOriented Monolayer Film of Gd_2O_3:0.05Eu Crystallites: Quasi-Topotactic Transformation of the Hydroxide Film and Drastic Enhabcement of Photoluminescence Properties,ò *Angew. Chem. Int. Ed.*, **48** [21] 3846-9 (2009).

[37]X. L. Wu, ñNitrate-Type Layered Rare-Earth Hydroxides: Controlled Synthesis, Interlayer Ion Exchange, Sructure Characterization, and Applications in Photoluminescence,ò Ph.D. Thesis, Northeastern University, October 2013. [thesis]

[38]X. L. Wu, J.-G. Li, Q. Zhu, W. G. Liu, J. Li, X. D. Li, X. D. Sun, and Y. Sakka, ñOne-Step Freezing Temperature Crystallization of Layered Rare-Earth Hydroxide ($Ln_2(OH)_5NO_3{\cdot}nH_2O$) Nanosheets For a Wide Spectrum of Ln (Ln=Pr-Er, and Y), Anion Exchange with Fluorine and Sulfate, and Microscopic Coordination Probed via Photoluminescence,ò *J. Mater. Chem. C*, **3** [14] 3428-37 (2015).

[39]J.-G. Li, X. D. Li, X. D. Sun, and T. Ishigaki, ñMonodispersed Colloidal Spheres for Uniform $Y_2O_3:Eu^{3+}$ Red-Phosphor Particles and Greatly Enhanced Luminescence by Simultaneous Gd^{3+} Doping,ò *J. Phys. Chem. C*, **112** [31] 11707-16 (2008).

[40]Y. Ganjkhanlou, M. Kazemzad, and F. A. Hessari, ñChromaticity Dependence on Eu Concentration in Y_2O_3:Eu Nanopowders,ò *Nano*, **5** [2] 111-6 (2010).

[41]W. H. Rhodes, ñAgglomerate and Particle Size Effects on Sintering Yttria-Stabilized Zirconia,ò *J. Am. Ceram. Soc.*, **64** [1] 19-22 (1981).

[42]M. G. S. Murray, J. Wang, C. B. Ponton, and P. M. Marquis, ñAn Improvement in Processing of Hydroxyapatite Ceramics,ò *J. Mater. Sci.*, **30** [12] 3061-74 (1995).

[43]F. F. Lange, ñSinterability of Agglomerated Powders,ò *J. Am. Ceram. Soc.*, **67** [2] 83-9 (1984).

[44]G. Achutaramayya and W. Scott, ñMeasurement of Dihedral Angles by Scanning Electro Microscopy,ò *J. Am. Ceram. Soc.*, **56** [4] 230-1 (1973).

[45]T. Ikegami, K. Kotani, and K. Eguchi, ñSome Roles of MgO and TiO_2 in Densification of a Sinterable Alumina,ò *J. Am. Ceram. Soc.*, **70** [12] 885-90 (1987).

[46]Y. Nigara, ñMeasurement of the Optical Constants of Yttrium Oxide,ò *Jpn. J. Appl. Phys.*, **7** [4] 404-8 (1968).

[47]A. Konrad, T. Fries, A. Gahn, F. Kummer, U. Herr, R. Tidecks, and S. Samwer, ñChemical Vapor Synthesis and Luminescence Properties of Nanocrystalline Cubic Y_2O_3:Eu,ò *J. Appl. Phys.*, **86** [6] 3129-33 (1999).

[48]M. L. Jia, J. H. Zhang, S. Z. Lu, J. T. Sun, Y. S. Luo, X. R. Ren, H. W. Song, and X. J. Wang, ñUV Excitation Properties of Eu^{3+} at the S_6 Site in Bulk and Nanocrystalline Cubic Y_2O_3,ò *Chem. Phys. Lett.*, **384** [1-3] 193-6 (2004).

[49]G. Concas, G. Spano, E. Zych, and J. Trojan-Piegza, ñNano- and Microcrystalline Lu_2O_3:Eu Phosphors: Variations in Occupancy of C_2 and S_6 Sites by Eu^{3+} Ions,ò *J. Phys.: Condens. Matter*, **17** [17] 2594-604 (2005).

[50]J. Heber, K. H. Hellwege, U. Kobler, and H. Murmann, ñEnergy Levels and Interaction Between Eu^{3+}-Ions at Lattice Sites of Symmetry C_2 and Symmetry C_{3i} in Y_2O_3,ò *Z. Physik*, **237** [3] 189-204 (1970).

[51]H. Retot, S. Blahuta, A. Bessiere, B. Viana, B. LaCourse, and E. Mattmann, ñImproved Scintillation Time Response in $(Lu_{0.5}Gd_{0.5})_2O_3:Eu^{3+}$ Compared with $Lu_2O_3:Eu^{3+}$ Transparent Ceramics,ò *J. Phys. D: Appl. Phys.*, **44** [23] 235101 (2011).

[52]H. Huang, G.-Q. Xu, W. S. Chin, L. M. Gan, and C. H. Chew, ñSynthesis and Characterization of Eu:Y_2O_3 Nanoparticles,ò *Nanotechnology*, **13** [3] 318-23 (2002).

[53]S. Y. Zeng, K. B. Tang, T. W. Li, and Z. H. Liang, ñ3D Flower-Like $Y_2O_3:Eu^{3+}$ Nanostructures: Template-Free Synthesis and its Luminescence Properties,ò *J. Colloid Interface Sci.*, **316** [2] 921-9 (2007).

[54]P. Packiyaraj and P. Thangadurai, ñStructural and Photoluminescence Studies of Eu^{3+} Doped Cubic Y_2O_3 Nanophosphors,ò *J. Lumin.*, **145** 997-1003 (2014).

[55]Q. W. Chen, Y. Shi, L. Q. An, J. Y. Chen, and J. L. Shi, ñFabrication and Photoluminescence Characteristics of Eu^{3+}-Doped Lu_2O_3 Transparent Ceramics,ò *J. Am. Ceram. Soc.*, **89** [6] 2038-42 (2006).

Chapter Ⅳ

Effects of Gd substitution on sintering and optical properties of highly transparent $(Y,Gd)_2O_3$:Eu ceramics

- **Fabrication of highly transparent $(Y,Gd)_2O_3$:Eu ceramics**
  - **Effects of Gd^{3+} incorporation on particle properties**
    - **Impacts of Gd^{3+} doping on ceramic sintering**
  - **Influences of Gd^{3+} addition on optical performances**

4.1 Introduction

Cubic C-type rare-earth oxides with the formula of RE_2O_3 (RE=Eu-Lu, as well as Y and Sc) having 80 atoms per unit cell may be densified into transparent ceramics for potential application in various optical and thermodynamic systems.[1-5] By properly doping with activator into host material and employing advanced processing techniques, polycrystalline transparent ceramic scintillators better than conventional single-crystals may be acquired. The materials can absorb and convert x-rays into visible light to be applied in x-ray medical diagnosis systems such as computed tomography and stationary digital imaging. Transparent $Y_{1.34}Gd_{0.6}Eu_{0.06}O_3$ ceramic as the first commercialized polycrystalline scintillator is being used in medical x-ray detectors.[6] Y_2O_3 is an attractive host material due to its low cost, high dielectric constant (14-18), large band gap (5.6 eV), high melting point (2430 °C), high thermal conductivity (13.6 W/mK), refractive index (n_H=1.93 at λ=613 nm), high thermal stability, low phonon energy (380 cm^{-1}), and good resistance to erosion and thermal shock.[7-9] In order to achieve high-quality imaging and alleviate x-ray radiation hazards to patientsô bodies, a high-efficiency scintillator should have a high absorption coefficient for x-rays, high transparency, short decay time, high light output and low radiation damage.[10] As the relationship among the absorption coefficient (η_{abs}), theoretical density (ρ), and effective atomic number (Z_{eff}) can be expressed as $\eta_{abs}=\rho Z_{eff}^4$,[11,12] a high theoretical density and atomic number are thus essential for a scintillator. The small difference in ionic radius between Y^{3+} and Gd^{3+} makes it possible to form a continuous solid solution (YGO, space group: *Ia*3) that is not only cost-effective but also has a high theoretical density and a high atomic number for Gd. Moreover, Gd^{3+} can readily sensitize the $^5D_0$Ÿ $^7F_2$ red emission of Eu^{3+} to achieve relatively strong light emission.[13,14] The combination of these excellent properties of YGO:Eu solid solutions has attracted our interest and a series of investigations have been carried out.

Recently, several kinds of compositions of YGO:Eu ceramics have been produced by hot pressing, hot isostatic pressing and pressureless sintering.[6,15-17] It is, however, still difficult to achieve high transparency in the visible-light region and also lacks study in the following aspects: (1) what is the role of Gd^{3+} in YGO:Eu ceramic sintering? (2) how does Gd^{3+} doping affect the optical properties of the ceramics. In this chapter, we address these issues via a systematic investigation?

Along with the advances in particle processing, sinterable powders for producing transparent ceramics have been synthesized by wet-chemical routes.[18-22] Anion-exchangeable layered rare-earth hydroxide (LRH), as a relatively new type of two-dimensional nanomaterial,[23-27] has been proved to be an excellent precursor for yielding highly sinterable oxide powders of the binary Y-Eu system based on our research in Chapter z . In the present study, highly transparent $(Y_{0.95-x}Gd_xEu_{0.05})_2O_3$ (x=0.15-0.65) ceramics were successfully fabricated using LRH nanosheets as the precursor via vacuum sintering, and the simultaneous effects of Gd^{3+} substitution on the particle properties, sintering kinetics and optical performances of the materials were studied.

4.2 Experimental procedure

4.2.1 Powder synthesis and characterization

The starting materials were $Y(NO_3)_3{\cdot}6H_2O$ (>99.99% pure, Kanto Chemical Co., Tokyo, Japan), $Gd(NO_3)_3{\cdot}6H_2O$ (>99.99% pure, Kanto Chemical) and $Eu(NO_3)_3{\cdot}6H_2O$ (>99.95% pure, Kanto Chemical).

In a typical synthetic procedure, an x value of 0.15 to 0.65 was selected for the $(Y_{0.95-x}Gd_xEu_{0.05})_2O_3$ precursor with the Eu^{3+} content fixed at 5 at.%, because the optimal Eu^{3+} contents were reported to be ~5 at.% for Y_2O_3:Eu[14,28] and 5-7 at.% for Gd_2O_3:Eu.[29-32] A precipitation precursor was produced at a freezing

temperature of 4 °C by the dropwise addition of ammonia solution (1 M, ultrahigh purity, Kanto Chemical) at a rate of ~3 mL/min into 0.075 M of mixed nitrate solution under mild stirring. After aging for 1.5 h, the resultant suspension was filtered and repeatedly washed with distilled water and then dispersed in ammonium sulfate solution with a SO_4^{2-}/total cation molar ratio (R) of 0.03 for anionic exchange. After reaction for 2 h, the product was recovered via suction filtration, rinsed with distilled water and anhydrous alcohol, followed by drying at 80 °C. The procedure for the synthesis of the Y-Eu binary-system LRH precursor can be found in Chapter z in detail. The dried precursor was calcined in a tube furnace under flowing oxygen gas (300 mL/min) at 1100 °C for 4 h to produce oxide powders, with a heating rate of 5 °C/min in the ramp stage.

The precursors and calcination products were characterized by Brunauerï Emmettï Teller analysis (BET; Model Autosorb-iQ, Quantachrome Instruments, Boynton Beach, Florida, USA), x-ray diffractometry (XRD; Model RINT2200, Rigaku, Tokyo, Japan), field-emission scanning electron microscopy (FE-SEM; Model S-5000, Hitachi, Tokyo), transmission electron microscopy (TEM; Model JEM-2000FX, JEOL, Tokyo), laser diffraction particle size analysis (LDPSA, Model LA-920, Horiba, Kyoto, Japan), UV-vis absorption spectroscopy (Model V-560, JASCO) and fluorescence spectroscopy (Model FP-6500, JASCO, Tokyo).

4.2.2 Compaction, sintering, and characterization of transparent ceramics

The $(Y_{0.95-x}Gd_xEu_{0.05})_2O_3$ oxide particles were cold isostatically pressed under ~320 MPa into green bodies, and their densification kinetics was investigated using two different dilatometers, that is, the Model 402 E/7 equipment (Netzsch, Selb, Germany) for constant rate of heating up to 1650 °C and the Model DIL 402 C one (Netzsch) for isothermal sintering in the temperature range of 1150-1250 °C for 2 h. Both the types of sintering were performed under flowing argon gas protection and with constant heating and cooling rates of 10 and 20 °C/min, respectively.

Vacuum sintering was performed in a W-heater furnace at 1625-1700 °C for 4 h under a pressure of less than 10^{-4} Pa. The heating rate used for the ramp stage was 8 °C/min up to 1100 °C and 1 °C/min from 1100 °C to the final sintering temperature. The densities of the sintered bodies were determined by the Archimedes method.

The sintered ceramics were double-side polished to a thickness of ~1 mm to measure the in-line transmittance on a UV/VIS/NIR spectrophotometer (Model SolidSpec-3700DUV, Shimadzu, Kyoto) over the wavelength range of 200-2000 nm.

Mirror-polished specimens were thermally etched at 1450 °C for 2 h in an oxygen atmosphere to observe their microstructures by FE-SEM (Model JSM-6500F, JEOL). Statistical grain sizes of the ceramics were derived from at least 200 grains using the WinRoof image analysis software.

4.3 Results and discussion

4.3.1 Effects of Gd^{3+} incorporation on particle properties

Figure 4.1a shows the XRD patterns of the as-synthesized $(Y_{0.95-x}Gd_xEu_{0.05})_2O_3$ (x=0.15-0.75) precursors. A series of 00l and sharp 220 diffractions are observed to be characteristic of the $Ln_2(OH)_5NO_3{\cdot}nH_2O$ layered compounds.[33] The 002 and 004 reflections clearly shift towards the high-angle side and the c constant decreases at a higher Gd^{3+} concentration, indicating that Gd^{3+} addition leads to a contracted lattice dimension in the c-direction. The 220 diffractions shift to the low angle side with

increasing Gd^{3+} incorporation, suggesting that Gd^{3+} incorporation induces an expansion in the hydroxide host layer owing to its larger ionic radius than Y^{3+} (for 8-fold coordination, 0.1019 nm for Y^{3+} and 0.1053 nm for Gd^{3+}).[34] The interlayer distance (*c*/2) also shrinks with increasing *x* value, which can be explained as follows. The nitrate anion (sp^2 hybridization) is a triangle plane and its spatial orientation in the interlayer (parallel or vertical) determines the interlayer distance. The expansion of the *ab* plane would cause decreasing charge density of the hydroxide layer, in favour of a parallel posture of NO_3^- in the interlayer gallery, leading to a lattice contraction along the *c*-axis.

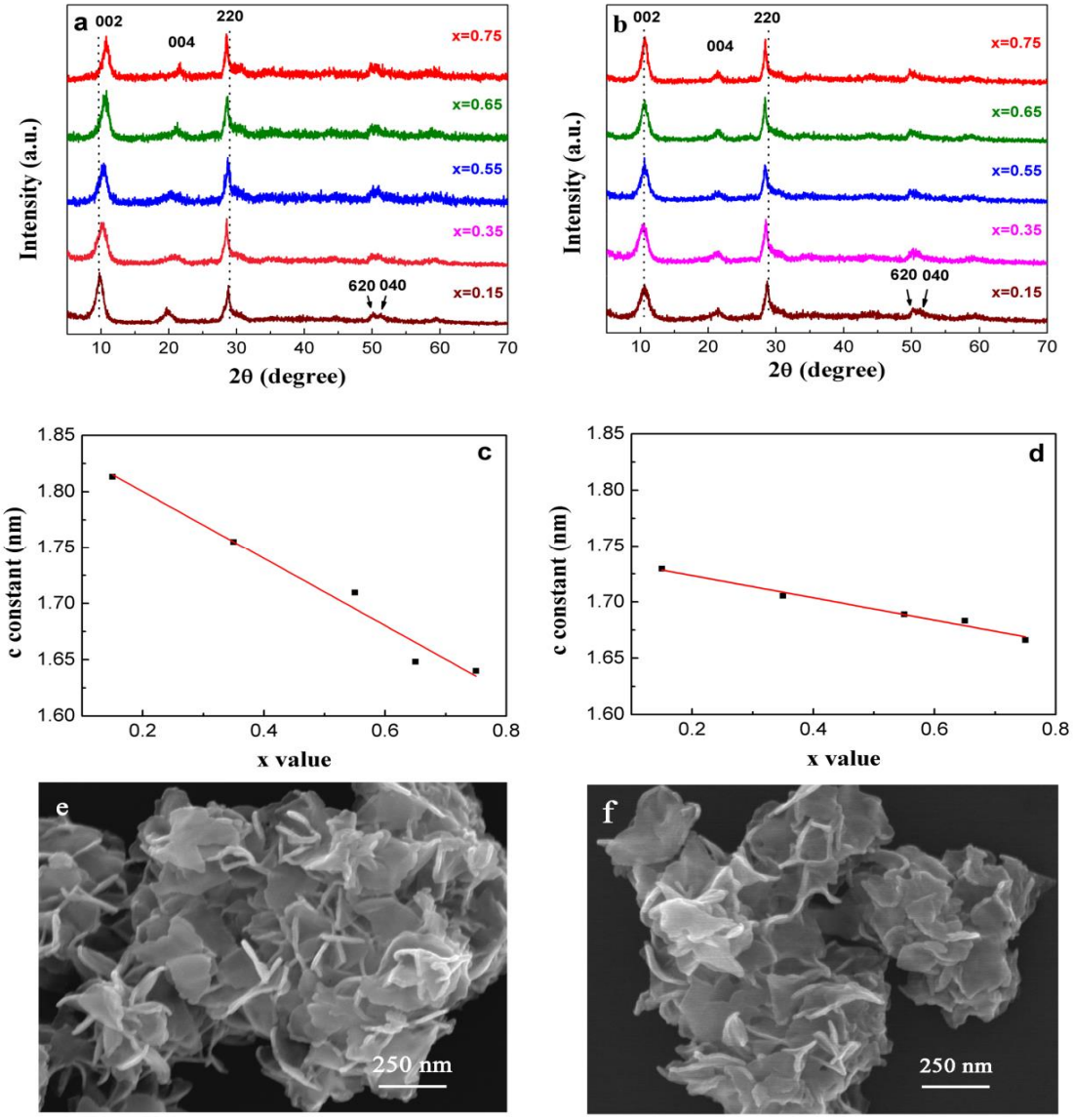

Fig. 4.1 (a) and (b) are the XRD patterns and (c) and (d) are the *c* constants of the as-synthesized $(Y_{0.95-x}Gd_xEu_{0.05})_2O_3$ (*x*=0.15-0.75) precursors before and after anion exchange with sulfate at *R*=0.03. (e) and (f) are the FE-SEM morphologies of the *x*=0.35 precursor and sulfate-exchange product, respectively.

Sulfate exchange at *R*=0.03 also changes cell dimension of the LRH crystal. The 002 and 004 diffractions of the exchange product only slightly move to the high-angle side with increasing Gd^{3+} content (Fig. 4.1b). Compared with the nitrate-type LRHs, the interlayer distances shrink for the *x*=0.15-0.55 compounds but expand for the *x*=0.65-0.75 ones (Figs. 4.1c and d). The geometry of sulfate anion is a

tetrahedron that owns larger space dimension than that of the nitrate, leading to an expansion along the *c* axis for the LRHs having small interlayer distance. On the other hand, the hydrogen bonding between the sulfate and the water molecules/hydroxyls in the hydroxide main layer would cause a contraction along the *c* axis for the LRHs possessing large interlayer distance. In summary, the interlayer distance is determined by the geometry/posture of the anions in the interlayer gallery, the charge density of the hydroxide main layer, and the electrostatic attraction/hydrogen bonding between the interlayer anions and the hydroxide host layer. It is also seen that sulfate-exchange does not bring about appreciable morphology change to the LRH of Y-Gd-Eu ternary system (Figs. 4.1e, f).

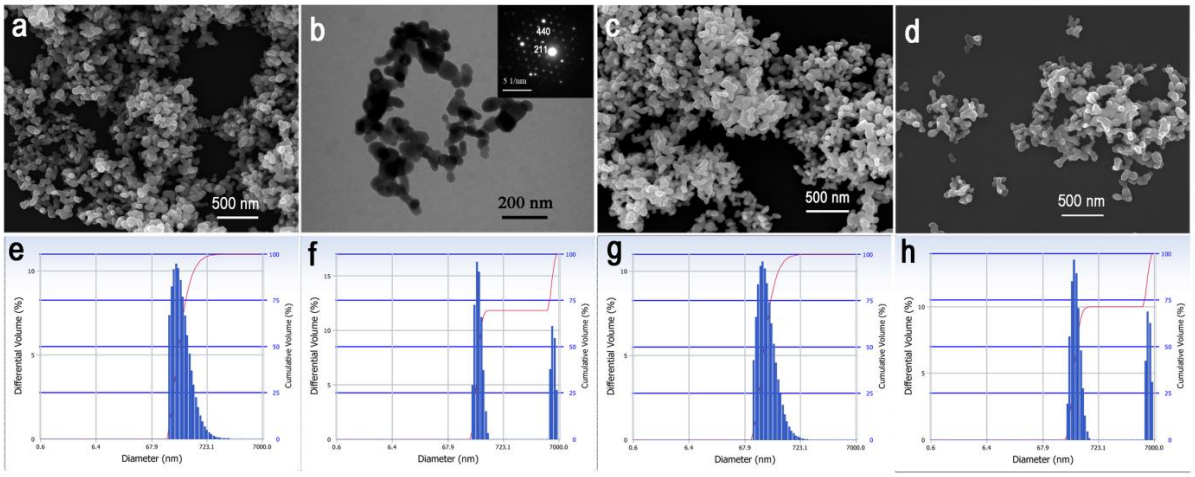

Fig. 4.2 FE-SEM (a, c and d) and TEM (b) images of the $(Y_{0.95-x}Gd_xEu_{0.05})_2O_3$ oxide powders for x=0.15 (a), 0.35 (b), 0.55 (c) and 0.65 (d), followed by their particle size distributions in cumulative volume obtained by LDPSA (e)-(h). The inset in panel (b) is the SAED pattern of x=0.35 sample.

Calcining the anion-exchanged LRH nanosheets produced generally well-dispersed and rounded $(Y_{0.95-x}Gd_xEu_{0.05})_2O_3$ oxide powders at 1100 °C (Fig. 4.2). LDPSA in volume distribution has been found to be effective in detecting hard agglomeration.[35] The results show that the x=0.15 and 0.55 particles possess unimodal particle-size distribution and average particle sizes of ~269 and 188 nm, respectively (Figs. 4.2e and g). The x=0.35 and 0.65 powders, although bimodal in size distribution, have substantially more uniform particles for their fine portions (~70 vol.%), with average sizes of ~251 and 276 nm, respectively (Figs. 4.2f and h). The coarse parts of these two powders (~30 vol.%) have similar average sizes of ~6 ε m. Such powders are significantly finer and less-aggregated than the commercially available ones produced by oxalate precipitation, and would be beneficial for achieving uniform densification to yield ceramics with finer grains at a relatively low densification temperature.[36,37] The BET analysis revealed specific areas of ~16.1, 15.8, 13.6 and 10.5 m^2/g for the powders with x=0.15, 0.35, 0.55 and 0.65, respectively. The corresponding particle sizes were estimated to be ~72, 62, 66 and 79 nm, assuming that the particles are ideal solid spheres with smooth surfaces and by applying the equation $D_{BET}=6000/(d_{th}\times S_{BET})$, where d_{th} is the theoretical density, which is given elsewhere,[13] S_{BET} is the specific surface area (m^2/g) and D_{BET} is the average particle size (nm). Excluding the W-coating effect (~20 nm of particle growth by W sputtering for electrical conduction), the average particle sizes obtained from FE-FEM images were ~68, 64, 60 and 59 nm for x=0.15, 0.35, 0.55 and 0.65, respectively. The selected area electron diffraction (SAED) pattern exhibits well-defined diffraction spots (in the inset of Fig. 4.2b), implying that the observed object (one particle) is a well-crystallized single crystal. The crystallite sizes determined from Scherrer equation were ~65, 65, 56 and

50 nm for x=0.15, 0.35, 0.55 and 0.65, respectively, which are similar to the particle sizes obtained by SEM and are also consistent with the SAED result. A slight decrease in the crystallite/particle size was observed with increasing Gd^{3+} incorporation, mainly in that the Gd^{3+} has higher alkalinity than the Y^{3+} to induce a higher thermal decomposition temperature of the precursor and hence retarded crystallite/particle growth.

4.3.2 Impacts of Gd^{3+} doping on ceramic sintering kinetics

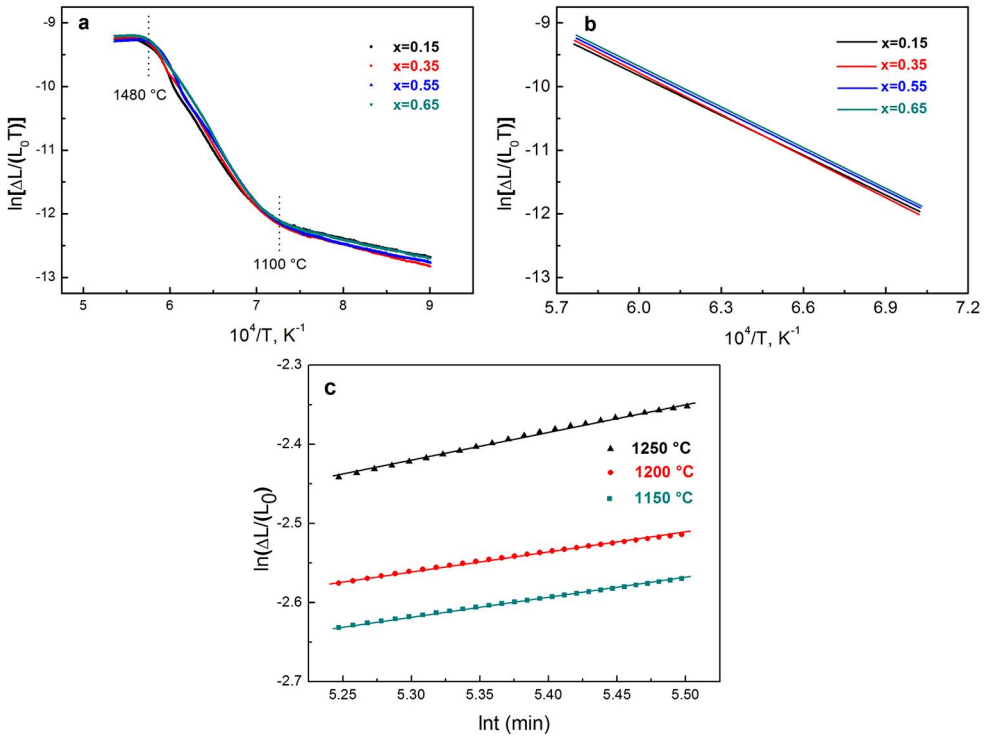

Fig. 4.3 Plots of ln(φL/L_0T) vs 1/T obtained from densification behaviors of the $(Y_{0.95-x}Gd_xEu_{0.05})_2O_3$ (x=0.15-0.65) solid solutions with a constant heating rate of 10 °C/min (a), fitting of ln(φL/L_0T) against 1/T at ~1100-1480 °C (b) and plots of ln(φL/L_0) vs ln$t$ in the temperature range of 1150-1250 °C for the x=0.35 specimen under isothermal conditions (c).

Under a constant rate of heating, Young et al.[38] derived the following sintering rate equation:

$$d(\Delta L/L_0)/dT \approx \begin{cases} \left(\frac{2.14\gamma\Omega D_{0B}RT}{ka^4cQ}\right)^{1/3}\left(\frac{Q}{3RT^2}\right)\exp\left(\frac{-Q}{3RT}\right) \\ \textit{grain boundary diffusion} \\ \left(\frac{5.34\gamma\Omega D_{0v}RT}{ka^3cQ}\right)^{1/2}\left(\frac{Q}{2RT^2}\right)\exp\left(\frac{-Q}{2RT}\right) \\ \textit{volume diffusion} \end{cases} \quad (4.1)$$

where φL is the change in length of the specimen, L_0 is the initial length of the sample, γ is the surface energy, Ω is the vacancy volume, D_{0B} is the grain boundary diffusion coefficient, c is the heating rate, R is the gas constant, T is the absolute temperature, Q is the activation energy and D_{0v} is the volume diffusion coefficient.

As deduced from equation 4.1, a plot of ln[Td(φL/L_0)/dT] or ln(φL/L_0T) versus 1/T will exhibit a single slope if a single diffusion mechanism dominates, and the activation energy can be calculated from the slope, -nQ/R, where n=3 for grain boundary diffusion and n=2 for volume diffusion.[38] The deviation from linearity

below 1100 °C may be ascribed to surface diffusion with a low activation energy (Fig. 4.3a), by which particles form sintering necks via the driving force of the curvature gradient. In the temperature range of 1100-1480 °C, fitting yielded four similar slopes for the $(Y_{0.95-x}Gd_xEu_{0.05})_2O_3$ (x=0.15-0.65) solid solutions (Fig. 4.3b), implying similar diffusion mechanisms.

Under isothermal conditions, the following relationship between the shrinkage ($\varphi L/L_0$) and the holding time (t) has been given by Johnson et al.:[39]

$$\frac{\Delta L}{L_0} = \left(\frac{K\gamma\Omega D}{kTr^p}\right)^m t^m \qquad (4.2)$$

where φL is the change in length of the compact, L_0 is the initial length of the sample, K, p and m are numerical constants, γ is the surface energy, Ω is the vacancy volume, D is the self-diffusion coefficient, t is the time, k is the Boltzmann constant, T is the absolute temperature and r is the particle radius. Equation (4.2) indicates that the plot of $\ln(\varphi L/L_0)$ against $\ln t$ should be a straight line, and thus the diffusion mechanism can be determined by the slope (m) of the line; that is, for spherical particle contacts, m=0.31 for grain boundary diffusion and m=0.46 for volume diffusion.[39] The plot of $\ln(\varphi L/L_0)$ versus $\ln t$ for the x=0.35 specimen yields three straight lines between 1150 and 1250 °C (Fig. 4.3c). The slopes of the three lines were found to be close to 0.31, indicating that the sintering mechanism was dominated by grain boundary diffusion. Applying equation (4.1) yielded grain-boundary-diffusion controlled activation energies of 225±2, 228±1, 227±2 and 229±1 kJ/mol for x=0.15, 0.35, 0.55 and 0.65, respectively, and hence Gd^{3+} doping does not play an important role in determining activation energy. There have been few reports on the activation energy of YGO:Eu materials for comparison. Chen et al.[40] calculated the activation energy of a $(Y_{0.99}Gd_{0.01})_2O_3$ ceramic to be 337 kJ/mol via the grain growth method. In this study, the activation energies are much lower than this value, which may be attributable to the combined effects of a larger grain boundary area, a more uniform microstructure and the Eu^{3+} dopant.

As the sintering temperature increases, grain boundary diffusion is predicted to become less efficient than volume diffusion owing to the higher activation energy of the latter,[41] by which the deviation from linearity was observed at temperatures higher than 1480 °C as shown in Fig. 4.3a.

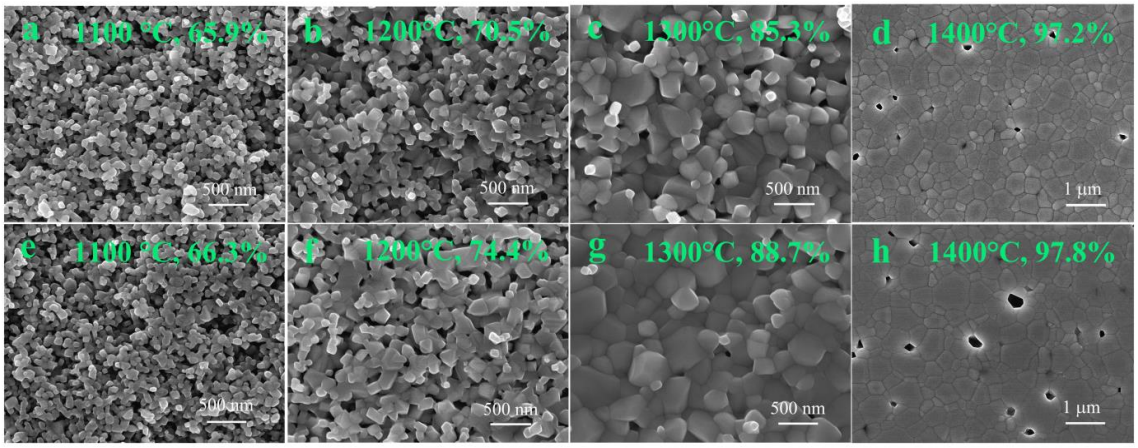

Fig. 4.4 FE-SEM micrographs showing microstructures of the $(Y_{0.8}Gd_{0.15}Eu_{0.05})_2O_3$ (a)-(d) and $(Y_{0.6}Gd_{0.35}Eu_{0.05})_2O_3$ (e)-(h) bodies vacuum-sintered at 1100-1400 °C.

Figure 4.4 compares the microstructures of the $(Y_{0.8}Gd_{0.15}Eu_{0.05})_2O_3$ and $(Y_{0.6}Gd_{0.35}Eu_{0.05})_2O_3$ bodies vacuum-sintered at 1100-1400 °C for 4 h, with the relative densities also indicated in the figure. The

densities of the two compacts increase with the elevated sintering temperature. At the initial sintering temperature of 1100 °C, the particles form necks and the shape of the pores is irregular (Figs. 4.4a and e). In the temperature range of 1200-1300 °C, the sintering necks grow and the pores transform into arrays of interconnected cylinder-like channels, which are characteristics of intermediate-stage sintering (Figs. 4.4b, c, f and g). At 1400 °C and above, their relative densities are over 97% and the pores become isolated and rounded, suggesting the start of the final sintering stage (Figs. 4.4d and h). Moreover, the x=0.35 sintered body has a larger grain size and higher density than the x=0.15 sample under identical sintering conditions, since the addition of more Gd^{3+} leads to lattice distortion and further promotes the grain boundary mobility according to a previous report.[40] The ceramics with x=0.15 and 0.35 sintered at the quite low temperature of 1400 °C already had their high densities of ~97.2 and 97.8% and average grain sizes of ~380 nm and 510 nm, respectively. The residual pores were mostly located on grain boundaries, which may be readily removed at a higher sintering temperature.

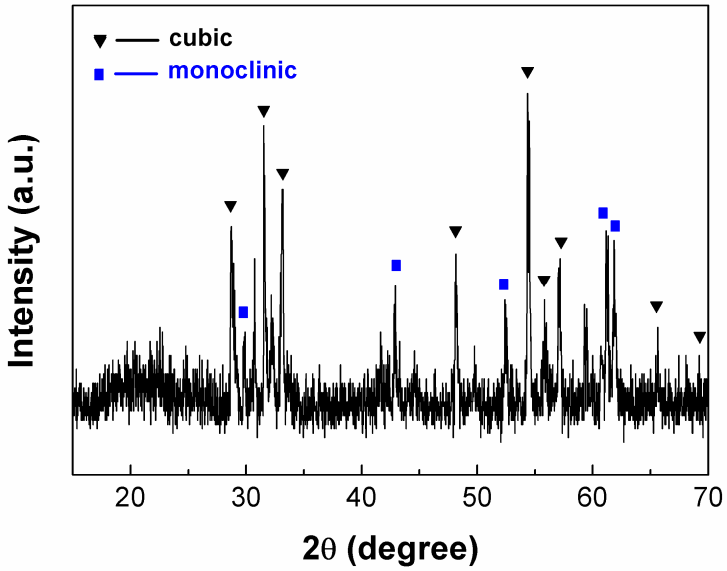

Fig. 4.5 XRD pattern of the $(Y_{0.3}Gd_{0.65}Eu_{0.05})_2O_3$ ceramic sintering at 1650 °C.

The Y_2O_3-Gd_2O_3 phase diagram (Appendix Fig. 2) revealed that the phase transformation for a solid solution with 70 (mol%) Gd^{3+} content will occur at approximate temperature of 1720 °C. That is, a mixed phase may be produced in the temperature range of 1720-1765 °C, while a pure monoclinic phase would be formed at 1765-2200 °C.[42] A higher phase transformation temperature at a lower Gd^{3+} content can be achieved (e.g., 1885 °C for 60% Gd^{3+}). Under a high vacuum condition, however, the phase transformation temperatures tend to be much lower than the reported values. For example, the x=0.65 specimen already underwent a phase transformation from a cubic phase to a mixed phase (cubic plus monoclinic) with low crystallinity at the sintering temperature of 1650 °C (Fig. 4.5), as a result of which the ceramic became opaque. And hence, the temperature for vacuum sintering was selected to be 1625 °C for the specimen with x=0.65 and 1700 °C for the others with x=0.15-0.55.

Figure 4.6 shows microstructures and fracture surfaces of the final $(Y_{0.95-x}Gd_xEu_{0.05})_2O_3$ (x=0.15-0.65) ceramics. Pore-free ceramics of uniform grain sizes were obtained for the specimens with x=0.15-0.55 owing to the further elimination of residual pores. The pores are occasionally found for the x=0.65 sample and thus followed by a relatively low transparency (Fig. 4.6). The average grain sizes were observed to be ~15 μm, 27

μm, 35 μm and 11 μm for the ceramics with x=0.15, 0.35, 0.55 and 0.65, respectively. An increase in Gd^{3+} addition of 40% from 15 to 55% promotes the grain-size growth by ~20 μm under identical sintering condition. As observed from the fracture surfaces, the densified ceramics are mainly intragranularly fractured and pores along the grain boundaries are also difficult to be detected. The relative densities of the four ceramics made in the present work are all close to 100%.

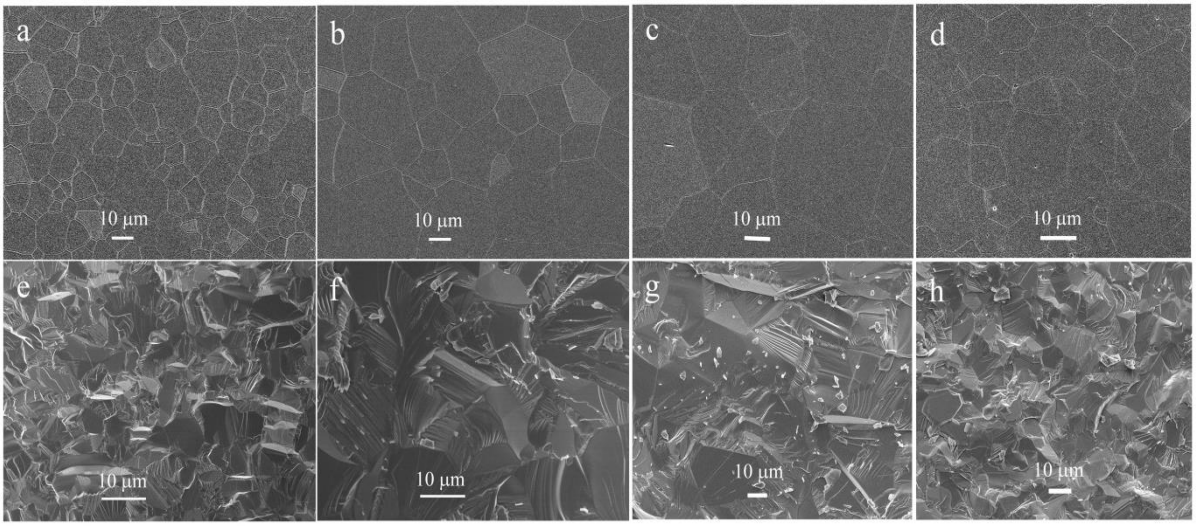

Fig. 4.6. FE-SEM micrographs of the polished surfaces of $(Y_{0.95-x}Gd_xEu_{0.05})_2O_3$ ceramics sintered at 1700 °C (x=0.15 (a), 0.35 (b) and 0.55 (c)) and 1625 °C (x=0.65 (d)), and their respective fracture surfaces (e)-(h). These microstructures of the $(Y_{0.95-x}Gd_xEu_{0.05})_2O_3$ ceramics correspond to the sintered specimens shown in Fig. 4.7.

4.3.3 Effects of Gd^{3+} addition on optical properties

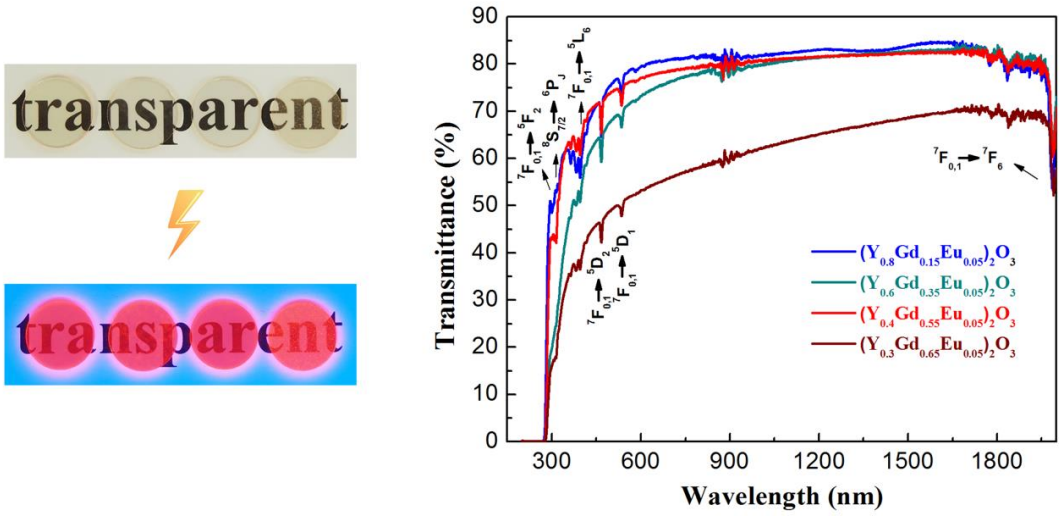

Fig. 4.7 Appearances (left panel, digital images) and in-line transmittances (right panel) of the transparent $(Y_{0.95-x}Gd_xEu_{0.05})_2O_3$ (x=0.15-0.65) ceramics. All the samples were vacuum sintered at 1700 °C for 4 h. The denotation keys in the right panel correspond to the four ceramics (from left to right) exhibited in the left panel. The lower part of the left panel shows the observed red emission of Eu^{3+} under excitation from a 254 nm UV lamp. The four samples all have a thickness of 1 mm.

The appearances and in-line transmittances of the $(Y_{0.95-x}Gd_xEu_{0.05})_2O_3$ (x=0.15-0.65) ceramics are

shown in Fig. 4.7. The four specimens display high transparency to the naked eye. Upon UV irradiation at 254 nm, all the transparent bodies exhibit strong red emissions that correspond to the $^5D_0 \rightarrow {}^7F_{1,2}$ transitions of Eu^{3+} (Fig. 4.7, lower part of left panel). The absorption bands indicated on the transmittance curves correspond to the intra-$4f^6$ transitions of Eu^{3+}, together with those at 308 and 314 nm for the $^8S_{7/2} \rightarrow {}^6P_J$ transition of Gd^{3+}.

The theoretical transmittance (T) of a defect-free single crystal can be calculated from the following two equations of

$$T = (1-R)^2 \exp(-\alpha t) \qquad (4.3)$$

$$R = \frac{(n-1)^2}{(n+1)^2} \qquad (4.4)$$

where t is the sample thickness, α is the loss factor and n is the refractive index.

The refractive index of $(Y_{0.95-x}Gd_xEu_{0.05})_2O_3$ single crystal has not been reported elsewhere. Even so, the n value for $Y_{1.34}Gd_{0.6}Eu_{0.06}O_3$ single crystal is 1.96 at a wavelength of ~613 nm,[10] and therefore the transparency of the $Y_{1.34}Gd_{0.6}Eu_{0.06}O_3$ single crystal is calculated to be ~80.1%, assuming α=0. The $(Y_{0.95-x}Gd_xEu_{0.05})_2O_3$ ceramics made in the present work have in-line transmittances of 79.5, 73.6, 77.1 and 53.4% for x=0.15, 0.35, 0.55 and 0.65 at the Eu^{3+} emission wavelength of 613 nm, which are ~99.3, 91.9, 96.3 and 66.7% of the theoretical value of $Y_{1.34}Gd_{0.6}Eu_{0.06}O_3$ single crystal, respectively. Our samples with x=0.15-0.55 thus possess much higher transmittances than the commercial $Y_{1.34}Gd_{0.6}Eu_{0.06}O_3$ ceramic scintillator (72.8% at 610 nm).[6]

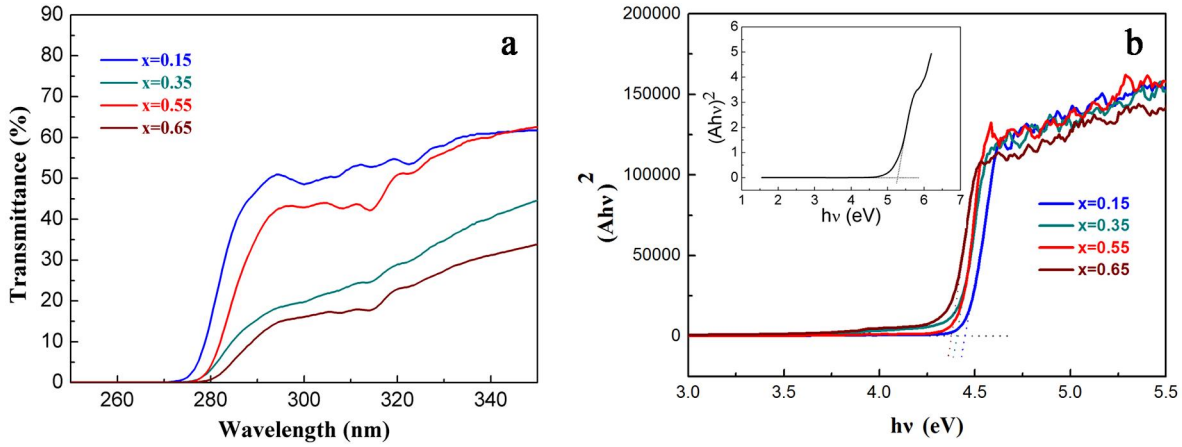

Fig. 4.8 Enlargement of in-line transmittance curves in Fig. 4.7 for wavelengths from 250 to 350 nm (a) and plots of hv vs $(Ahv)^2$ obtained from the in-line transmittance curves of the ceramics (b). The inset in Fig. 4.8b is a plot of hv vs $(Ahv)^2$ for the $(Y_{0.6}Gd_{0.35}Eu_{0.05})_2O_3$ powder sample obtained from its UV-vis absorption spectra.

The in-line transmittances of the $(Y_{0.95-x}Gd_xEu_{0.05})_2O_3$ ceramics start at different wavelengths, which can be appreciably observed from the enlarged transmittance curves shown in Fig. 4.8a. Increased Gd^{3+} addition induces a redshift of the starting wavelength, corresponding to a change in the bandgap energy.

The bandgap energy can be calculated from transmittance curve by the following two equations: [43]

$$\alpha = \frac{1}{d}\ln\left(\frac{1}{T}\right) \qquad (4.5)$$

$$\alpha h\nu = B(h\nu - E_g)^{1/2} \qquad (4.6)$$

where α is the absorption coeffient, d is the sample thickness, T is the transmittances, $h\nu$ is the incident photon energy, B is the absorption constant and E_g is the bandgap energy.

The plot of $(Ah\nu)^2$ against $h\nu$ is shown in Fig. 4.8b, from which the bandgap energy can be estimated by extrapolating the linear part of the curve to the x-axis (y=0). The bandgap energies of the ceramics were thus found to decrease in the order $(Y_{0.3}Gd_{0.65}Eu_{0.05})_2O_3$ (~4.38 eV) < $(Y_{0.4}Gd_{0.55}Eu_{0.05})_2O_3$ ≈ $(Y_{0.6}Gd_{0.35}Eu_{0.05})_2O_3$ (~4.43 eV) < $(Y_{0.8}Gd_{0.15}Eu_{0.05})_2O_3$ (~4.47 eV), owing to increasing content of less electronegative Gd^{3+}. The bandgap energy of the ceramic is much lower than that of the corresponding powder (~5.28 eV, inset of Fig. 4.8b), as shown with the composition $(Y_{0.6}Gd_{0.35}Eu_{0.05})_2O_3$ for example. This trend is in general agreement with a previous report,[44] and is attributable to a decrease of the centroid of the 5*d* orbital of RE^{3+} along with crystallite/grain growth.

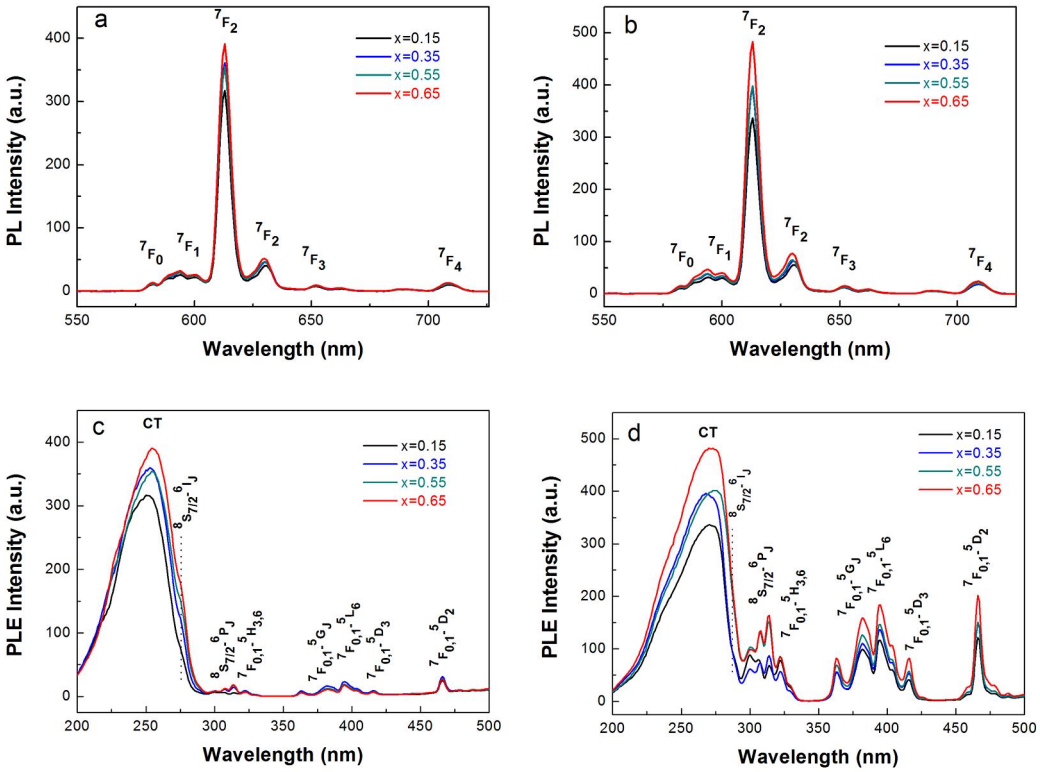

Fig. 4.9 PL/PLE behaviors of the $(Y_{0.95-x}Gd_xEu_{0.05})_2O_3$ powders (a, c) and ceramics (b, d). The PL spectra (a, b) were obtained under excitation with the peak wavelengths of the CT bands, while the PLE spectra (c, d) were acquired by monitoring the 613 nm emission of Eu^{3+}.

Figure 4.9 shows the photoluminescence (PL) and photoluminescence excitation (PLE) spectra of the $(Y_{0.95-x}Gd_xEu_{0.05})_2O_3$ (x=0.15-0.65) powders and ceramics. Both the two types of materials exhibit the typical red emissions of Eu^{3+}corresponding to its $^5D_0$Ÿ ^7F_J (J=0, 1, 2, 3, 4) transitions, with the strongest emission peak located at the wavelength of ~613 nm. The PLE spectrum obtained by monitoring the 613 nm emission is composed of a strong charge-transfer (CT band), arising from the electron transition from the 2*p* orbital of O^{2-} to the 4*f* orbital of Eu^{3+}, and weaker $^8S_{7/2}$Ÿ ^6P_J transitions of Gd^{3+} and the intra-4f^6 transitions of Eu^{3+},[13] as labeled in the figure in each case. The peaks at ~276 nm for the powders and ~287 nm for the ceramics, forming the right shoulder of the broad CT bands, are associated with the $^8S_{7/2}$Ÿ ^6I_J transition of Gd^{3+}.[43] A

clear redshift of the CT center of ~18 nm from the powder form to the bulk material can be observed, since the latter has a larger grain size and a smaller surface/grain boundary area. Both the PL and PLE intensities of the $(Y_{0.95-x}Gd_xEu_{0.05})_2O_3$ phosphor powders and ceramics primarily depend on the amount of Gd^{3+} incorporation because the lower electronegativity of Gd^{3+} (1.20) than that of Y^{3+} (1.22) allows easier electron transfer.

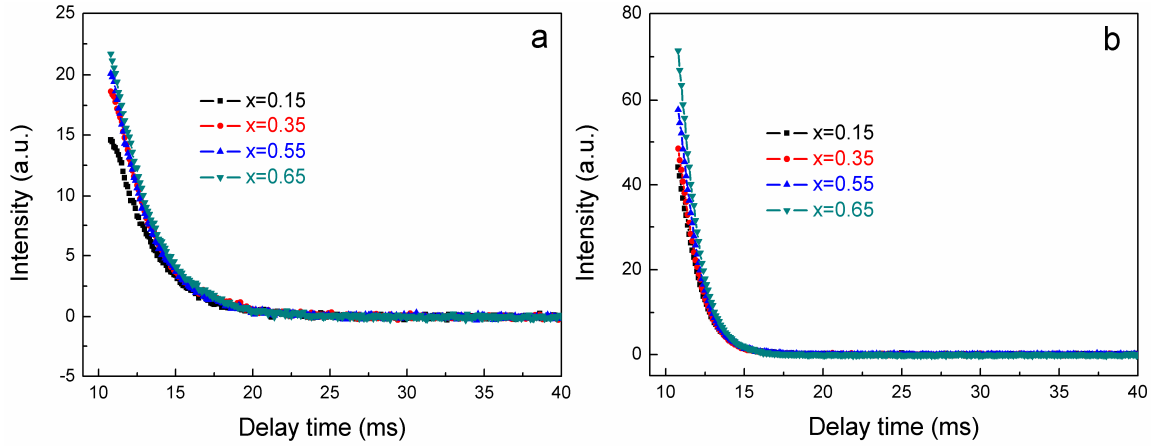

Fig. 4.10 Fluorescence decay behaviors of the $(Y_{0.95-x}Gd_xEu_{0.05})_2O_3$ powders (a) and ceramics (b) for the Eu^{3+} 613 nm emission.

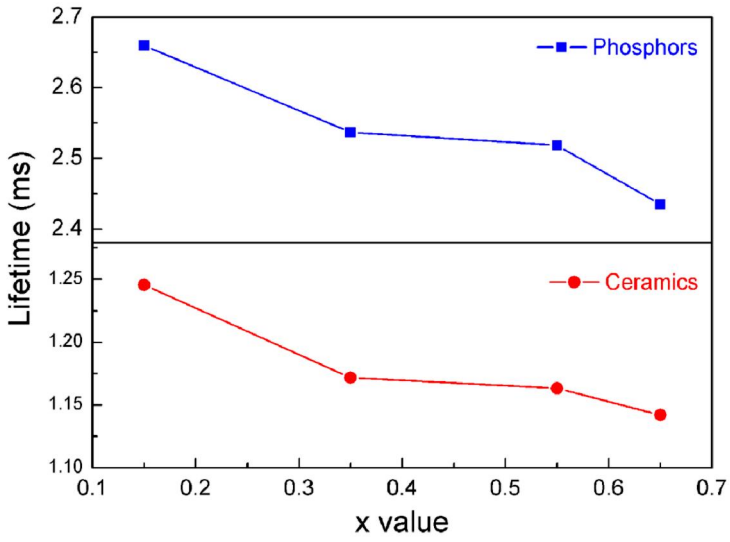

Fig. 4.11 Fluorescence lifetimes of the $(Y_{0.95-x}Gd_xEu_{0.05})_2O_3$ phosphors and ceramics for the 613 nm Eu^{3+} emission.

Figure 4.11 exhibits the fluorescence lifetimes of the $(Y_{0.95-x}Gd_xEu_{0.05})_2O_3$ phosphors and ceramics for the 613 nm red emission of Eu^{3+}, which are calculated by fitting the decay curves (Fig. 4.10) with the single exponential equation $I=Aexp(-t/\tau)+B$, where I is the emission intensity, τ is the fluorescence lifetime, t is the decay time and A and B are constants. The decreasing lifetimes of the $(Y_{0.95-x}Gd_xEu_{0.05})_2O_3$ powders at a higher Gd^{3+} concentration (2.66, 2.54, 2.52 and 2.45 ms for x=0.15, 0.35, 0.55 and 0.65, respectively, with an error of ±0.01) may be largely attributed to lattice effects, since the decomposition temperature of the precursor increases towards a higher Gd concentration and the obtained oxide powder tends to have relatively low crystallinity. On the other hand, *C*-type cubic RE_2O_3 provides two crystallographic positions

for Eu^{3+} occupancy, that is, the non-centrosymmetric C_2 and centrosymmetric S_6 (C_{3i}) sites. Concas et al.[46] indicated that Eu^{3+} is almost randomly trapped at the two sites in nanocrystalline particles, while it is preferentially trapped at the C_2 site in the bulk material owing to its state being close to equilibrium. In this study, the Gd^{3+} doping significantly promoted mass diffusion and grain growth during ceramic sintering and further expanded the host lattice, and thus it is expected that more Eu^{3+} will prefer to occupy the C_2 site of Ln_2O_3 ceramics with more Gd^{3+} incorporation. In addition, the Eu^{3+} located at the C_2 site will cause a much shorter lifetime than that at the S_6 site.[47,48] As a result, a decreasing lifetime with increasing x was observed for the ceramics (1.25, 1.17, 1.16 and 1.14 ms for x=0.15, 0.35, 0.55 and 0.65, respectively, with an error of ±0.01). For the same reason in combination with the fewer defects and larger grains, the sintered ceramics have much shorter lifetimes than the phosphor powders. The lifetimes determined in the present work also in general agreement with the reported values of 1.4-3.1 ms for Ln_2O_3:Eu (Ln=Y and Gd) phosphors,[13,49-51] and 1.0-1.6 ms for Y_2O_3:Eu, $(Y,La)_2O_3$ and Lu_2O_3:Eu ceramics.[35,52,53]

4.4 Conclusions

Highly transparent $(Y_{0.95-x}Gd_xEu_{0.05})_2O_3$ (x=0.15-0.65) ceramics have been produced via controlled processing of well-dispersed oxide powders, upon UV irradiation into strong red emissions. A detailed investigation of the effects of Gd^{3+} doping on particle properties, sintering kinetics and optical performances yielded the following major conclusions:

(1) The oxide particles derived from layered hydroxide precursors show greatly reduced hard agglomeration and the crystallite/particle sizes slightly decrease with more Gd^{3+} addition, while the grain sizes of their sintered bodies appreciably increase with increasing Gd^{3+} incorporation.

(2) In the temperature range of 1100-1480 °C, the sintering kinetics is mainly controlled by grain boundary diffusion.

(3) The bandgap energies of the $(Y_{0.95-x}Gd_xEu_{0.05})_2O_3$ ceramics generally decrease at a higher Gd^{3+} concentration.

(4) Both the oxide powders and transparent ceramics exhibit the characteristic red emission of Eu^{3+} at ~613 nm (the $^5D_0$Ÿ $^7F_2$ transition) under charge transfer (CT) excitation. Gd^{3+} substitution enhances the photoluminescence intensity, however, lowers the fluorescence lifetime.

4.5 References

[1]G. C. Wei, W. P. Lapatovich, and R. Snellgrove, ñDysprosium Oxide Ceramic Arc Tube for HID Lamps,ò *J. Phys. D: Appl. Phys.*, **41** [14] 144014 (2008).

[2]Y. H. Huang, D. L. Jiang, J. X. Zhang, and Q. L. Lin, ñFabrication of Transparent Lanthanum-Doped Yttria Ceramics by Combination of Two-Step Sintering and Vacuum Sintering,ò *J. Am. Ceram. Soc.*, **92** [12] 2883-7 (2009).

[3]B. Lu, Y. Wang, X. D. Sun, and T. Sun, ñSynthesis of Sc_2O_3 Nanopowders and Fabrication of Transparent, Two-Step Sintered Sc_2O_3 Ceramics,ò *Adv. Appl. Ceram.*, **111** [7] 389-92 (2012).

[4]R. Boulesteixa, R. Epherrea, S. Noyaua, M. Vandenhendea, A. Maîtrea, C. Salléb, G. Alombert-Gogetc, Y. Guyotc, and A. Brenierc, ñHighly Transparent Nd:Lu_2O_3 Ceramics Obtained by Coupling Slip-Casting and Spark Plasma Sintering,ò *Scripta Mater.*, **75** 54-7 (2014).

[5]E. Carnall and D. Pearlman, ñTransparent Gd_2O_3 Ceramics and Phosphors,ò *Mat. Res. Bull.*, **7** [7] 647-53 (1972).

[6]C. D. Greskovich, D. Cusano, D. Hoffman, and R. J. Riedner, ñCeramic Scintillators for Advanced, Medical X-Ray Detectors,ò *Am. Ceram. Soc. Bull.*, **71** [7] 1120-30 (1992).

[7]P. Packiyaraj and P. Thangadurai, ñStructural and Photoluminescence Studies of Eu^{3+} Doped Cubic Y_2O_3 Nanophosphors,ò *J. Lumin.*, **145** 997-1003 (2014).

[8]E. E. Brown, U. Hoemmerich, A. Bluiett, C. Kucera, J. Ballato, and S. Trivedi, ñNear-Infrared and Upconversion Luminescence in Er:Y_2O_3 Ceramics under 1.5 µm Excitation,ò *J. Am. Ceram. Soc.*, **97** [7] 2105-10 (2014).

[9]S. Z. Lu, Q. H. Yang, H. J. Zhang, Y. G. Wang, D. D. Huang, Q. Wang, and Z. Y. Wei, ñSpectroscopic Characteristics and Laser Performance of Nd:$Y_{1.8}La_{0.2}O_3$ Transparent Ceramics,ò *IEEE J. Quantum Electron.*, **49** [3] 293-300 (2013).

[10]C. Greskovich and S. Duclos, ñCeramic Scintillators,ò *Annu. Rev. Mater. Sci.*, **27** 69-88 (1997).

[11]J. K. Li, J.-G. Li, Z. J. Zhang, X. L. Wu, S. H. Liu, X. D. Li, X. D. Sun, and Y. Sakka, ñGadolinium Aluminate Garnet ($Gd_3Al_5O_{12}$): Crystal Structure Stabilization via Lutetium Doping and Properties of the $(Gd_{1-x}Lu_x)_3Al_5O_{12}$ Solid Solutions (x=0ï 0.5),ò *J. Am. Ceram. Soc.*, **95** [3] 931-6 (2012).

[12]Y. Zorenko, V. Gorbenko, I. Konstantkevych, B. Grinev, and M. Globus, ñScintillation Properties of $Lu_3Al_5O_{12}$:Ce Single-Crystalline Films,ò *Nucl. Instrum. Methods Phys. Res. Sect. A*, **486** 309-314 (2002).

[13]B. Lu, J.-G. Li, and Y. Sakka, ñControlled Processing of $(Gd,Ln)_2O_3$:Eu (Ln=Y, Lu) Red Phosphor Particles and Compositional Effects on Photoluminescence,ò *Sci. Technol. Adv. Mater.*, **14** [6] 064202 (2013).

[14]J.-G. Li, X. D. Li, X. D. Sun, and T. Ishigaki, ñMonodispersed Colloidal Spheres for Uniform $Y_2O_3:Eu^{3+}$ Red-Phosphor Particles and Greatly Enhanced Luminescence by Simultaneous Gd^{3+} Doping,ò *J. Phys. Chem. C*, **112** [31] 11707-16 (2008).

[15]X. D. Li, X. D. Sun, J.-G. Li, Z. M. Xiu, T. Gao, Y. N. Liu, and X. Z. Hu, ñCharacterization of High-Gadolinium $Y_{0.6}Gd_{1.34}Eu_{0.06}O_3$ Powder and Fabrication of Transparent Ceramic Scintillator Using Pressureless Sintering,ò *Int. J. Appl. Ceram. Technol.*, **7** [S1] E1-8 (2010).

[16]Y. K. Kim, H. K. Kim, D. K. Kim, and G. S. Cho, ñSynthesis of Eu-Doped $(Gd,Y)_2O_3$ Transparent Optical Ceramic Scintillator,ò *J. Mater. Res.*, **19** [2] 413-6 (2004).

[17]G. Cho, Y. K. Kim, S. H. Cho, D. K. Kim, B.-J. Kim, H. J. Seo, and H. K. Kim, ñSynthesis and Characterization of Doped Ceramic Scintillators Based on $(Gd,Y)_2O_3$,ò *IEEE Nucl. Sci. Symp. Conf. Rec.*, **3** 1314-7 (2005).

[18]J. Xu, Y. Shi, J. J. Xie, and F. Lei, ñFabrication, Microstructure, and Luminescent Properties of Ce^{3+}-Doped $Lu_3Al_5O_{12}$ (Ce:LuAG) Transparent Ceramics by Low-Temperature Vacuum Sintering,ò *J. Am. Ceram. Soc.*, **96** [6] 1930-6 (2013).

[19]Y. Wang, B. Lu, X. D. Sun, T. Sun, and H. Xu, ñSynthesis of Nanocrystalline Sc_2O_3 Powder and Fabrication of Transparent Sc_2O_3 Ceramics,ò *Adv. Appl. Ceram.*, **110** [2] 95-8 (2011).

[20]K. Serivalsatit, B. Kokuoz, B. Yazgan-Kokuoz, M. Kennedy, and J. Ballato, ñSynthesis, Processing, and Properties of Submicrometer-Grained Highly Transparent Yttria Ceramics,ò *J. Am. Ceram. Soc.*, **93** [5] 1320-5 (2010).

[21]J.-G. Li, T. Ikegami, and T. Mori, ñFabrication of Transparent, Sintered Sc_2O_3 Ceramics,ò *J. Am. Ceram. Soc.*, **88** [4] 817ï 21 (2005).

[22]T. Ikegami, J.-G. Li, T. Mori, and Y. Moriyoshi, ñFabrication of Transparent Yttria Ceramics by the Low-Temperature Synthesis of Yttrium Hydroxide,ò *J. Am. Ceram. Soc.*, **85** [7] 1725-9 (2002).

[23]L. Poudret, T. J. Prior, L. J. McIntyre, and A. M. Fogg, ñSynthesis and Crystal Structures of New Lanthanide Hydroxyhalide Anion Exchange Materials, $Ln_2(OH)_5X{\cdot}1.5H_2O$ (X = Cl, Br; Ln=Y, Dy, Er, Yb),ò *Chem. Mater.*, **20** [24] 7447-53 (2008).

[24]F. X. Geng, Y. Matsushita, R. Z. Ma, H. Xin, M. Tanaka, F. Izumi, N. Iyi, and T. Sasaki, ñGeneral Synthesis and Structural Evolution of a Layered Family of $Ln_8(OH)_{20}Cl_4{\cdot}nH_2O$ (Ln=Nd, Sm, Eu, Gd, Tb, Dy, Ho, Er, Tm, and Y),ò *J. Am. Chem. Soc.*, **130** [48] 16344-50 (2008).

[25]L. J. McIntyre, L. K. Jackson, and A. M. Fogg, ñ$Ln_2(OH)_5NO_3{\cdot}xH_2O$ (Ln=Y, Gd-Lu): A Novel Family of Anion Exchange Intercalation Hosts,ò *Chem. Mater.*, **20** [1] 335-40 (2008).

[26]Q. Zhu, J.-G. Li, C. Y. Zhi, X. D. Li, X. D. Sun, Y. Sakka, D. Golberg, and Y. Bando, ñLayered Rare-Earth Hydroxides (LRHs) of $(Y_{1-x}Eu_x)_2(OH)_5NO_3{\cdot}nH_2O$ (x=0-1): Structural Variations by Eu^{3+} Doping, Phase Conversion to Oxides, and the Correlation of Photoluminescence Behaviors,ò *Chem. Mater.*, **22** [14] 4204-13 (2010).

[27]X. L. Wu, J.-G. Li, J. K. Li, Q. Zhu, X. D. Li, X. D. Sun, and Y. Sakka, ñLayered Rare-Earth Hydroxide and Oxide Nanoplates of the Y/Tb/Eu System: Phase-Controlled Processing, Structure Characterization and Color-Tunable Photoluminescence via Selective Excitation and Efficient Energy Transfer,ò *Sci. Technol. Adv. Mater.*, **14** [1] 015006 (2013).

[28]Y. Ganjkhanlou, M. Kazemzad, and F. A. Hessari, ñChromaticity Dependence on Eu Concentration in Y_2O_3:Eu Nanopowders,ò *Nano*, **5** [2] 111-6 (2010).

[29]J.-G. Li, Q. Zhu, X. D. Li, X. D. Sun, and Y. Sakka, ñColloidal Processing of Gd_2O_3:Eu^{3+} Red Phosphor Monospheres of Tunable Sizes: Solvent Effects on Precipitation Kinetics and Photoluminescence Properties of the Oxides,ò *Acta Mater.*, **59** [9] 3688-96 (2000).

[30]L. F. Hu, R. Z. Ma, T. C. Ozawa, and T. Sasaki, ñOriented Monolayer Film of Gd_2O_3:0.05Eu Crystallites: Quasi-Topotactic Transformation of the Hydroxide Film and Drastic Enhancement of Photoluminescence Properties,ò *Angew. Chem. Int. Ed.*, **48** [21] 3846-9 (2009).

[31]X. L. Wu, J.-G. Li, Q. Zhu, J. K. Li, R. Z. Ma, T. Sasaki, X. D. Li, X. D. Sun, and Y. Sakka, ñThe Effects of Gd^{3+} Substitution on the Crystal Structure, Site Symmetry, and Photoluminescence of Y/Eu Layered Rare-Earth Hydroxide (LRH) Nanoplates,ò *Dalton Tran.*, **41** [6] 1854-61 (2012).

[32]R. S. Ningthoujam, R. Shukla, R. K. Vatsa, V. Duppel, L. Kienle, and A. K. Tyagi, ñGd_2O_3:Eu^{3+} Particles Prepared by Glycine-Nitrate Combustion: Phase, Concentration, Annealing, and Luminescence Studies,ò *J. Appl. Phys.*, **105** [8] 084304 (2009).

[33]F. X. Geng, Y. Matsushita, R. Z. Ma, H. Xin, M. Tanaka, N. Iyi, and T. Sasaki, ñSynthesis and Properties of Well-Crystallized Layered Rare-Earth Hydroxide Nitrates from Homogeneous Precipitation,ò *Inorg. Chem.*, **48** [14] 6724-30 (2009).

[34]R. D. Shannon, ñRevised Effective Ionic Radii and Systematic Studies of Interatomic Distances in Halides and Chalcogenides,ò *Acta Crystallogr.*, **A32** 751-67 (1976).

[35]B. Lu, J.-G. Li, T. S. Suzuki, M. Estili, W. G. Liu, X. D. Sun, and Y. Sakka, ñControlled Synthesis of Layered Rare-Earth Hydroxide Nanosheets Leading to Highly Transparent $(Y_{0.95}Eu_{0.05})_2O_3$ Ceramics,ò *J. Am. Ceram. Soc.*, **98** [5] 1413-22 (2015).

[36]J. F. Jorgen, R. H. R. Castro, T. B. Holland, and K. van Benthem, ñMechanical Properties of Individual $MgAl_2O_4$ Agglomerates and their Effects on Densification,ò *Acta Mater.*, **69** 187-95 (2014).

[37]L. C. Lim, P. M. Wong, and M. Jan, ñMicrostructural Evolution during Sintering of Near-Monosized Agglomerate-Free Submicron Alumina Powder Compacts,ò *Acta Mater.*, **48** [9] 2263-75 (2000).

[38]W. S. Young and I. B. Cutler, ñInitial Sintering with Constant Rates of Heating,ò *J. Am. Ceram. Soc.*, **53** [12] 659-663 (1970).

[39]D. L. Johnson and I. B. Cutler, ñDiffusion Sintering: 1, Initial Stage Sintering Models and their Application to Shrinkage of Powder Compacts,ò *J. Am. Ceram. Soc.*, **46** [11] 541-5 (1963).

[40]P.-L. Chen and I.-W. Chen, ñGrain Boundary Mobility in Y_2O_3: Defect Mechanism and Dopant Effects,ò *J. Am. Ceram. Soc.*, **79** [7] 1801-9 (1996).

[41]S. M. Schwarz, B. W. Kempshall, and L. A. Giannuzzi, ñEffects of Diffusion Induced Recrystallization on Volume Diffusion in the Copper-Nickel System,ò *Acta Mater.*, **51** [10] 2765-76 (2003).

[42]W. H. Rhodes, ñPhase Diagrams in Advanced Ceramicsò; pp. 2-15 in *Phase Chemistry in the Development of Transparent Polycrystalline Oxides*, Academic Press Limited, London, United Kingdom, 1995.

[43]A. Hagfeldt and M. Gratzel, ñLight-Induced Redox Reactions in Nanocrystalline Systems,ò *Chem. Rev.*, **95** [1] 49-68 (1995).

[44]Z. L. Fu, S. H. Zhou, T. Q. Pan, and S. Y. Zhang, ñPreparation and Luminescent Properties of Cubic Eu^{3+}:Y_2O_3 Nanocrystals and Comparison to Bulk Eu^{3+}:Y_2O_3,ò *J. Lumin.*, **124** [2] 213-6 (2007).

[45]Y. H. Li and G. Y. Hong, ñSynthesis and Luminescence Properties of Nanocrystalline Gd_2O_3:Eu^{3+} by Combustion Process,ò *J. Lumin.*, **124** [2] 297-301 (2007).

[46]G. Concas, G. Spano, E. Zych, and J. Trojan-Piegza, ñNano- and Microcrystalline Lu_2O_3:Eu Phosphors: Variations in Occupancy of C_2 and S_6 Sites by Eu^{3+} Ions,ò *J. Phys.: Condens. Matter*, **17** [17] 2594-604 (2005).

[47]J. Heber, K. H. Hellwege, U. Kobler, and H. Murmann, ñEnergy Levels and Interaction Between Eu^{3+}-Ions at Lattice Sites of Symmetry C_2 and Symmetry C_{3i} in Y_2O_3,ò *Z. Physik*, **237** [3] 189-204 (1970).

[48]H. Retot, S. Blahuta, A. Bessiere, B. Viana, B. LaCourse, and E. Mattmann, ñImproved Scintillation Time Response in $(Lu_{0.5}Gd_{0.5})_2O_3$:Eu^{3+} Compared with Lu_2O_3:Eu^{3+} Transparent Ceramics,ò *J. Phys. D: Appl. Phys.*, **44** [23] 235101 (2011).

[49]P. Packiyaraj and P. Thangadurai, ñStructural and Photoluminescence Studies of Eu^{3+} Doped Cubic Y_2O_3 Nanophosphors,ò *J. Lumin.*, **145** 997-1003 (2014).

[50]Q. Zhu, J.-G. Li, X. D. Li, and X. D. Sun, ñMorphology-Dependent Crystallization and Luminescence Behaviour of $(Y,Eu)_2O_3$ Red Phosphors,ò *Acta Mater.*, **57** [20] 5975-85 (2009).

[51]S. Y. Zeng, K. B. Tang, T. W. Li, and Z. H. Liang, ñ3D Flower-Like Y_2O_3:Eu^{3+} Nanostructures: Template-Free Synthesis and its Luminescence Properties,ò *J. Colloid Interface Sci.*, **316** [2] 921-9 (2007).

[52]S. Z. Lu, Q. H. Yang, Y. G. Wang, Y. H. Li, and D. D. Huang, ñLuminescent Properties of Eu:$Y_{1.8}La_{0.2}O_3$ Transparent Ceramics for Potential White LED Applications,ò *Opt. Mater.*, **35** [4] 718-21 (2013).

[53]Q. W. Chen, Y. Shi, L. Q. An, J. Y. Chen, and J. L. Shi, ñFabrication and Photoluminescence Characteristics of Eu^{3+}-Doped Lu_2O_3 Transparent Ceramics,ò *J. Am. Ceram. Soc.*, **89** [6] 2038-42 (2006).

Chapter Ⅴ

Fabrication and characterization of transparent Y_2O_3:Tb,Eu ceramics with color-tunable emission

- **Fabrication of highly transparent Y_2O_3:Tb,Eu ceramics**
- **Transition from Tb_4O_7 to Tb_2O_3 during vacuum sintering**
- **Photoluminescence behaviors of the Y_2O_3:Tb,Eu ceramics**

5.1 Introduction

Tb^{3+} and Eu^{3+} activated Y_2O_3 as two well-known green and red-emitting phosphors are widely applied in various lighting and display systems as well as multiplexed biological labeling.[1-5] Tb^{3+} can not only sensitize the $^5D_0$Ÿ $^7F_2$ red emission of Eu^{3+} to achieve strong light emission but also be used to tune the light-emitting color together with Eu^{3+}.[6-9] Along with the advances in particle processing, sinterable phosphor powders may be densified into transparent ceramics by a cost-effective pressureless sintering technique (vacuum/ atmosphere-controlled sintering). Compared with atmosphere-controlled sintering, vacuum sintering has the following advantages: (1) much lower cost and higher safety; (2) the ability to readily purify materials and remove surface absorption gases; (3) significantly reduced amounts of harmful species (H_2O, N_2, CO_2, etc.) in the sintering atmosphere; (4) a lower sintering temperature and shorter resistance time.

Simple wet-chemical routes have been frequently utilized for yielding sinterable powders, and the properties of the final oxides significantly affected by their precursors.[10-13] A protective or reducing atmosphere (e.g., hydrogen, ammonia, nitrogen, etc.) tends to be used for calcining Tb^{3+}-containing precursors,[7,14-19] since a white Tb_2O_3 powder readily oxidizes into brownish Tb_4O_7 upon heating in an oxygen/air atmosphere. An oxygen atmosphere, however, is more operative for removing the impurities in the precursor via thermal decomposition (e.g., elemental carbon, etc.) and beneficial for obtaining oxide particles with good crystallinity. Tb_4O_7 can also be transformed into Tb_2O_3 under the decreasing oxygen partial pressure and the increasing temperature.

We directly attained a brownish Tb^{4+}-containing oxide powder in this study by calcining the LRH nanosheets of the Y/Tb/Eu ternary system in oxygen atmosphere, with which highly transparent $(Y_{0.98-x}Tb_{0.02}Eu_x)_2O_3$ ceramics were successfully vacuum-sintered for color-tunable emissions. In the following, we report the powder processing and fabrication and optical properties of the transparent $(Y_{0.98-x}Tb_{0.02}Eu_x)_2O_3$ ceramics.

5.2 Experimental procedure

The starting materials used for LRH synthesis were $Y(NO_3)_3{\cdot}6H_2O$ (>99.99% pure, Kanto Chemical, Tokyo, Japan), $Eu(NO_3)_3{\cdot}6H_2O$ (>99.99% pure, Kanto Chemical) and $Tb(NO_3)_3{\cdot}6H_2O$ (>99.95% pure, Kanto Chemical).

In a typical synthetic procedure, the x value of the $(Y_{0.98-x}Tb_{0.02}Eu_x)_2O_3$ precursor was selected from 0 to 0.04 with the Tb^{3+} content was fixed at 2 at.%. A LRH precursor with ternary Y/Tb/Eu system was produced by ammonia precipitation and sulfate-ion exchange at a freezing temperature of ~4 °C. The resultant precipitation was converted to an oxide powder by thermal decomposition in a tube furnace under flowing oxygen gas (300 mL/min) at 1100 °C for 4 h with a heating rate of 5 °C/min. The detailed synthetic procedure of the Y/Eu binary-system oxide powder is given in Chapter z. It should be noted that the Tb^{3+} ions in the precursor are partially oxidized to Tb^{4+} during calcination in flowing oxygen, and thus a brownish oxide powder was resulted.

The calcined brownish oxide particles were cold isostatically pressed under a pressure of ~400 MPa. Vacuum sintering was subsequently performed in a W-heater furnace at 1700 °C for 4 h under a pressure of less than 10^{-3} Pa. The heating rate used for the ramp stage was 8 °C/min up to 1100 °C and 1 °C/min from 1100 °C up to the final sintering temperature. The sintered ceramics were finally double-sized polished to a thickness of ~1.2 mm.

Phase structure of the precursors, calcination products and ceramics was analyzed by X-ray diffractometry (XRD; Model RINT2200, Rigaku, Tokyo, Japan) using nickel filtered Cu KŬradiation with a scan speed of 1º/min. The in-line transmittances of the ceramics were measured via a UV/VIS/NIR spectrophotometer (Model SolidSpec-3700DUV, Shimadzu, Kyoto, Japan) over the wavelength range of 200ī 2000 nm. The mirror-polished specimens were chemically etched in sulfuric acid to observe their microstructures using field-emission scanning electron microscopy (FE-SEM; Model JSM-6500F, JEOL, Tokyo). The average grain sizes of the ceramics were obtained from ~100 grains using WinRoof image analysis software. The photoluminescence (PL), photoluminescence excitation (PLE) and fluorescence decay kinetics of the ceramics were analyzed by a spectrofluorometer (Model FP-6500, JASCO, Tokyo) equipped with a 60 mm-diameter integrating sphere (Model ISF-513, JASCO) and a 150 W Xe lamp as the excitation source at room temperature.

5.3 Results and discussion

5.3.1 Thermodynamic calculation for the transition from Tb_4O_7 to Tb_2O_3

The oxide powder calcined from the ion-exchanged LRH precursor in flowing O_2 appears brownish owing to oxidation of Tb^{3+} to Tb^{4+} and thus the formation of the mixed valence compound of Tb_4O_7 ($Tb_2O_3 \cdot 2TbO_2$). We hope, however, that the Tb ions are in the oxidation state of 3+ in the final ceramics, since Tb^{4+} is not luminescent and causes coloration. Whether the following reduction reaction occurs can be determined by the thermodynamic function of the Gibbs free energy (G).

$$Tb_2O_3 \cdot 2TbO_2 \rightarrow 2Tb_2O_3 + 1/2O_2 \quad (5.1)$$

In the standard state, the Gibbs free energies (G^{θ}) of Tb_2O_3, TbO_2 and O_2 are -1910.75, -996.22 and -61.13kJ/mol, respectively.[20] For equation 5.1, the change in the Gibbs free energy (φG^{θ}) was calculated to be 51 kJ/mol, implying that $Tb_2O_3 \cdot 2TbO_2$ cannot spontaneously convert into Tb_2O_3 in the standard state. Whereas, decreasing the oxygen partial pressure and increasing the temperature make it possible. In practical condition, the change in the Gibbs free energy (φG) can be calculated from the equation $\varphi G = \varphi G^{\theta} + RTlnJ$, where T is the absolute temperature, J is a function related to the gas partial pressure and R is the gas constant. Under a pressure of 10^{-3} Pa for vacuum sintering, φG becomes less than 0 kJ/mol when the temperature is above 394 °C, implying that $Tb_2O_3 \cdot 2TbO_2$ has been reduced to Tb_2O_3.

Moreover, the result of the thermodynamic calculation suggests a good way to directly attain Tb^{3+}-containing oxide powders while avoiding the use of harmful NH_3 or dangerous H_2 during particle synthesis (also applicable to deoxidize commercial Tb_4O_7 powder), namely, vacuum treatment at a proper heating temperature.

5.3.2 Phase structure of the $(Y_{0.98-x}Tb_{0.02}Eu_x)_2O_3$ precursors, oxide powders and ceramics

Figure 5.1a exhibits XRD patterns of the original LRH (R=0) and the sulfate-exchange (R=0.03) precursors of ternary Y-Tb-Eu system. A series of 00l and sharp 220 diffractions were observed to be characteristic of the LRH compound in each case.[21] Both the sulfate exchange and Eu^{3+} addition induce peak shifting of the 002 and 220 reflections, and the explanations of such phenomena have been derailed in Chapter Ⅳ.

All the diffraction peaks of the oxide powders (Fig. 5.1b) and vacuum sintered ceramics (Fig. 5.1c) can be well indexed with cubic structured Y_2O_3 (JCPDS No. 01-083-0927) in each case, and the sharp diffractions imply high crystallinity. No obvious peak shifting was found at a higher Eu^{3+} concentration for

both the material forms because of the limited amount of Eu^{3+} and the similar ionic radii of Tb^{3+} (0.0923 nm for six-fold coordination) and Eu^{3+} (0.0947 nm for six-fold coordination).[22] The lattice parameters of the oxide powders and ceramics calculated from the (222) diffraction are ~1.0587 and 1.0680 nm, respectively. Compared with the cell dimension of pure Y_2O_3 (1.0608 nm, JCPDS No. 01-083-0927), the smaller values of the oxide powders are owing to the presence of an appreciable amount of Tb^{4+}, which is significantly smaller than not only Tb^{3+} and Eu^{3+} but also Y^{3+}. It is known that, for the six-fold coordination of Ln^{3+} in the sesquioxide of Ln_2O_3, Tb^{4+}, Y^{3+}, Tb^{3+} and Eu^{3+} have ionic radii of 0.0760, 0.0900, 0.0923, and 0.0947 nm, respectively.[22] The final resultant ceramics have larger lattice constants than Y_2O_3, which can be attributed to the larger sizes of Tb^{3+} and Eu^{3+} than Y^{3+} and is an indication of Tb^{4+}Ÿ Tb^{3+} conversion during vacuum sintering. This is in accordance with the theoretical calculation and the colorlessness of the vacuum-sintered ceramics (Fig 5.2) .

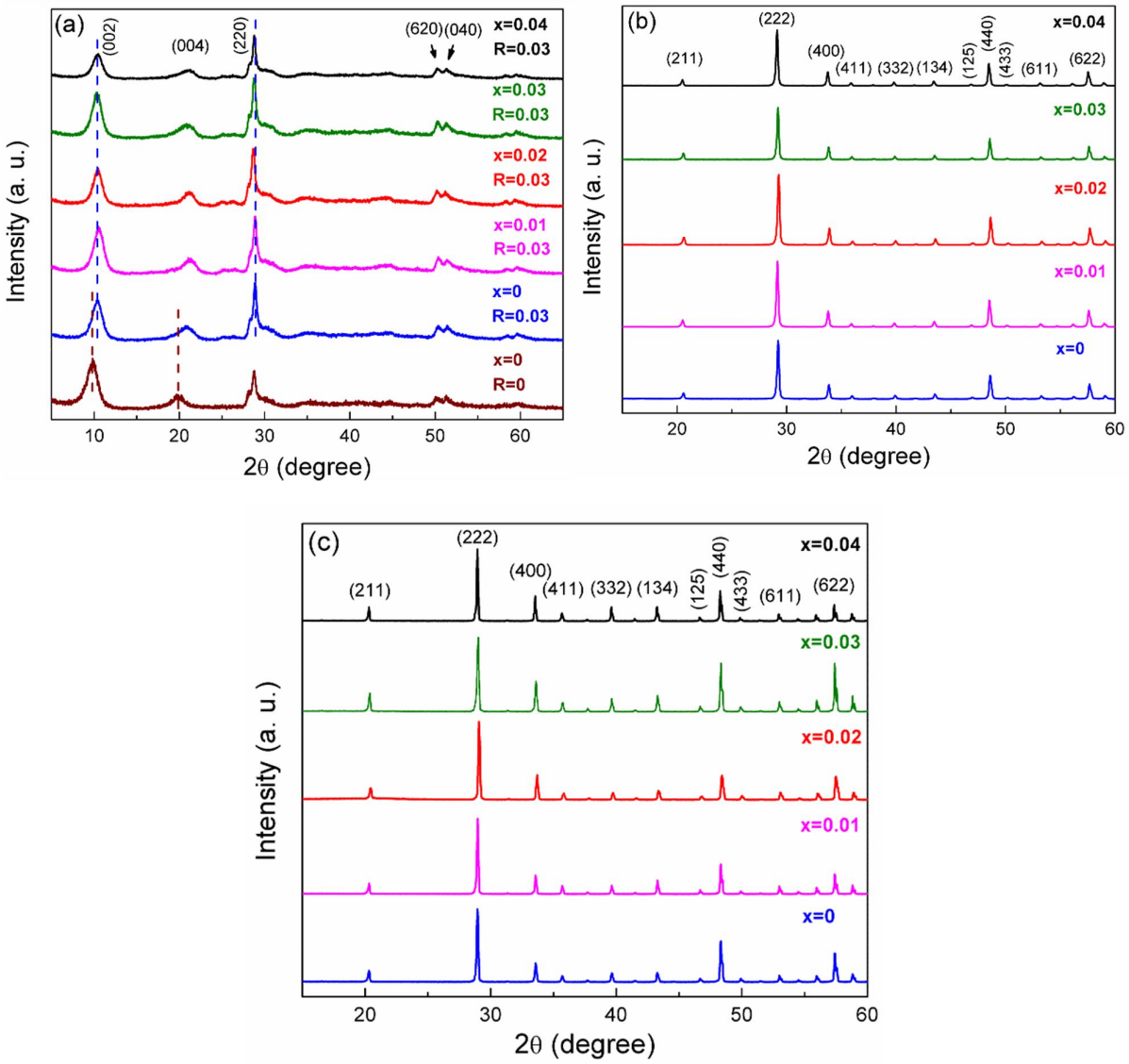

Fig. 5.1 XRD patterns of the LRH precursors before (R=0) and after SO_4^{2-} exchange (a), the oxide powders obtained by calcining the sulfate-exchanged LRH precursors in flowing oxygen at 1100 °C for 4 h (b), and the vacuum sintered transparent ceramics (c). The *x* value denotes Eu content in the $(Y_{0.98-x}Tb_{0.02}Eu_x)^{3+}$ combination.

5.3.3 Transmittances and microstructures of the $(Y_{0.98-x}Tb_{0.02}Eu_x)_2O_3$ ceramics

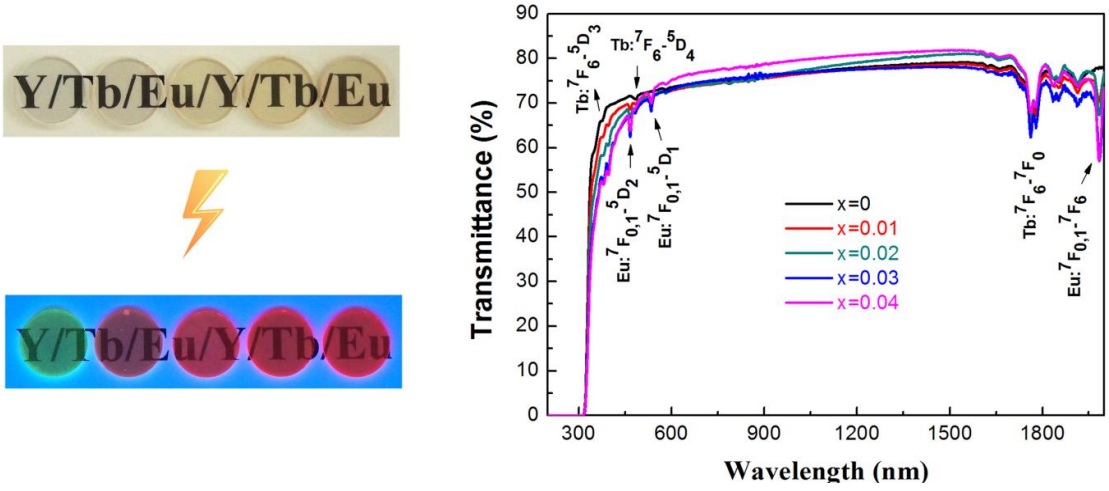

Fig. 5.2 Appearances (left panel) and in-line transmittances (right panel) of the transparent $(Y_{0.98-x}Tb_{0.02}Eu_x)_2O_3$ ceramics. The symbols in the right panel correspond to the four ceramics (from left to right) exhibited in the left panel. The lower part of the left panel shows the observed green to red emission under excitation from a 254 nm UV lamp. All five specimens have a thickness of 1.2 mm.

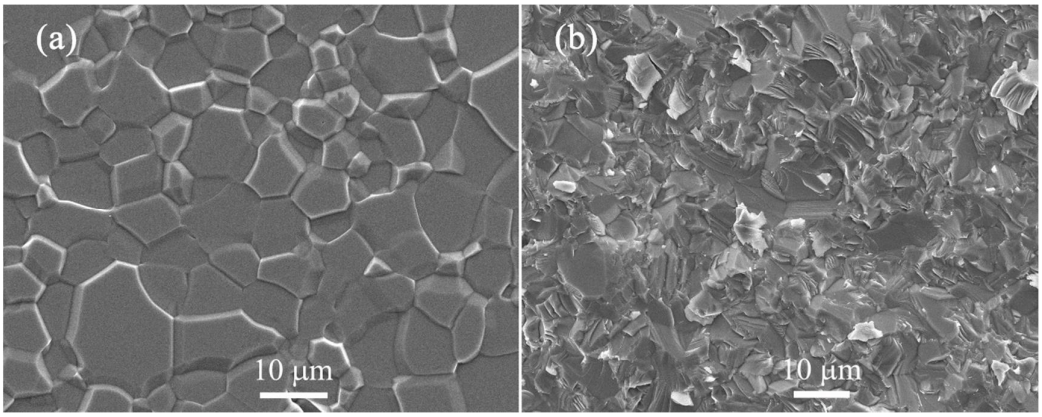

Fig. 5.3 FE-SEM micrograph showing the polished surface (a) and fracture surface (b) of the $(Y_{0.95}Tb_{0.02}Eu_{0.03})_2O_3$ ceramic.

Figure 5.2 shows the appearances and in-line transmittances of the $(Y_{0.98-x}Tb_{0.02}Eu_x)_2O_3$ (x=0-0.04) ceramics. The five specimens exhibit high transparency to the naked eye. Upon UV irradiation at 254 nm, the transparent bodies display strong green to red emissions that correspond to the $^5D_4$Ÿ $^7F_5$ transitions of Tb^{3+} and $^5D_0$Ÿ $^7F_{1,2}$ transitions of Eu^{3+} (Fig. 5.2, lower part of left panel). The absorption bands indicated on the transmittance curves accord with the intra-4f^6 transition of Eu^{3+} and the intra-4f^8 transition of Tb^{3+}.

The theoretical transmittance of an Y_2O_3 single crystal is ~81% at a wavelength of 613 nm.[23] The in-line transmittances of $(Y_{0.98-x}Tb_{0.02}Eu_x)_2O_3$ ceramics are ~74, 73, 74, 74 and 76% for x=0, 0.01, 0.02, 0.03 and 0.04 at 613 nm, which are ~91, 90, 91, 91 and 94% of the theoretical value, respectively. The transmittances of the $(Y_{0.98-x}Tb_{0.02}Eu_x)_2O_3$ ceramics in the visible region are ~5% lower than that of the $(Y_{0.95}Eu_{0.05})_2O_3$ ceramic made in Chapter 3. Formation of LRHs underwent different precipitation behaviors for different Ln^{3+},[24] and hence the presence of Tb^{3+} may have affected some characteristics of the Y-Tb-Eu

ternary LRH nanosheets. Additionally, trace of Tb^{4+} may also exist in the sintered body, which would lead to light absorption, particularly in the visible-light region.

The polished surface and fracture surface of the $(Y_{0.95}Tb_{0.02}Eu_{0.03})_2O_3$ ceramic are shown in Fig. 5.3. The grain size is uniform with an average grain size of ~12 εm, and no residual pores or abnormal grain growth can be observed (Fig. 5.3a). From the fracture surface (Fig. 5.3b), it can be seen that the fully dense ceramic is mainly intragranularly fractured.

5.3.4 Photoluminescence behaviors of the transparent $(Y_{0.98-x}Tb_{0.02}Eu_x)_2O_3$ ceramics

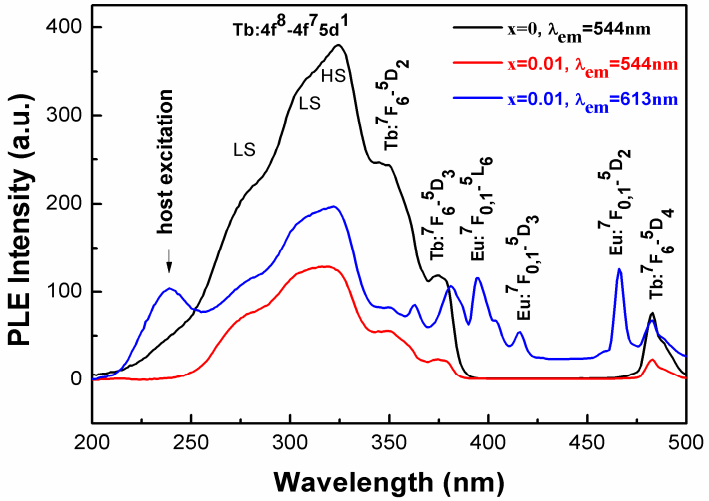

Fig. 5.4 PLE behaviors of $(Y_{0.98-x}Tb_{0.02}Eu_x)_2O_3$ (x=0 and 0.01) ceramics observed by monitoring the 544 and 613 nm emissions.

Figure 5.4 shows the PLE spectra of the transparent $(Y_{0.98}Tb_{0.02})_2O_3$ and $(Y_{0.97}Tb_{0.02}Eu_{0.01})_2O_3$ ceramics obtained by monitoring green Tb^{3+} emission at 544 nm and red Eu^{3+} emission at 613 nm. Owing to crystal-field interaction and spin-orbit coupling, the $(Y_{0.98}Tb_{0.02})_2O_3$ ceramic exhibits two spin-allowed (low-spin $4f^75d^1$ excited state, LS) bands at ~303 and 281 nm and one spin-forbidden (high-spin $4f^75d^1$ excited state of Tb^{3+}, HS) band at ~323 nm. The two LS bands are much weaker than HS band. By monitoring the 544 nm Tb^{3+} green emission, the $(Y_{0.97}Tb_{0.02}Eu_{0.01})_2O_3$ ceramic shows an almost identical PLE spectrum to that of $(Y_{0.98}Tb_{0.02})_2O_3$ but relatively low excitation intensity due to the energy transfer from Tb^{3+} to Eu^{3+}. However, the intensity of its 303 nm LS PLE becomes close to that of the HS band because the spin-allowed transition is more sensitive to the relative concentration of Tb^{3+} and Eu^{3+} ions in the Y_2O_3 host lattice.[25] On the other hand, the strong Tb^{3+} $4f^8$-$4f^75d^1$ transition of $(Y_{0.98-x}Tb_{0.02}Eu_x)_2O_3$ ceramics also induces to a longer starting wavelength in their transmittance curves (Fig. 5.1, ~320 nm) than that of the $(Y_{0.95}Eu_{0.05})_2O_3$ ceramic (~270 nm).[23]

The broad charge-transfer (CT) band center of the transparent $(Y_{0.95}Eu_{0.05})_2O_3$ ceramic was found to be located at ~267 nm.[23] Monitoring the 613 nm red emission of Eu^{3+} yielded the $4f^8$-$4f^75d^1$ transition band of Tb^{3+} for the $(Y_{0.97}Tb_{0.02}Eu_{0.01})_2O_3$ ceramic (its CT band of Eu^{3+} overlaps with the LS), together with peaks above a wavelength of 350 nm arising from the intra-$4f^8$ transition of Tb^{3+} and the intra-$4f^6$ transition of Eu^{3+} and a peak at ~239 nm corresponding to the absorption of rare-earth-oxide host lattice. Considering the energy transfer from Tb^{3+} to Eu^{3+}, strong Eu^{3+} luminescence can be obtained by excitation of the 323 nm Tb^{3+} HS band rather than that of the 270 nm Eu^{3+} CT band.

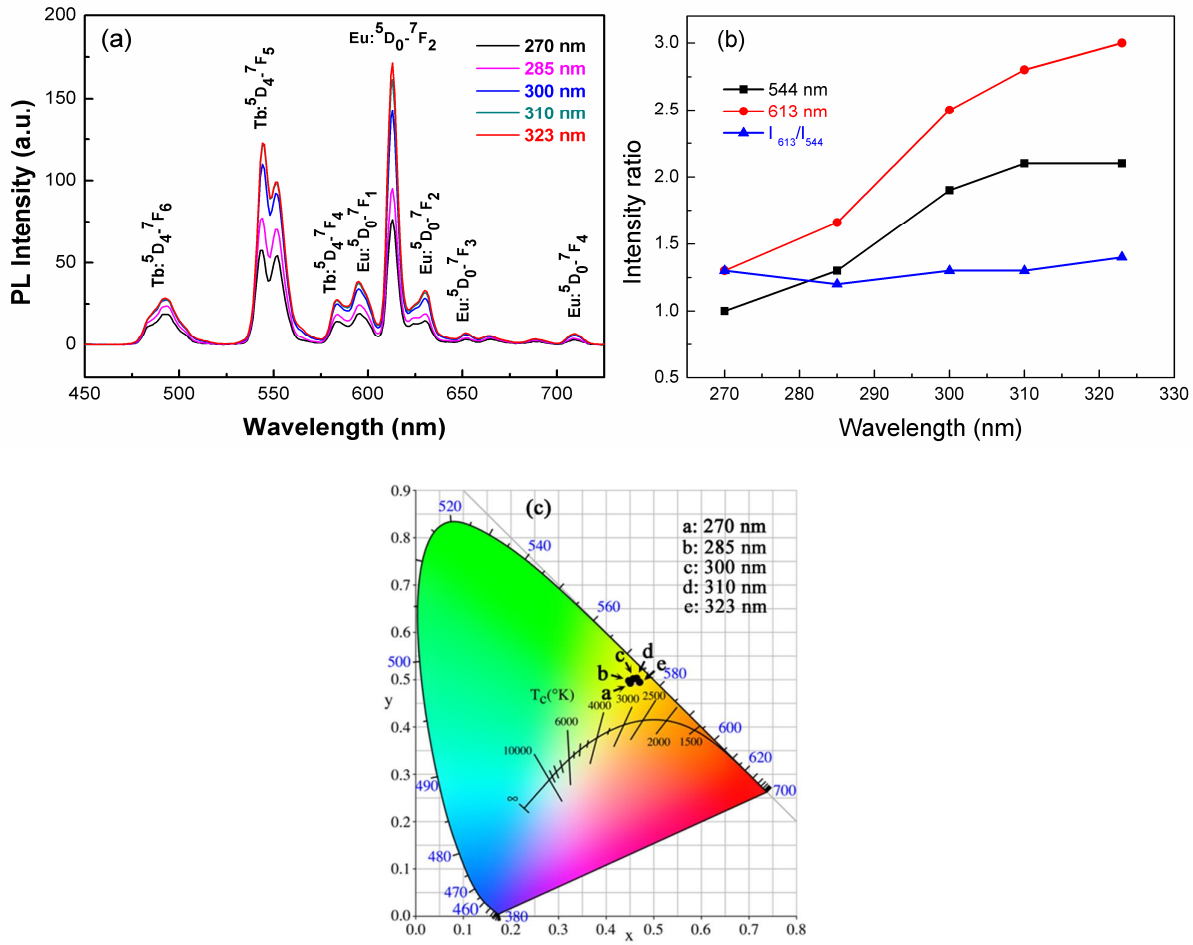

Fig. 5.5 PL spectra of the $(Y_{0.97}Tb_{0.02}Eu_{0.01})_2O_3$ ceramic under excitation wavelength of 270-323 nm (a), PL intensities of the 544 and 613 nm emissions normalized to 1 for the lowest value, and the I_{613}/I_{544} and I_{544}/I_{492} intensity ratios (b). CIE chromaticity diagram of the sample (c).

The effects of excitation at wavelengths of 270-323 nm on the luminescence of the transparent $(Y_{0.97}Tb_{0.02}Eu_{0.01})_2O_3$ ceramic are shown in Fig. 5.5a. This material exhibits two groups of characteristic emissions corresponding to the $^5D_4$Ÿ ^7F_J (J=4, 5, 6) transitions of Tb^{3+} and the $^5D_0$Ÿ ^7F_J (J=0, 1, 2, 3, 4) transitions of Eu^{3+},[7,8,26,27] with their respective strongest peaks located at 544 nm and 613. The PL intensities of both Tb^{3+} and Eu^{3+} increase at a longer excitation wavelength (Fig. 5.5b). The increment of the PL intensity for Tb^{3+} is in that the wavelength shifts towards to the center of the Tb^{3+} HS band (Fig. 5.4), and increase in the intensity of Eu^{3+} emission is attributable to the energy transfer from Tb^{3+} to Eu^{3+}, albeit apart away from the center of the CT band. The intensity ratio of the red and green emissions (I_{613}/I_{544}) generally remains constant at ~1.3 (Fig. 5.5b), elucidating that the two colors undergo nearly simultaneous growth and generally remain unchanged in the wavelength range of 270-323 nm. The CIE chromaticity coordinates of the sample are (0.45, 0.49), (0.45, 0.50), (0.46, 0.50), (0.46, 0.50) and (0.47, 0.49) under excitation wavelengths of 270-323 nm (Fig. 5.5c), which all fall into the yellow color region, reflecting the constant value of I_{613}/I_{544}.

Figure 5.6a shows the PL behavior of the $(Y_{0.98-x}Tb_{0.02}Eu_x)_2O_3$ ceramics under excitation at the wavelength of the Tb^{3+} HS band (323 nm). The $(Y_{0.98}Tb_{0.02})_2O_3$ ceramic exhibits characteristic Tb^{3+} emission with four groups of split peaks: $^5D_4$Ÿ $^7F_5$ strong green emission at ~544 nm, $^5D_4$Ÿ $^7F_6$ weak blue emission at

~492 nm, $^5D_4$Ÿ $^7F_3$ red emission at ~624 nm and $^5D_4$Ÿ $^7F_4$ yellow emission at ~585 nm . No $^5D_3$Ÿ ^7F_J transitions are observed since the high Tb^{3+} concentration (more than 1 at.%) induces cross relaxation from the $^5D_3$Ÿ $^5D_4$ and $^7F_6$Ÿ $^7F_0$ transitions.[28-30] The PL intensity of Tb^{3+} decreases along with increasing *x*. The addition of only 1% Eu^{3+} significantly reduces the PL intensity of Tb^{3+} by ~67%. On the other hand, the PL intensity of Eu^{3+} increases with more Eu^{3+} addition up to x=0.02 owing to efficient energy transfer from Tb^{3+} to Eu^{3+}. However, as the Eu^{3+} concentration increases, luminescence quenching occurs, causing decreased PL intensity. At the maximum Eu^{3+} emission intensity, the total activator concentration was found to be 4 at.%, in compliance with a previous report on Y_2O_3:Tb/Eu phosphor powders.[8]

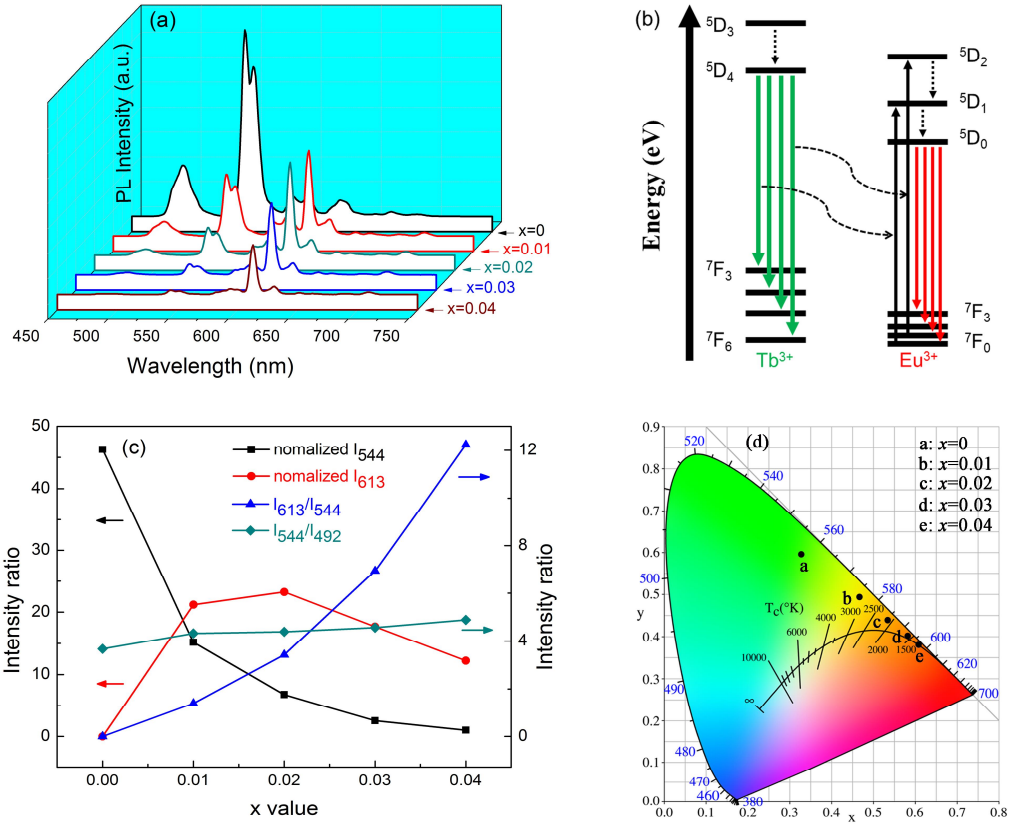

Fig. 5.6 PL spectra of the transparent $(Y_{0.98-x}Tb_{0.02}Eu_x)_2O_3$ (x=0-0.04) ceramics under excitation at the wavelength of the Tb^{3+} HS band (323 nm) (a), Energy level scheme representing the process of energy transfer from Tb^{3+} to Eu^{3+} (b), relative intensities of the 544 and 613 nm emissions and the I_{613}/I_{544} and I_{544}/I_{492} intensity ratios (c), and CIE chromaticity diagram showing the emission colors of the ceramics (d).

The energy transfer process can be discussed with the scheme shown in Fig. 5.6b. That is, under excitation at the wavelength of 323 nm, the $4f^8$ electrons of Tb^{3+} are raised to the $4f^75d^1$ energy level, which then relax to the $^5D_3$ and finally $^5D_4$ states. It can be observed that the energy of Tb^{3+} ($^5D^3$ and $^5D_4$) is a bit higher than that of Eu^{3+} ($^5D_1$ and $^5D_0$), implying that energy transfer may occur via the nonradiative process. Moreover, the $^5D_4$-$^7F_6$ and $^5D_4$-$^7F_3$ emissions of Tb^{3+} is overlapped with the absorption bands $^7F_1$-$^5D_2$ or $^7F_0$-$^5D_1$ of Eu^{3+}, respectively, and hence the energy transfer from Tb^{3+} to Eu^{3+} is very efficient through the cross relaxation process.[31-35] Upon UV excitation, a part of the excitation energy can be transferred to $^5D_{1,2}$ states of Eu^{3+} from the emission of Tb^{3+}, then fell to the $^5D_0$ energy level by energy relaxation, and finally jumped back to the ^7F_J (J=1-4) level of Eu^{3+} by radiative transition, which enhances the characteristic emission of Eu^{3+}. The amount of energy transferred from Tb^{3+} is dependent on the content of Eu^{3+} in the Y_2O_3 host, and

thus varied emission intensities are observed from Fig. 5.6a for both the Tb^{3+} and Eu^{3+} activators.

The red to green intensity ratio I_{613}/I_{544} (Fig. 5.6c) greatly increases at a higher Eu^{3+} concentration ascribed to the efficient energy transfer and the rapid quenching for Tb^{3+} as evidenced by Fig. 5.7. On the other hand, the green to blue ratio of I_{544}/I_{492} generally remains at ~4, implying that Eu^{3+} doping does not substantially affect the inner energy level of the Tb^{3+}.

The CIE chromaticity coordinates of the transparent $(Y_{0.98-x}Tb_{0.02}Eu_x)_2O_3$ (x=0-0.04) ceramics are (0.33, 0.60), (0.47, 0.49), (0.54, 0.44), (0.58, 0.40) and (0.61, 0.38) for x=0, 0.01, 0.02, 0.03 and 0.04, respectively (Fig. 5.6d). The corresponding colors are yellowish-green, yellow, yellowish-orange, orange and reddish-orange, roughly comparable to those of the observed ceramic objects under UV irradiation at 254 nm (Fig. 5.2).

As the relationship between the energy transfer (η_{ET}) and the luminescence intensities of the donor (Tb^{3+}) in the presence (I) and absence (I_0) of the acceptor (Eu^{3+}) can be expressed as $\eta_{ET}=1-I/I_0$,[36] η_{ET} is estimated to be ~67.2 and 85.3% for the specimen with x=0.01 and 0.02, respectively. Such high energy-transfer efficiencies can also be attributable to the overlap between the $^5D_4$Ÿ $^7F_{3,6}$ emission of Tb^{3+} and the $^7F_{0,1}$Ÿ $^5D_{1,2}$ absorption of Eu^{3+}.[31-35]

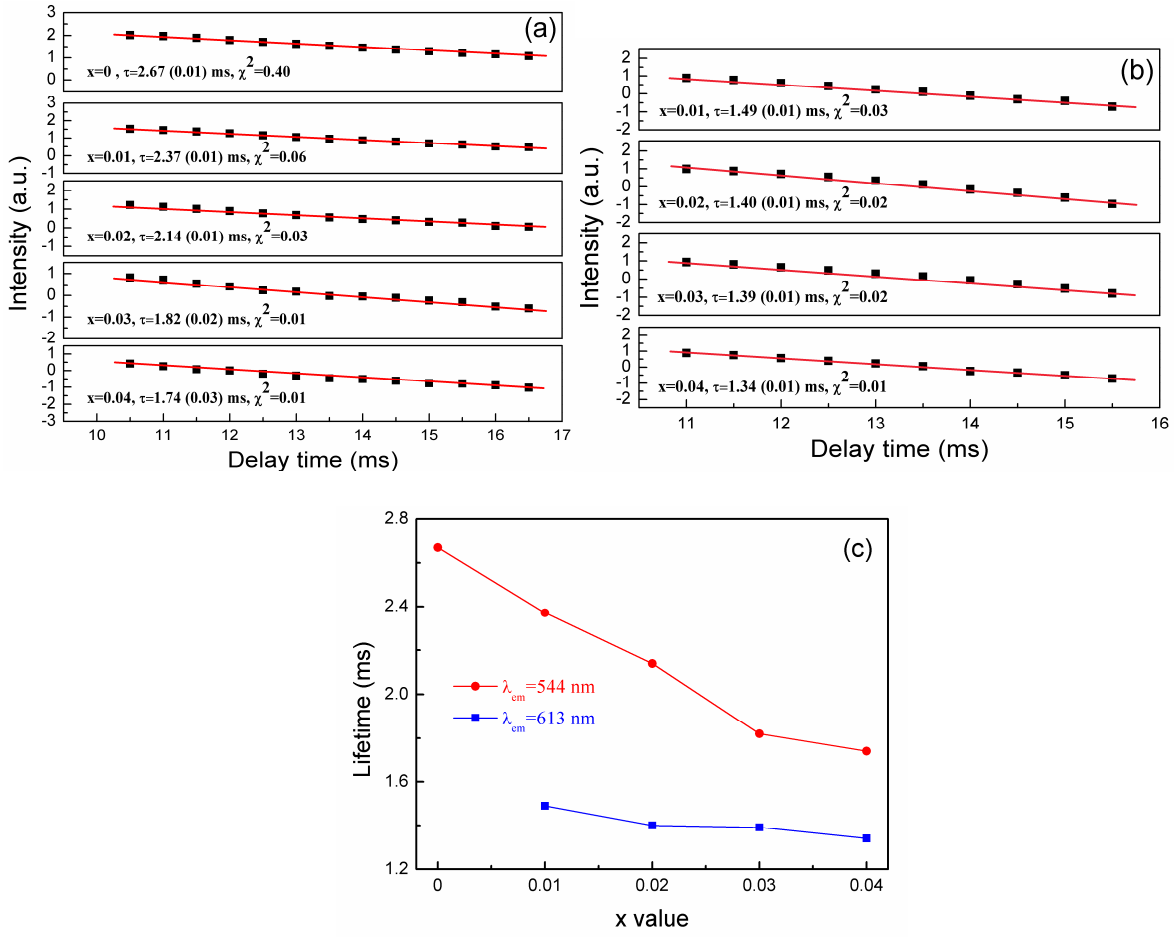

Fig. 5.7 Fluorescence decay behaviors of the $(Y_{0.98-x}Tb_{0.02}Eu_x)_2O_3$ ceramics for the 544 nm Tb^{3+} emission (a) and 613 nm Eu^{3+} emission (b), along with their lifetimes (c).

Figures 5.7a and b exhibit the decay kinetics of the transparent $(Y_{0.98-x}Tb_{0.02}Eu_x)_2O_3$ ceramics for the 544 nm Tb^{3+} and 613 nm Eu^{3+} emissions, respectively. The fluorescence lifetime can be calculated by

fitting the decay curve with the single exponential function $I=Aexp(-t/\tau)+B$, where τ is the fluorescence lifetime, t is the decay time, I is the emission intensity and A and B are constants. Under the Tb^{3+} emission, the lifetime rapidly decreases with increasing Eu^{3+} addition due to the energy transfer from Tb^{3+} to Eu^{3+} (Fig. 5.7c).[24,35] The lifetime of the Eu^{3+} emission slightly decreases at a higher Eu^{3+} concentration since more Eu^{3+} incorporation reduces the distance between luminescent centers, which may raise the nonradiative relaxation rate.[7] In addition, nonradiative transition probability is greater in distorted environments generated by increasing x, contributing to the decreased lifetimes.[25] The fluorescence lifetimes of $(Y_{0.98-x}Tb_{0.02}Eu_x)_2O_3$ ceramics for the 544 nm Tb^{3+} emission are much higher than those for the 613 nm Eu^{3+} emission also because of the energy transfer. The lifetimes of the latter determined in this work (1.34-1.49±0.01 ms) are also fall into the reported values of 1.0-1.6 ms for Y_2O_3:Eu, $(Y,La)_2O_3$:Eu and Lu_2O_3:Eu ceramics.[22,37,38]

5.4 Conclusions

Brownish Tb^{4+}-containing oxide powders calcined from layered rare-earth hydroxide precursors in oxygen atmosphere have been reduced and densified into transparent $(Y_{0.98-x}Tb_{0.02}Eu_x)_2O_3$ (x=0-0.04) ceramics with color-tunable emission via vacuum sintering. A systematic investigation on $(Y_{0.98-x}Tb_{0.02}Eu_x)_2O_3$ ceramics yielded the following major conclusions:

(1) Improved emissions for both Eu^{3+} and Tb^{3+} were attained by varying the excitation wavelength from 270 to 323 nm, without notably changing the color coordinates of the whole emission.

(2) By unitizing the effective energy transfer from Tb^{3+} to Eu^{3+}; the emission colors of the $(Y_{0.98-x}Tb_{0.02}Eu_x)_2O_3$ ceramics can be precisely tuned from yellowish green to reddish orange via varying the Eu^{3+}/Tb^{3+} ratio.

(3) At the maximum Eu^{3+} emission intensity (for total activator content of 4 at.%), energy transfer with an efficiency of ~85.3% was achieved.

(4) The fluorescence lifetimes of the $(Y_{0.98-x}Tb_{0.02}Eu_x)_2O_3$ ceramics for both the 544 nm Tb^{3+} and 613 nm Eu^{3+} emissions decreased at a higher Eu^{3+} concentration.

5.5 References

[1]A. Paulraj, P. Natarajan, K. Munnisamy, M. K. Nagoor, K. P. Nattar, B. Abdulrazak, and J. Duraisamy, ñPhotoluminescence Efficiencies of Nanocrystalline versus Bulk Y_2O_3:Eu Phosphor-Revisited,ò *J. Am. Ceram. Soc.*, **94** [5] 1627-33 (2011).

[2]J.-G. Li, X. D. Li, X. D. Sun, and T. Ishigaki, ñMonodispersed Colloidal Spheres for Uniform Y_2O_3:Eu^{3+} Red-Phosphor Particles and Greatly Enhanced Luminescence by Simultaneous Gd^{3+} Doping,ò *J. Phys. Chem. C*, **112** [31] 11707-16 (2008).

[3]G. Wakefield, E. Holland, P. J. Dobson, and J. L. Hutchison, ñLuminescence Properties of Nanocrystalline Y_2O_3:Eu,ò *Adv. Mater.*, **13** [20] 1557-60 (2001).

[4]G. A. Sotiriou, D. Franco, D. Poulikakos, and A. Ferrari, ñOptically Stable Biocompatible Flame-Made SiO_2-Coated Y_2O_3:Tb^{3+} Nanophosphors for Cell Imaging,ò *ACS Nano*, **6** [5] 3888-97 (2012).

[5]L. Wang, L. Shi, N. Liao, H. Jia, P. Du, Z. Xi, L. Wang, and D. Jin, ñPhotoluminescence Properties of Y_2O_3:Tb^{3+} and YBO_3:Tb^{3+} Green Phosphors Synthesized by Hydrothermal Method,ò *Mater. Chem. Phys.*, **119** [3] 490-4 (2010).

[6]G. A. Sotiriou, M. Schneider, and S. E. Pratsinis, ñColor-Tunable Nanophosphors by Codoping Flame-Made Y_2O_3 with Tb and Eu,ò *J. Phys. Chem. C*, **115** [4] 1084-9 (2011).

[7]X. L. Wu, J.-G. Li, J. K. Li, Q. Zhu, X. D. Li, X. D. Sun, and Y. Sakka, ñLayered Rare-Earth Hydroxide and Oxide Nanoplates of the Y/Tb/Eu System: Phase-Controlled Processing, Structure Characterization and Color-Tunable Photoluminescence via Selective Excitation and Efficient Energy Transfer,ò *Sci. Technol. Adv. Mater.*, **14** [1] 015006 (2013).

[8]T. S. Atabaev, H.-K. Kim, and Y.-H. Hwang, ñSubmicron Y_2O_3 Particles Codoped with Eu and Tb Ions: Size Controlled Synthesis and Tuning the Luminescence Emission,ò *J. Colloid Interface Sci.*, **373** [1] 14-9 (2012).

[9]Z. L. Liu, L. X. Yu, Q. Wang, Y. C. Tao, and H. Yang, ñEffect of Eu,Tb Codoping on the Luminescent Properties of Y_2O_3 Nanorods,ò *J. Lumin.*, **131** [1] 12-6 (2011).

[10]B. Lu, Y. Wang, X. D. Sun, and T. Sun, ñSynthesis of Sc_2O_3 Nanopowders and Fabrication of Transparent, Two-Step Sintered Sc_2O_3 Ceramics,ò *Adv. Appl. Ceram.*, **111** [7] 389-92 (2012).

[11]J.-G. Li, T. Ikegami, and T. Mori, ñFabrication of Transparent, Sintered Sc_2O_3 Ceramics,ò *J. Am. Ceram. Soc.*, **88** [4] 817ï 21 (2005).

[12]K. Serivalsatit and J. Ballato, ñSubmicrometer Grain-Sized Transparent Erbium-Doped Scandia Ceramics,ò *J. Am. Ceram. Soc.*, **93** [11] 3657-62 (2010).

[13]Y. Wang, B. Lu, X. D. Sun, T. Sun, and H. Xu, ñSynthesis of Nanocrystalline Sc_2O_3 Powder and Fabrication of Transparent Sc_2O_3 Ceramics,ò *Adv. Appl. Ceram.*, **110** [2] 95-8 (2011).

[14]L. Zhao, D. Y. Wang, Y. H. Wang, and Y. Tao, ñVisible Quantum Cutting and Energy Transfer in Tb^{3+}-Doped KSr(Gd,Y)$(PO_4)_2$ Under VUVï UV Excitation,ò *J. Am. Ceram. Soc.*, **97** [12] 3913-7 (2014).

[15]Y. C. Kang, I. W. Lenggoro, S. B. Park, and K. Okuyama, ñPhotoluminescence Characteristics of YAG:Tb Phosphor Particles with Spherical Morphology and Non-Aggregation,ò *J. Phys. Chem. Solids*, **60** [11] 1855-8 (1999).

[16]Y. S. Lin and R. S. Liu, ñChemical Substitution Effects of Tb^{3+} in YAG:Ce Phosphors and Enhancement of Their Emission Intensity Using Flux Combination,ò *J. Lumin.*, **122** 580-2 (2007).

[17]Y. Satoh, S. Ohshio, and H. Saitoh, ñPhotoluminescence Spectroscopy of Highly Oriented Y_2O_3:Tb Crystalline Whiskers,ò *Sci. Technol. Adv. Mater.*, **6** [2] 215-8 (2005).

[18]M. A. Flores-Gonzalez, G. Ledoux, S. Roux, K. Lebbou, P. Perriat, and O. Tillement, ñPreparing Nanometer Scaled Tb-Doped Y_2O_3 Luminescent Powders by the Polyol Method,ò *J. Solid State Chem.*, **178**

[4] 989-97 (2005).

[19]Y.-C. Fang, X.-R. Huang, Y.-D. Juang, and S.-Y. Chu, ñColor-Tunable Blue to Green $Ca_{4-1.5x}Ta_2O_9$:$x$$Tb^{3+}$ Phosphor: Cross-Relaxation Mechanism and Thermal Stability,ò *J. Am. Ceram. Soc.*, **95** [5] 1613-8 (2012).

[20]D. L. Ye and J. H. Hu, Thermodynamic Data Manual of Inorganic Matter. Metallurgy Industry Press, Beijing, China, 2002.

[21]F. X. Geng, Y. Matsushita, R. Z. Ma, H. Xin, M. Tanaka, N. Iyi, and T. Sasaki, ñSynthesis and Properties of Well-Crystallized Layered Rare-Earth Hydroxide Nitrates from Homogeneous Precipitation,ò *Inorg. Chem.*, **48** [14] 6724-30 (2009).

[22]R. D. Shannon, ñRevised Effective Ionic Radii and Systematic Studies of Interatomic Distances in Halides and Chalcogenides,ò *Acta Crystallogr.*, **A32** 751-67 (1976).

[23]B. Lu, J.-G. Li, T. S. Suzuki, M. Estili, W. G. Liu, X. D. Sun, and Y. Sakka, ñControlled Synthesis of Layered Rare-Earth Hydroxide Nanosheets Leading to Highly Transparent $(Y_{0.95}Eu_{0.05})_2O_3$ Ceramics,ò *J. Am. Ceram. Soc.*, **98** [5] 1413-22 (2015).

[24]X. L. Wu, J.-G. Li, Q. Zhu, W. G. Liu, J. Li, X. D. Li, X. D. Sun, and Y. Sakka, ñOne-Step Freezing Temperature Crystallization of Layered Rare-Earth Hydroxide ($Ln_2(OH)_5NO_3{\cdot}nH_2O$) Nanosheets for a Wide Spectrum of Ln (Ln=Pr-Er, and Y), Anion Exchange with Fluorine and Sulfate, and Microscopic Coordination Probed via Photoluminescence,ò *J. Mater. Chem. C*, **3** [14] 3428-37 (2015).

[25]S. Mukherjee, V. Sudarsan, R. K. Vatsa, S. V. Godbole, R. M. Kadam, U. M. Bhatta, and A. K. Tyagi, ñEffect of Structure, Particle Size and Relative Concentration of Eu^{3+} and Tb^{3+} Ions on the Luminescence Properties of Eu^{3+} Co-Doped Y_2O_3:Tb Nanoparticles,ò *Nanotechnology*, **19** [32] 325704 (2008).

[26]M. Back, M. Boffelli, A. Massari, R. Marin, F. Enrichi, and P. Riello, ñEnergy Transfer between Tb^{3+} and Eu^{3+} in Co-Doped Y_2O_3 Nanocrystals Prepared by Pechini Method,ò *J. Nanopart. Res.*, **15** [7] 1753 (2013).

[27]B. Lu, J.-G. Li, and Y. Sakka, ñControlled Processing of $(Gd,Ln)_2O_3$:Eu (Ln=Y, Lu) Red Phosphor Particles and Compositional Effects on Photoluminescence,ò *Sci. Technol. Adv. Mater.*, **14** [6] 064202 (2013).

[28]N. Duhamel-Henry, J. L. Adam, B. Jacquier, and C. Linarès, ñPhotoluminescence of New Fluorophosphate Glasses Containing a High Concentration of Terbium (III) Ions,ò *Opt. Mater.*, **5** [3] 197-207 (1996).

[29]M. Back, A. Massari, M. Boffelli, F. Gonella, P. Riello, D. Cristofori, R. Ricco, and F. Enrichi, ñOptical Investigation of Tb^{3+}-Doped Y_2O_3 Nanocrystals Prepared by Pechini-Type Sol-Gel Process,ò *J. Nanopart. Res.*, **14** [4] 792 (2012).

[30]Y. C. Wu, C. Garapon, R. Bazzi, A. Pillonnet, O. Tillement, and J. Mugnier, ñOptical and Fluorescent Properties of Y_2O_3 Sol-Gel Planar Waveguides Containing Tb^{3+} Doped Nanocrystals,ò *Appl. Phys. A*, **87** [4] 697-704 (2007).

[31]E. Nakazawa and S. Shionoya, ñEnergy Transfer Between Trivalent Rare-Earth Ions in Inorganic Solids,ò *J. Chem. Phys.*, **47** [9] 3211-9 (1967).

[32]W. Chen, R. Sammynaiken, and Y. N. Huang, ñPhotoluminescence and Photostimulated Luminescence of Tb^{3+} and Eu^{3+} in Zeolite-Y,ò *J. Appl. Phys.*, **88** [3] 1424-31 (2000).

[33]R. Q. Li, Y. L. Liu, N. N. Zhang, L. L. Li, L. Liu, Y. M. Liang, and S. C. Gan, ñShape Controllable Synthesis and Multicolour Fluorescence of Lanthanide Doped Vernier Yttrium Oxyfluoride,ò *J. Mater. Chem. C*, **3** [16] 3928-34 (2015).

[34]J.-G. Li and Y. Sakka, ñRecent Progress in Advanced Optical Materials Based on Gadolinium Aluminate Garnet ($Gd_3Al_5O_{12}$),ò *Sci. Technol. Adv. Mater.*, **16** [1] 014902 (2015).

[35]W. H. Di, X. J. Wang, P. F. Zhu, and B. J. Chen, ñEnergy Transfer and Heat-Treatment Effect of Photoluminescence in Eu^{3+}-Doped $TbPO_4$ Nanowires,ò *J. Solid State Chem.*, **180** [2] 467-73 (2007).

[36]J.-C. Bourcet and F. K. Fong, ñQuantum Efficiency of Diffusion Limited Energy Transfer in $La_{1-x-y}Ce_xTb_yPO_4$,ò *J. Chem. Phys.*, **60** [1] 34-9 (1974).

[37]S. Z. Lu, Q. H. Yang, Y. G. Wang, Y. H. Li, and D. D. Huang, ñLuminescent Properties of Eu:$Y_{1.8}La_{0.2}O_3$ Transparent Ceramics for Potential White LED Applications,ò *Opt. Mater.*, **35** [4] 718-21 (2013).

[38]Q. W. Chen, Y. Shi, L. Q. An, J. Y. Chen, and J. L. Shi, ñFabrication and Photoluminescence Characteristics of Eu^{3+}-Doped Lu_2O_3 Transparent Ceramics,ò *J. Am. Ceram. Soc.*, **89** [6] 2038-42 (2006).

Chapter VI

Conclusions and Outlook

6.1 Conclusions

Extensive investigation on synthesis of readily sinterable oxide powders and fabrication of highly transparent Y_2O_3-based ceramics were carried out. Ammonium hydrogen carbonate precipitation is a good way for yielding well dispersed particles but not for multi-system transparent ceramics (Chapter Ⅱ). On the other hand, LRH nanosheets, when properly anion-exchanged with SO_4^{2-}, have been demonstrated to be an excellent precursor for producing readily sinterable oxide powders that can be densified into highly transparent Y_2O_3-based ceramics, including binary Y-Eu system (Chapter Ⅲ), and ternary Y-Gd-Eu (Chapter Ⅳ) and Y-Tb-Eu systems (Chapter Ⅴ). Our systematic studies have yielded the following main conclusions.

Y^{3+} and Lu^{3+} substitution for Gd^{3+} on the precursors and phosphors via ammonium hydrogen carbonate precipitation (Chapter Ⅱ)

The nucleation order during ammonium hydrogen carbonate (AHC) precipitation is found to be Y^{3+} < Gd^{3+} < Eu^{3+} < Lu^{3+}. The lattice parameters of the $(Gd,Ln)_2O_3$:Eu (Ln=Y, Lu) solid solutions linearly shrink at a higher Y^{3+}/Lu^{3+} content, and their theoretical densities linearly decrease along with increasing Y^{3+} incorporation but increase with more Lu^{3+} addition. The center of the CT bands red shifts at a higher Gd^{3+} concentration. The PL/PLE intensities and external quantum efficiency of $(Gd,Ln)_2O_3$:Eu phosphors improve at a higher Gd^{3+} concentration. Elevated calcination temperature enhances the PL intensity and the external quantum efficiency but lowers the lifetime of $(Gd,Ln)_2O_3$:Eu phosphors. AHC precipitation has been demonstrated to be a good way for yielding well dispersed phosphors, however, may not for multi-system transparent ceramics.

Optimal processing parameters for yielding transparent ceramics with LRHs as the precursor (Chapter Ⅲ)

The optimal combination of processing parameters to yield the best sinterable oxide powders from LRH nanosheets include freezing temperature synthesis (~4 °C) at $[Ln^{3+}]$=0.05-0.075 mol/L, anion exchange of the interlayer NO_3^- at the SO_4^{2-}/Ln^{3+} molar ratio of 0.03, and precursor calcination at 1100 °C. Slower heating (1 °C/min) in the ramp stage of vacuum sintering benefits optical quality of the final ceramic and the optimal sintering temperature is 1700 °C.

Effects of Gd^{3+} substitution for Y^{3+} on resultant particles and ceramics (Chapter Ⅳ)

The particle/crystallite sizes of the $(Y_{0.95-x}Gd_xEu_{0.05})_2O_3$ (x=0.15-0.65) oxide powders slightly decrease at a higher Gd^{3+} concentration, while the grain sizes of their sintered bodies markedly increase with increasing Gd^{3+} incorporation. In the temperature range of 1100-1480 °C, the sintering kinetics is mainly controlled by grain boundary diffusion with similar activation energies of ~230 kJ/mol. The bandgap energies of the $(Y_{0.95-x}Gd_xEu_{0.05})_2O_3$ ceramics generally decrease with more Gd^{3+} addition. Gd^{3+} substitution for Y^{3+} enhances the PL and PLE intensity. The ceramic fluorescence lifetime decrease along with incerasing x.

Effects of Tb^{3+} and Eu^{3+} codoping on ceramic optical properties (Chapter Ⅴ)

The effective energy transfer from Tb^{3+} to Eu^{3+} was demonstrated, with which green to orange emission of the $(Y_{0.98-x}Tb_{0.02}Eu_x)_2O_3$ (x=0-0.04) ceramics can be precisely tuned by varying the Eu^{3+} concentration. Improved emissions for both Eu^{3+} and Tb^{3+} were obtained by varying the excitation wavelength from 270 to 323 nm, without notably changing the color coordinates of the whole emission. The addition of Eu^{3+} shortens the fluorescence lifetimes of the $(Y_{0.98-x}Tb_{0.02}Eu_x)_2O_3$ ceramics for both the 544 nm Tb^{3+} and 613 nm Eu^{3+} emissions.

6.2 Outlook

Transparent ceramic scintillators are being widely developed to replace the expensive single crystal. By contrast with the previous reports and commercial scintillators, the transparent Y_2O_3-based ceramics that are comparable to single crystals in optical quality with fine grain sizes made in this work are incomparably superior.

The optimized cost-effective vacuum sintering technique can be adopted for mass production and industrialization of transparent ceramics.

The particle synthesis route deveoped in this thesis provides a good way for yielding less agglomerated phosphor powders and highy transparent ceramics.

The underlying mechanism of Gd substitution on densification and optical properties not only reveals the role of Gd but also gives some enlightenments on ceramic sintering and spectroscopy study, with which the obtained highly transparent certamics can be applied in various optical and thermodynamic applications, including scintillation.

Tb^{3+} and Eu^{3+} combination in energy transfer and color-tunable emission has been demonstrated in ceramic field and may find various optical applications in the future.

Appendix

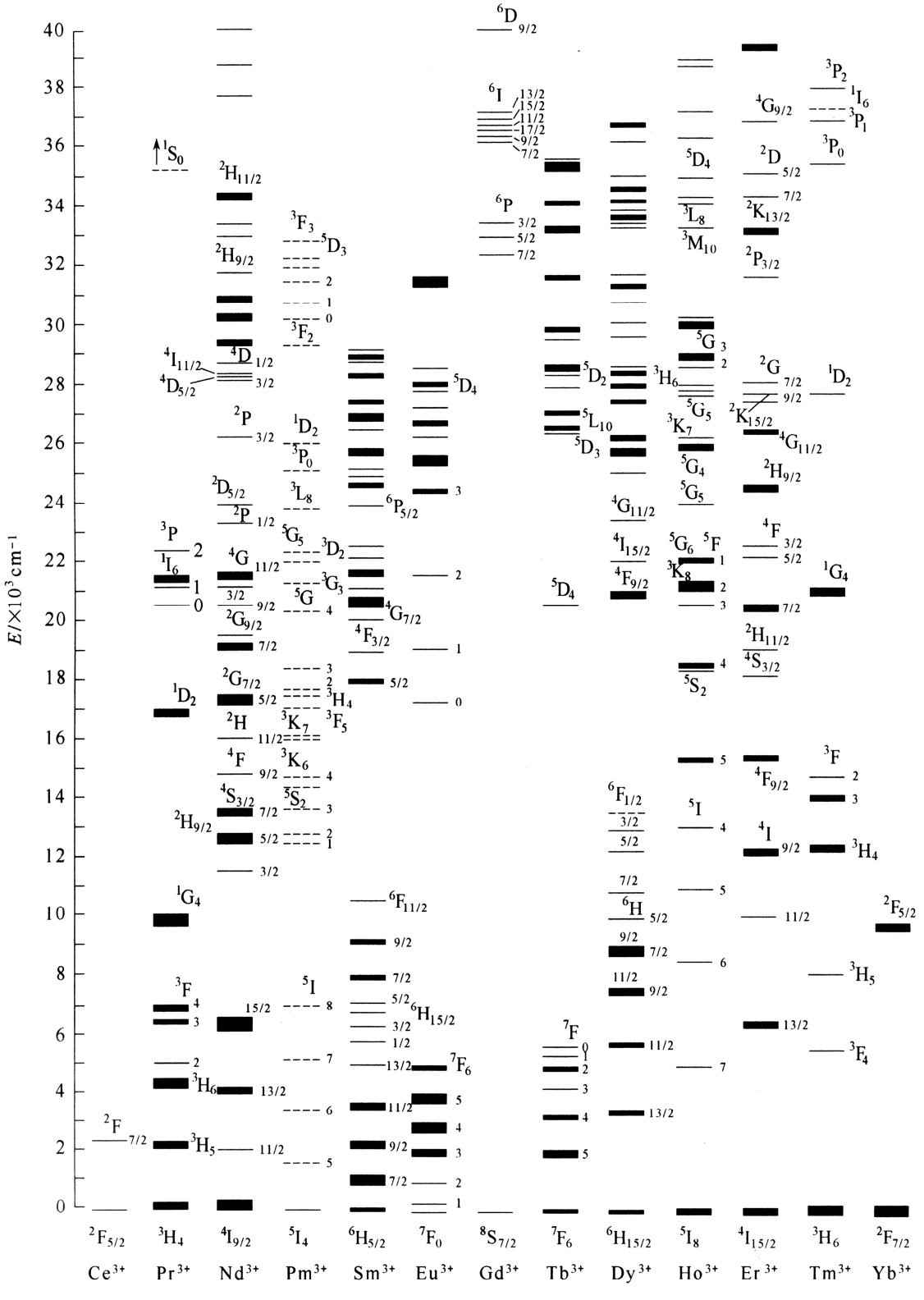

Fig. 1 Energy levels of the trivalent rare-earth ions.

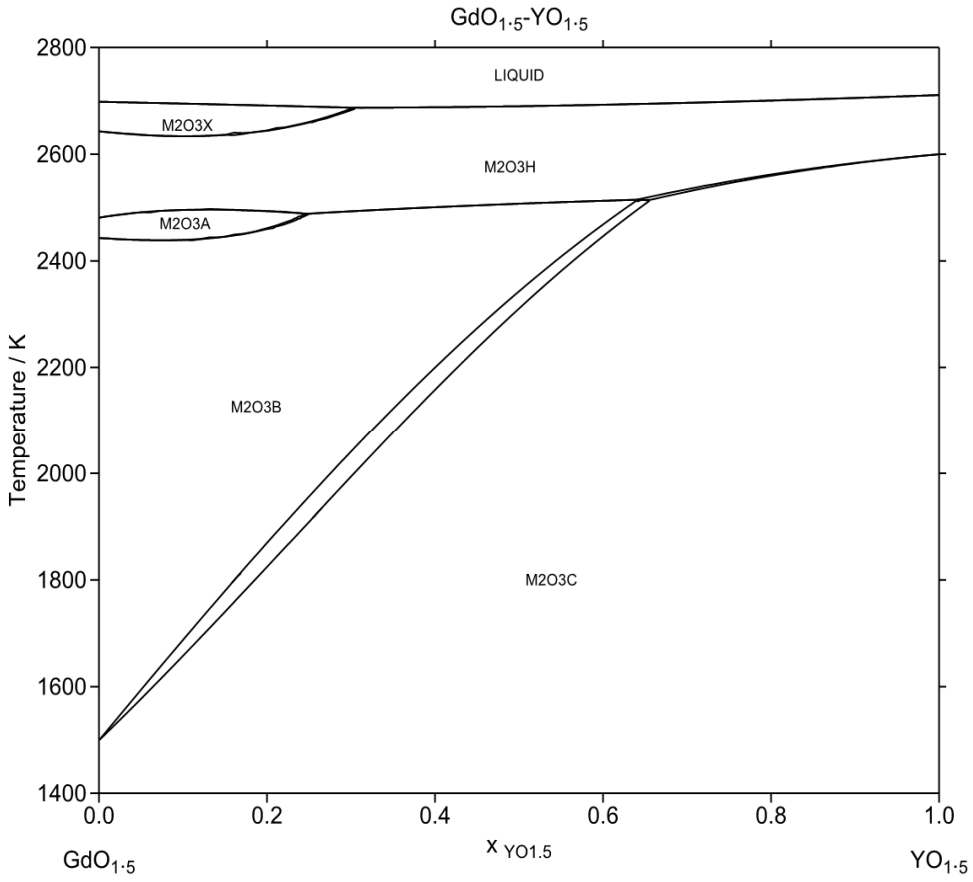

Fig. 2 Y_2O_3-Gd_2O_3 phase diagram.

ACHIEVEMENTS

Publications

1. **Bin Lu**, Ji-Guang Li, and Yoshio Sakka, ñControlled Processing of $(Gd,Ln)_2O_3$:Eu (Ln=Y, Lu) Red Phosphor Particles and Compositional Effects on Photoluminescence,ò ***Sci. Technol. Adv. Mater.***, 14 [6], 064202 (2013) ï DOI: 10.1088/1468-6996/14/6/064202

2. **Bin Lu**, Ji-Guang Li, Tohru S. Suzuki, Mehdi Estili, Weigang Liu, Xudong Sun, and Yoshio Sakka, ñControlled Synthesis of Layered Rare-Earth Hydroxide Nanosheets Leading to Highly Transparent $(Y_{0.95}Eu_{0.05})_2O_3$ Ceramicsò, ***J. Am. Ceram. Soc.***, 98 [5] 1413-22 (2015) ï DOI: 10.1111/jace.13488

3. **Bin Lu**, Ji-Guang Li, Tohru S. Suzuki, Hidehiko Tanaka, Xudong Sun, and Yoshio Sakka, ñEffects of Gd Substitution on Sintering and Optical Properties of Highly Transparent $(Y_{0.95-x}Gd_xEu_{0.05})_2O_3$ Ceramicsò, ***J. Am. Ceram. Soc.***, in press (2015) ï DOI-10.1111/jace.13627

4. **Bin Lu**, Ji-Guang Li, Xudong Sun, and Yoshio Sakka, ñFabrication and Characterization of Transparent $(Y_{0.98-x}Tb_{0.02}Eu_x)_2O_3$ Ceramics with Color-Tailorable Emissionò, submitted to ***J. Am. Ceram. Soc.***

5. Weiguang Liu, Xiaoli Wu, Ji-Guang Li, Qi Zhu, **Bin Lu**, Xiaodong Li, Xudong Sun, and Yoshio Sakka, ñFew-Layer-Thick Nanosheets of $Ln_2(OH)_5NO_3{\cdot}nH_2O$ ($Ln=Y_{0.98}RE_{0.02}$, RE=Pr, Sm, Eu, Tb, Dy, Ho, Er, and Tm): Exfoliation-Free Synthesis, Interlayer Engineering via SO_4^{2-} Exchange, and the Derivation of Better Dispersed Ln_2O_3 Nanophosphorsò, in submission

Conferences/ Symposiums

Oral/Poster Presentations

1. **Bin Lu**, Ji-Guang Li, Tohru Suzuki, and Yoshio Sakka, ñSynthesis of $(Y_{0.95-x}Gd_xEu_{0.05})_2O_3$ Red Phosphors and Fabrication of Transparent Ceramics with Sulfate-Exchanged Nitrate-Type Layered Hydroxide Nanosheets as Precursors,ò ***The Eighth International Conference on the Science and Technology for Advanced Ceramics (STAC-8)***, 25pHO05; Yokohama, Japan, June 25th-27th, 2014. ï **Oral presentation**

2. **Bin Lu**, Ji-Guang Li, Tohru Suzuki, and Yoshio Sakka, ñSynthesis of $(Y_{0.95}Eu_{0.05})_2O_3$ Phosphors and Fabrication of Transparent $(Y_{0.95}Eu_{0.05})_2O_3$ Ceramics,ò ***Spring Meeting of Japan Society of Powder and Powder Metallurgy (JSPM)***, 3-19A; Waseda University, Tokyo, Japan, June 3rd-5th, 2014. ï **Oral presentation**

3. **Bin Lu**, Ji-Guang Li, and Yoshio Sakka, ñSynthesis of Well Dispersed $(Gd,Ln)_2O_3$:Eu (Ln=Y, Lu) Red Phosphors and Compositional Effects on Photoluminescence,ò ***The 5th International Congress on Ceramics (ICC5)***, D-05-003; Beijing, China, August 17th-21st, 2014. ï **Oral presentation**

4. **Bin Lu**, Ji-Guang Li, and Yoshio Sakka, ñ$(Gd_{0.95-x}Ln_xEu_{0.05})_2O_3$ (Ln=Y, Lu, x=0-0.95) Phosphors: Synthesis, Formation Mechanism, Compositional Impacts and Photoluminescence Behaviours,ò ***The 7th International Conference on the Science and Technology for Advanced Ceramics (STAC-7)***, PP-106; Yokohama, Japan, June 19th-21st, 2013. ï **Poster presentation**

5. **Bin Lu**, Ji-Guang Li, and Yoshio Sakka, ñ$(Y_{0.95}Eu_{0.05})O_3$系易焼結性粉末と透光性セラミックスの作製 (Syntheis of Sinterable $(Y_{0.95}Eu_{0.05})O_3$ Powders and Fabrication of Transparent $(Y_{0.95}Eu_{0.05})O_3$ Ceramics),ò ***Spring Annual Meeting of the Society of Powder Technology***; Tokyo, Japan, May 19-20th, 2015.